FACULTY OF SCIENCE AND TECHNOLOGY

MASTER'S THESIS

Study programme / specialisation: Engineering Structures and Materials / Mechanical Engineering	The *spring* semester, *2023* Open / ~~Confidential~~
Author: Anders Thon Sletsjøe	
Supervisor at UiS: Vidar Folke Hansen	
Thesis title: Effects of cold rolling on the mechanical properties and grain structure of Inconel 718 alloy	
Credits (ECTS): 30	
Keywords: Inconel 718 Cold rolling Texture Precipitation Deformation	Pages: 97 + appendix: 42 Stavanger, *15.06.2023*

Abstract

This master thesis in material science aimed to investigate the influence of increased degree of cold rolling reduction of precipitation formation in commercially produced Nickel-base superalloy Inconel 718, and evaluate the mechanical properties. The research involved mechanical testing through tensile testing and Vickers microhardness testing, accompanied by microstructural investigation with optical and scanning electron microscope.

The material was machined into thin strips and solution heat treated at 1100°C for 1 hour and water quenched to normalize the material. Subsequently, the samples underwent cold rolling with a constant reduction down to 20% and 50% of their original thickness, followed by a two-step precipitation hardening treatment at 720°C for 8 hours, furnace cooling to 650°C for another 8 hours and air cooling to room temperature.

The mechanical testing revealed a clear increase in hardness, yield strength and tensile strength with increased cold rolling reduction, while also decreasing the ductility. The precipitation of secondary strengthening phases also contributed to increased strength, albeit to a lesser extent as degree of deformation increased.

The microstructure revealed a transformation from an equiaxed, well defined grain structure with a significant amount of deformation twins, to a visibly deformed grain structure characterized by elongated grains and deformation bands. Further, the microstructure showed indication of texture formation with a preferred grain orientation and intergranular slight variations in orientation.

Acknowledgement

Firstly I Would like to direct a special thank you to Karl Petter Aarthun at Scandinavian Fittings & Flanges for kindly providing me with the materials needed to conduct this research. Their contribution made it possible for me to write this thesis.

I am also deeply grateful for my faculty supervisor, Professor Vidar Hansen. His continuous support, insightful feedback and guidance throughout the entire research process has been invaluable.

I would like to extend a heartfelt thank you to my coordinating engineer Wakshum Mekonnen Tucho and senior engineer Espen Undheim for help with SEM imaging, insight, engagement and valuable discussions.

I would also like to thank senior engineers Johan Andreas Thorkaas and Mats Ingdal for help in the laboratory and for general guidance on research methodology.

Lastly, I want to express my sincere appreciation to my classmates, especially Lars Olav Laukvik, Marius Jørs, and Kristian Nesse. Their friendship, engaging conversations, and shared experiences have made this study period truly memorable and enjoyable.

Contents

List of Figures

List of Tables

Symbols and Abbreviations

γ	Gamma
γ'	Gamma Prime
γ''	Gamma Double Prime
δ	Delta

fcc	Face Centered Cubic
bct	Body centered Tetragonal
hcp	Hexagonal Close-Packed

0D	Undeformed non precipitation hardened
0DPH	Undeformed precipitation hardened
20D	20% deformed non precipitation hardened
20DPH	20% deformed precipitation hardened
50D	50% deformed non precipitation hardened
50DPH	50% deformed precipitation hardened

SFF	Scandinavian Fittings & Flanges
TTT	Time Temperature Transformation
SHT	Solution Heat Treatment
HV	Hardness Vickers
RD	Rolling Direction
ND	Normal Direction
TD	Transverse Direction
ASB	Adiabatic Shear Band
SEM	Scanning Electron Microscope
TEM	Transmission Electron Microscope
EDS	Energy Dispersive Spectroscopy
EBSD	Electron Backscatter Diffraction
IPF	Inverse Pole Figure
APF	Atomic Packing Fraction
SFE	Stacking-Fault Energy

1 Introduction

This thesis has consisted of mechanical testing and microstructural investigation of cold rolled conventionally precipitation hardenable nickel-based superalloy Inconel 718.

The scope of this thesis was to research and inspect the impact of varying degree of deformation by cold rolling had on precipitation hardening in nickel-based superalloy Inconel 718. This was done by mechanical testing for strength and microstructural investigation by SEM and optical microscopy on an increasing degree of deformation, namely 0%, 20% and 50%.

The material was provided by Scandinavian Fittings & Flanges in the form of four 7/8", 140mm long studbolts. These were machined down and solution heat treated at 1100°C for one hour followed by quenching. Samples were then deformed with a constant reduction, followed by a two step precipitation hardening heat treatment at 720°C for 8 hours and 650°C for 8 hours.

The mechanical testing consisted of Vickers microhardness testing and tensile testing. Microstructural examination was done by optical light microscope and SEM. EDS was done for chemical analysis, and EBSD for grain structure and texture.

All figures presented in this thesis has been reproduced by the author using the referenced sources mentioned in the figure captions.

2 Theory

2.1 History and Use of Nickel-based Alloys

Nickel-base alloys have undergone a long development process stretching all the way back to the early 1900's. The need for a material that could withstand the high temperatures of that times turbosupercharger became present. A while later the first austenittic stainless steel was discovered, and it is from this the γ face-centered cubic austenite field of study the modern superalloys known today stems from [1].

Nickel-based superalloys are widely recognized as a very useful range of materials due to their wide range of applications and uses. They hold significant importance due to their exceptional performance, particularly at elevated temperatures, with regards to strength and corrosion resistance. Inconel 718, which is the focus of this thesis, demonstrates great strength, creep rupture resistance, and corrosion resistance up to temperatures as high as 650°C [2], making it suitable for use in aviation, space exploration, and petrochemical industries.

2.2 Nickel-based Alloy Metallurgy

The superalloys consist of an austenittic fcc γ matrix with a number of various secondary phases which will be discussed in more detail later in chapter 2.2.2. These secondary precipitate phases are what gives the superalloys its strength along with solid solution strengtheners.

The nickel-based superalloys mainly receive their strength from intermetallic compound precipitation in an austenittic fcc matrix and also solid solution strengtheners. Superalloys which is strengthened by aluminium or titanium receives its strength from the γ' precipitate phase, while alloys strengthened by niobium receives it from the γ'' precipitate phase. Alloys strengthened by niobium plus titanium/aluminium, such as Inconel 718, uses both γ' and γ'' precipitates for strengthening, with γ'' being the main contributor. Carbides may also provide some strengthening through dispersion hardening. Other phases may also be present such as the δ, η, σ, μ and Laves phase.

The fcc ordered $Ni_3(Al,Ti)$ γ' phase and the bct ordered Ni_3Nb γ" together with the hexagonal ordered Ni_3Ti η phase makes up the so called geometrically close-packed phases. The orthorhombic Ni_3Nb δ phase and the η phase is not specifically used for their strength contributions, but are useful during processing.

Harmful phases that can affect the material in a negative way may be present and can consist of the topologically close-packed hexagonal Laves, tetragonal σ and rhombohedral μ phases [3].

2.2.1 Chemical Composition

Chemical composition of an alloy might vary with what wants to be achieved in terms of material properties. The chemical composition of the material investigated in this thesis was stated in the material documentation provided by SFF (Scandinavian Fittings & Flanges) and is given in Table 2.1.

Table 2.1: Chemical composition of Inconel 718 provided by SFF

C	**Mn**	**Si**	**P**	**S**	**Ni**	**Cr**	**Mo**	**Cu**	**Al**	**Ti**	**Nb**	**B**	**Fe**
0.014	0.07	0.06	0.008	0.0005	54.3	17.86	2.99	0.05	0.51	0.96	5.02	0.0025	Bal

The list below explains the effects of the variable alloying elements found in they alloy of this thesis and their contribution to the properties of the material:

Carbon - Grain boundary refiner and carbonnitride former [3]. Also carbide former, mainly MC which can increase the toughness and ductility if carbon content is low [4].

Manganese - Regarded as an impurity which reduces the hot malleability and creep ductility due to grain boundary cracking. However it may increase weldability when segregated at grain boundaries [5].

Silicon - Can increase sulfidation resistance [3], but also decrease hot malleability, creep ductility due to grain-boundary cracking and hot ductility [5].

Phosphorus - Regarded as a detrimental tramp element with property-level reductions [3]. However it has been shown by Horton et al. and McKamey et al. that it can improve stress rupture properties in some nickel-base alloys when added in controlled amounts [6] [7].

Nickel - Primary element and can form precipitation strengthening phases with elements such as Al, Ti and Nb.

Chromium - Solid solution strengthener. Forms carbides M_7C_3 and $M_{23}C_6$. Improves oxidation and sulfidation resistance [3].

Molybdenum - Solid solution strengthener. Carbide former MC, $M_{23}C_6$ and M_6C [3].

Copper - Segregation of copper at grain boudaries can reduce the hot malleability and creep ductility due to grain-boundary cracking [5].

Aluminium - Forms γ'' Ni_3(Al,Ti). Hardening precipitates and/or intermetallics. Oxidation resistance [3].

Titanium - Forms γ'' Ni_3(Al,Ti) and carbide MC [3].

Niobium - Forms γ', and forms carbides MC and M_6C [3].

Boron - Improves creep properties, and increases rupture strength. Can also form borides if present in large amounts [3].

Iron - Solid solution strengthener [3].

2.2.2 Phases of Nickel-based Alloys

A number of phases can be present in Nickel-base alloys. This chapter gives av overview of most of them. The most common phases found in Inconel 718 are the Ni_3Al and Ni_3(AL,Ti) compositioned γ', Ni_3Nb compositioned γ'', Ni_3Nb compositioned δ and various carbides. The following information presented in this chapter is based on information from [2] and [3].

Gamma Prime (γ''):

This is a phase with a fcc (ordered $L1_2$) crystal structure with the formula Ni_3Al and Ni_3(Al, Ti). Lattice parameters are 0.3561nm for pure Ni_3Al and 0.3568nm for $Ni_3(Al_{0.5}Ti_{0.5})$. It is often coherent with the γ matrix and are rich in elements such as aluminium, titanium and tantalum. γ' can be represented with varying shapes from spherical to cubic, but in modern Ni-base alloys it is generally cuboidal in shape. By experiments it has been shown that with increasing mismatch of γ and γ' phase the shape of the phase can change from spherical to globular to blocky to cuboidal. Also with high mismatch and exposure to heat above 700°C, the undesirable η and δ phase can be formed. In alloys containing niobium, the related precipitate phase γ'' is preferred over γ'.

Gamma Double Prime (γ''):

This BCT ordered compound with a $D0_{22}$ crystal structure and lattice parameters c=0.740nm and a=0.362 nm is the primary strengthening phase of superalloys containing Nb. The composition can be expressed as Ni_3Nb and it forms as disk-shaped particles on the {100} planes. When inspecting the unit cell, it can be

seen that the atomic arrangement is related to the $L1_2$ structure of the γ' phase. The a parameter is close to that γ' shows, but the c parameter is approximately doubled, hence the name γ''.

Delta (δ):

Has an orthorhombic crystal structure with lattice parameters a=0.5106-0.511nm, b=0.421-0.4251nm and c=0.452-0.4556nm and a Ni_3Nb composition. Can be found in Inconel 718 that has been over aged. The metastable γ'' that has the same composition can transform into the stable δ phase. When formed in the temperature range of 815-980°C it takes on a acicular shape. At low aging temperatures it forms by cellular reaction, and at high temperatures it forms by intergranular precipitation.

Eta (η):

Has a hcp ($D0_{24}$) ordered crystal structure, also referred to as geometrically close packed (gcp). It has the lattice parameters c=0.8276 and a=0.5093 and a Ni_3Ti composition. It may form intergranularly in cellular form or as platelets in a Widmanstätten pattern.

Laves

The aves phase is an intermetallic compound with a hexagonal crystal structure and lattice parameters a=0.475-0.495nm and c=0.770-0.815nm. The formula can be Fe_2Nb, Fe_2Ti, Fe_2Mo, Co_2Ta and Co_2Ti. It normally takes a form as elongated, irregularly shaped globules or as platelets if exposed to high temperatures over an extended period of time.

Sigma (σ):

The sigma phase has a tetragonal crystal structure with lattice parameters a=0.880-0.910nm and c=0.450-0.480nm. The compositional formulas are FeCr, FeCrMo, CrFeMoNi, CrCo and CrNiMo and is mostly seen in Fe-Ni- and Co-base alloys, and to a lesser extent in Ni-base superalloys. Can be seen as often elongated, irregularly shaped globules after extended exposure in the temperature range 540-980°C.

Carbides

Some important types of carbides that can exist in nickel-base superalloy is MC, M_6C, $M_{23}C_6$ and M_7C_3, where M can be a number of different metal atoms. The formation of these carbides depends on temperature where $M_{23}C_6$ and M_7C_3 are formed at low temperatures, M_6C is formed at an intermediate temperature, while MC are formed at high temperatures. MC can be formed from the melt or from precipitation from supersaturated solid solutions above 1038°C. The intermediate carbides favour a temperature in the range of 816 – 982°C, and maybe as high as 1038°C, while the low temperature carbides favour a temperature range of 790 – 816°C.

Borides

Small additions of boride are essential in the formation of borides that are known to improve creep-rupture resistance of superalloys. Borides are blocky or half moon shaped hard particles that can be seen at grain boundaries. Although not in the same volume as carbides. The commonly found boride in superalloys is in the form of M_3B_2, which has a tetragonal unit cell.

2.3 Strengthening Mechanisms

All mechanisms and processes described in the following few chapters plays a different role in determining the strength of a material in terms of the yield strength. What they all have in common is that the outcome of each mechanism hinders the motion of dislocations. These mechanisms involve solid solution strengthening, precipitation hardening, work hardening, and grain size influence.

A materials Yield Strength (σ_Y) can be determined by the sum of the individual independent mechanisms, and is given by equation 1 below.

Influence of strengthening mechanisms on Yield Strength:

$$\sigma_Y = \sigma_0 + \Delta\sigma_{ss} + \Delta\sigma_{ppt} + \Delta\sigma_{dis} + \frac{k}{\sqrt{d}} \tag{1}$$

Where σ_Y is the yield strength, σ_0 is the yield strength of a perfect metal, σ_{ss} is the contribution of solid solution strengthening, σ_{ppt} is the contribution of precipitates, σ_{dis} is the contribution of work hardening (dislocations) and the last term represents the grain size influence where d is the average grain diameter and k is a material constant specific to the material.

2.3.1 Solid Solution Strengthening

Solid solution strengthening is the method of strengthening a metal by introducing impurity atoms in the alloy. Metals with a high degree of purity are almost always weaker than alloys [8].

By inducing impurity atoms that have reasonably high solid solubility with the matrix and high hardening coefficients into the alloy it can increase the overall strength of the material by increasing its tensile and yield strengths, and should also have a beneficial impact of the materials creep strength. This increase in strength is primarily due to impurities restricting dislocation movement [5].

The impurity atoms may take place in the lattice either substitunionally by replacing an original atom, or interstitially by placing itself in between the lattice points if the atom is sufficiently small as shown in Figure 2.1 below. If the substitutional atom is smaller than what it is replacing, the crystal lattice is put into tension and the surrounding area will experience tensile strains, while if the substitutional atom is larger than what it is replacing, the larger atom will induce compressive strains to the surrounding area [8].

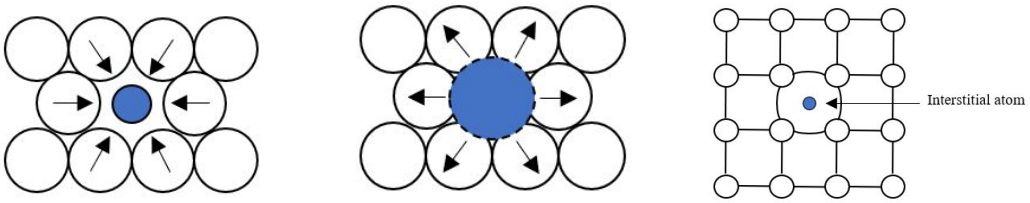

(a) (b) (c)

Figure 2.1: Representation of (a) small substitunional defect, (b) large substitutional defect, and (c) interstital defect. Arrows indicate lattice strain [8].

Both substitutional and interstitial defects produce stresses and distortions in the lattice which hinders dislocation motion, which ultimately increases the materials strength and creep strength.

2.3.2 Strengthening by Precipitation

Precipitation hardening is a process done to enhance the strength of a material by introducing precipitate phases into the previously supersaturated matrix achieved through solution annealing. The final structure of the material is influenced by the temperature, soaking time and cooling rate. To determine a desired structure, a TTT-diagram, as Figure 2.2 shown below can be studied prior to treatment[3].

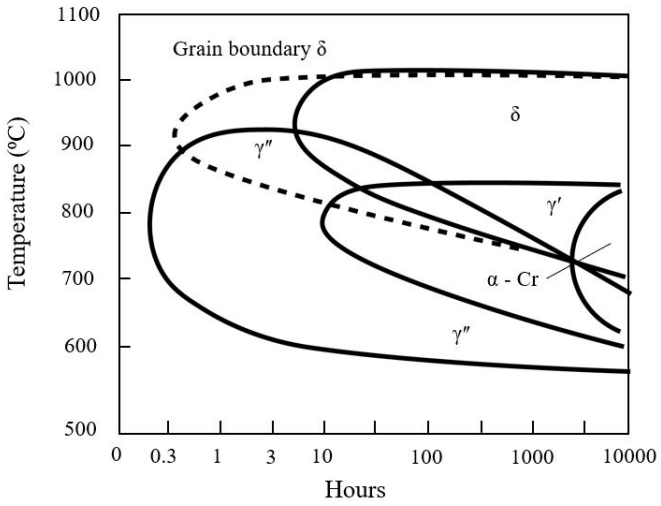

Figure 2.2: TTT-diagram for Inconel 718 [9].

Selecting temperature, soaking time, and cooling rate plays a significant role in determining what phases are formed and which will be present in the final structure.

Precipitation hardening increases the resistance to dislocation motion ultimately increasing the strength. These dislocations can either bend around or cut through the precipitate in something called Orowan mechanisms. The stress required for a dislocation to bend around a precipitate is related to the interparticle distance, meaning that it is inversely proportional to the interparticle distance which increases when a precipitate particle increases in size. For a dislocation to cut through a precipitate the stress required is proportional to the square root of the size of the precipitate. This means that optimum strength is achieved when the interparticle spacing is exactly small enough to avoid dislocations from bowing [5].

2.3.3 Work Hardening

Work hardening, also known as strain hardening is the process of plastically deforming a material to induce dislocation networks to ultimately strengthen the material. In this thesis the work hardening technique that has been used is cold rolling, which is also the most common method and will be discussed further in this chapter.

Plastic deformation primarily occurs by gliding of displacement of dislocations. By work hardening, the mobility of dislocations is impeded, leading to an increase in strength. This is based on the theory presented in 1934 by physicist and mathematician G. I. Taylor that presents the idea that some dislocations become stuck inside a crystal structure, becomes a source of internal stress which limits gliding dislocations [10].

During cold working, most of the energy put into the sample is dissipated in the form of heat, although a portion of the energy is also conserved in the metal as dislocations, vacancies, stacking-faults and stored energy [11]. Cold rolling also distorts the grains in the structure, and aligns itself in the rolling direction to form a texture if sufficient plastic deformation has happened. If the material is deformed heavily, the grains can be distorted to such an extent that the grains fracture and form smaller grains [11]. Smaller grains equals more grains and a higher density of grain boundaries which hinders movement ultimately increasing the strength of the material.

While work hardening or cold working a material does increase the materials tensile strength, yield strength and hardness, the ductility and the materials general ability to deform decreases [10].

The amount, or rather density of dislocations increases with increased cold work due to dislocation multiplication or by formation of new dislocations. As the dislocation density increases, the average distance between them decreases resulting in less space for dislocation movement and ultimately increased strength [8]. The effect of this can be reversed by an annealing process.

2.4 Influence of Cold Rolling on Precipitation Formation

Cold rolling induces a great deal of dislocations, vacancies, stacking faults, twins and stored energy into the material. All of these effects may influence the precipitation process in various ways. The nucleation of precipitate phases can be altered by work hardening. Not just the formation, but also the nucleation sites in which the precipitates form.

In Inconel 718, the metastable γ'' is the main strengthening phase. Normally after prolonged aging at temperatures below 900°C a transformation of the metastable γ'' to the stable δ phase occurs ($\gamma'' \rightarrow \delta$). Formation of δ can also directly occur at temperatures above 900°C jumping the metastable main strengthening phase [12]. As both γ'' and δ has the same chemistry of Ni_3Nb, formation of δ can come at the expense of the favorable γ''.

In this normal formation of precipitates, δ can nucleate at stacking faults in the pre-existing γ'' particles. At lower temperatures, δ nucleates at grain boundaries as well as coherent and incoherent twin boundaries, while at higher temperatures they can intergranularly precipitate [13].

Introducing deformation into the structure and increasing the density of dislocations will increase the materials strength, while it can also form additional nucleation sites for δ. It is shown that slip bands formed during deformation can act as nucleation sites for δ [14]. Cold rolling can also create excess vacancies which attracts Nb segregation, leaving more nucleation sites [15].

The normal precipitation kinetics has then been influenced by plastic deformation as energy needed for precipitation of certain phases decreases with increasing degree of deformation, and also where precipitates form, and heterogeneous nucleation of stable δ phase on dislocation features leading to a reduction of density of the desired γ" phase [16].

2.5 Stacking Fault

The fcc structure consist of a stacking sequence of three, such as ABCABCABC where A, B and C consist of a plane of close-packed atoms. This is the densest configuration a solid can have. This gives an Atomic Packing Fraction (APF) of 0.74, which is the same fraction as for the hcp structure. For comparison, the BCC structure has an APF of 0.68 [10].

A stacking fault occurs when this sequence is interrupted either by the removal of a plane, or by addition of a plane. These faults are called intrinsic stacking fault and extrinsic stacking fault respectively [2]. Although this sort of structure is reasonably stable, it is more often found in deformed metals than annealed metals since some work have had to be done in order to produce it [10]. This deviation from the normal stacking sequence carries a specific energy which is termed stacking-fault energy (SFE). The SFE (γ_{SF}) is the energy per unit area of the planar defect between the two partials.

2.6 Twinning

Deformation twinning refers to a process in which a region of a crystal structure experiences uniform shear which produces a region that is reoriented but has the same crystal structure [17]. Figure 2.3 below show an arrangement of atoms in a twin region. The white circles represent the atomic position before twinning occurs, while the black circles is the atomic position after.

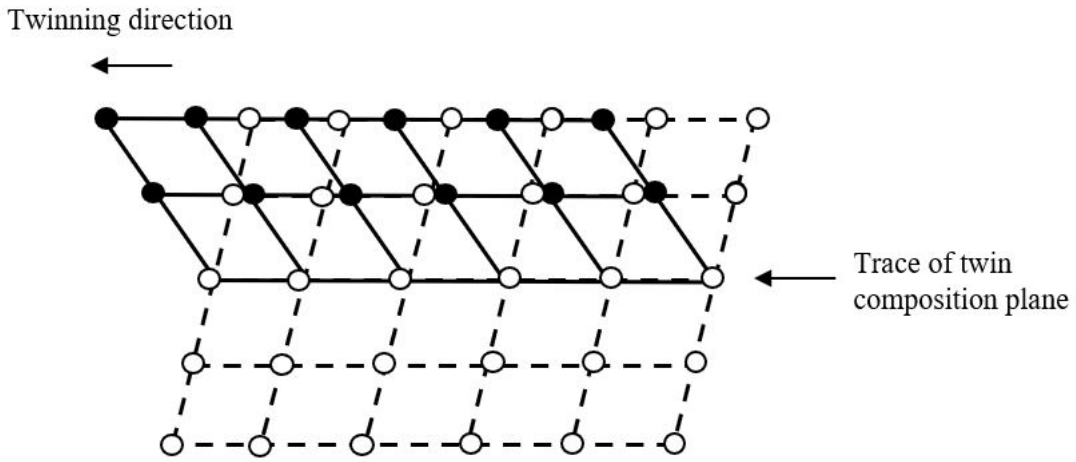

Figure 2.3: Atomic arrangement of a twin structure [18]

What differentiates slip from deformation twinning is that twinning occurs without rotation of the crystal lattice [17]. Also twinning is characterized by displacement of atomic planes within a crystal lattice parallel to a specific twinning plane. This divides the lattice into symmetrical parts, each with a distinct orientation. This results in a mirror image being formed across the twinned region. This is different from slip where the crystal orientation above and below the slip plane is identical [18].

Similarly to linear defects such as edge and screw dislocations, twinning occurs in certain crystallographic planes and directions. For an FCC crystal structure such as Inconel 718, the preferred twinning plane is the {111}-family of planes, and the $\langle 112 \rangle$direction [10].

Compared to deformation resulting from slip, twinning typically produces a smaller amount of plastic deformation. Nevertheless, the greatest value of formation of

twins has to do with the crystallographic reorientation that occurs. This new arrangement may now be oriented such that new slip systems are in favourable positions relative to the stress axis, encouraging new slip processes to take place [8].

Deformation Twins:

In structures where the stacking-fault energy is low, deformation twinning can occur during rolling at low temperatures with a medium to large rolling strain [18].

Annealing Twins:

Twins that formed as a consequence of grain growth or during recrystallization of cold worked materials [19].

2.7 Shear Bands

During work hardening (cold rolling) most of the kinetic energy induced into the material is converted to thermal energy which leads to an increase in temperature of the material. This means that during cold rolling, the material experiences both softening due to increased heat, and strain hardening due to plastic deformation [20].

Shear bands, or adiabatic shear bands (ASBs) where adiabatic means that no heat is transferred into the system and the change in internal energy is due to the work done can form when close to adiabatic heating occurs which can lead to local softening of the material, thermomechanical instability and immense localized shear strain along narrow bands [20].

Once these bands are initiated, they can become self-propagating due to the adiabatic heating produces a decrease in local flow stress. The shear bands can thus be a highly dangerous factor for deformation as it can lead to localized deformation and ultimately local failure. Not only does shear bands have the capacity to significantly degrade the mechanical properties of a material, but it can also lead to final failure due to shear-induced cracking [21].

2.8 Deformation Texture

Most metals of industrial interest are polycrystalline, meaning that each grain has an orientation different from the orientation of the neighbouring grain which forms a more or less random structure. During deformation the orientation of the individual grains can rearrange in a specific preferred orientation and form what is called a deformation texture.

Changes in orientation that takes place during deformation are not random and are a consequence of the common deformation mechanisms that takes place on the most favourable oriented slip or twinning systems. Because the number of slip systems are limited, a limited amount of orientations are possible and deformation textures are formed. Deformation texture of fcc metals are primarily determined by their stacking-fault energy (γ_{SF}). Deformation texture for materials with low γ_{SF} ($< 25 mJm^{-2}$) such as Inconel 718 is referred to as alloy type textures [22].

Texture can have an impact of the mechanical properties in a material. When tensile tested in the direction of the preferred orientation, materials tends to show increased values of tensile ductility, increased fracture toughness and decreased strength. The opposite can be observed when tensile testing in the transverse direction of the preferred orientation [23].

Results are often presented with the use of pole figures of stereographical projection which show the distribution of specific crystallographic orientations in the material.

2.9 Heat Treatment

During this thesis two different heat treatments will be carried out. One solution heat treatment prior to cold rolling, and a two stage precipitation hardening heat treatment after cold rolling.

2.9.1 Solution Heat Treatment

Solution heat treating also known as solution annealing is the process of heating a material to a specific temperature. This process is done to homogenize the microstructure prior to precipitation hardening, and dissolve solute atoms to form a single-phase solid solution. Once the material is held (soaked) at the specified temperature for a predetermined length of time, the material is quenched in a liquid medium. This is to rapidly cool the material to room temperature to effectively lock the solution in the heat treated state[3].

For Inconel 718, this treatment is often done in the region of 970-1250°C, for a specific time to release age hardening constituents into the matrix and to dissolve the Laves phase [24]. In this thesis the solution heat treatment was conducted at 1100°C for one hour, and quenched in water. This is discussed further in Chapter 3.4.

2.9.2 Precipitation Hardening Treatment

Precipitation hardening is done to form finely dispersed nanometer-sized precipitates in the matrix. Age hardening constituents in the form of precipitates are formed in the structure which impedes dislocation motion and ultimately strengthens the material.

Although strengthening phases are formed during precipitation hardening, other detrimental phases or phases that does not contribute to strength might also be unavoidable and formed. It is thusly wise to avoid temperature ranges and soaking times that may produce unwanted phases. This can be decided by studying an alloy-specific TTT-diagram as shown in Chapter 2.3.2.

In this thesis the two-stage precipitation hardening heat treatment was done at 720°C for eight hours, then furnace cooled to 650°C and held for another eight hours followed by air cooling to room temperature. This is discussed further in Chapter 3.4

2.10 Fractography

There is in general two different fracture modes. Brittle fracture, and ductile fracture. What differentiates these and is the basis of classification is the materials ability to experience plastic deformation[8].

A materials ability to undergo plastic deformation before breaking is known as ductility. It is a relative term, meaning that there is no set number for what classifies it as a brittle or ductile fracture, but rather one has to look at the situation to determine the classification. Ductility is most often expressed as percentage elongation before fracture [25].

Ductility is generally a desired material property as it allows the material to plastically deform before braking, giving time to prevent catastrophic failure under service. This plastic flow helps to reduce stress concentrations at defects in the material, making a ductile material more tolerant of imperfections [25].

Ductility depends on the fracture mechanism such as cleavage, fracture by plastic void growth or creep fracture. Cleavage fractures are associated with zero or very low ductility, while a plastic void growth fracture is considered ductile with elongation normally ranging from 20-100% , but also in high strength steels only achieving a few percentage elongation [25].

Intergranular and transgranular fracture. Transgranular fracture is a fracture where a crack propagates across grain boundaries. This type of fracture can be

of a ductile variant with involving void formation, or through a brittle process known as cleavage. Intergranular fractures is a brittle type of fracture where the crack propagates along grain boundaries, often due to defects in or near the grain boundaries such as voids, dislocations, stacking faults or weakening precipitates. A schematic representation of trans- and intergranular crack propagation can be seen in Figure 2.4 below [11].

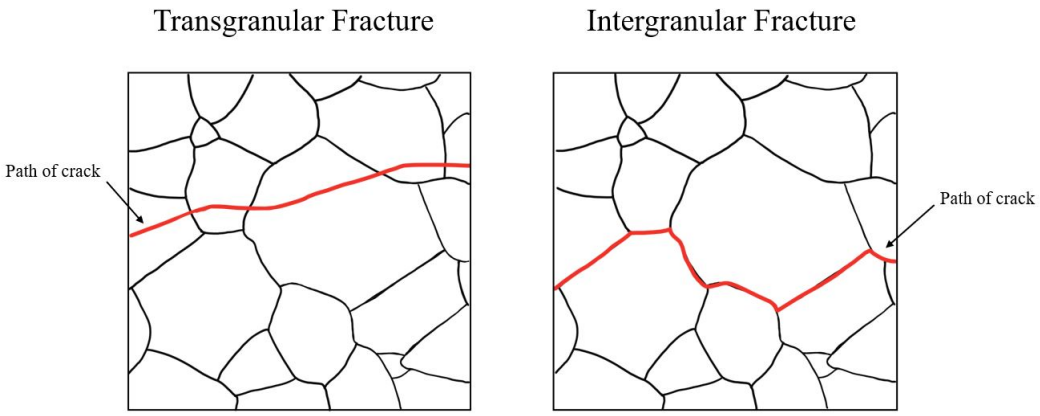

Figure 2.4: Schematic representation of transgranular and intergranular Fracture [8].

2.11 Tensile Test

Tensile testing is a destructive test method for determining a materials mechanical properties such as yield strength, tensile strength and ductility. The test measures the required force to break a material under tension while monitoring the elongation of the test piece.

The test procedure involves placing a specifically shaped test specimen as shown below into a testing rig. A load is then applied uniaxially along the long axis of the specimen which deforms the specimen and ultimately breaks it. The purpose of the specific "dogbone" shape of the test specimens is to confine the deformation to that specific parallel area, controlling where the fracture happens [8].

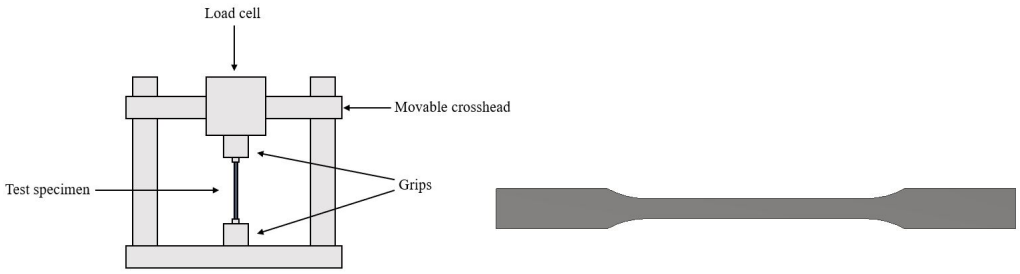

Figure 2.5: Tensile test machine and specimen with the characteristic "dogbone" shape [26].

The test specimens are usually standardized in accordance with ISO standard NS-EN ISO 6892-1:2019 [27] and are circular in cross-section, although standardized rectangular specimens can also be used.

The results of tensile tests are usually given as a plot of engineering stress versus engineering strain as shown in figure 2.6. Engineering stress/strain differs from true stress/strain by using the original cross section and gauge length as opposed to using the instantaneous values. The units for engineering stress are megapascals (MPa) in SI units, while engineering strain is a unitless value, but often expressed as a percentage. The formulas for engineering stress/strain is given below and are hereby referred to as just stress/strain.

Stress (engineering stress) [8]:

$$\sigma = \frac{F}{A_0} \tag{2}$$

where F is the instantaneous load applied perpendicular to the specimen, and A_0 is the original cross-sectional area.

Strain (engineering strain) [8]:

$$\epsilon = \frac{l_i - l_0}{l_0} = \frac{\Delta l}{l_0} \tag{3}$$

where l_0 is the original length, and l_i is the instantaneous length.

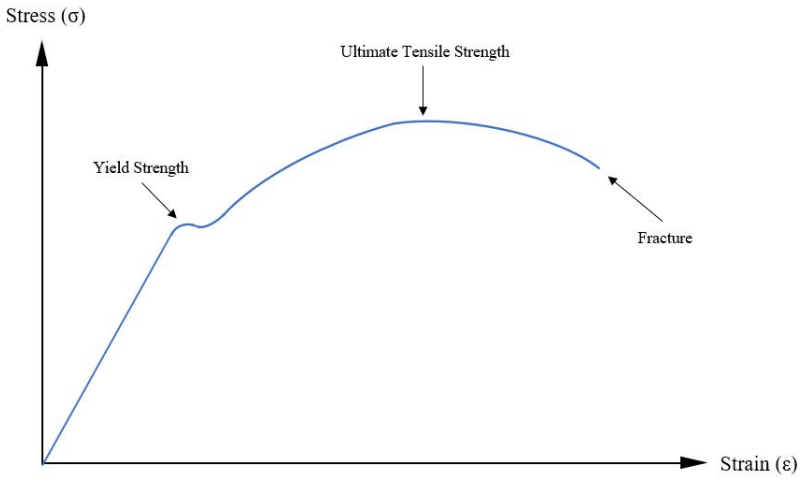

Figure 2.6: Typical stress-strain curve [28]

2.12 Vickers Hardness Test

The Vickers hardness test is a way of determining a materials hardness. It is often referred to as a "microindentation test" and consist of pressing a small diamond shaped indenter into the material with a specific force. The forces used can range from just grams to several kilograms depending on the material that is to be tested [8].

The impression made in the material can then be inspected and the diagonals measured under a microscope. The measurements can then be converted to hardness values manually by using equation 4 or by using software often found in relation to the hardness tester. Figure 2.7, taken from ISO standard NS-EN ISO 6507-1:2018 [29] depicts the indenter, indent and how the diagonals are measured.

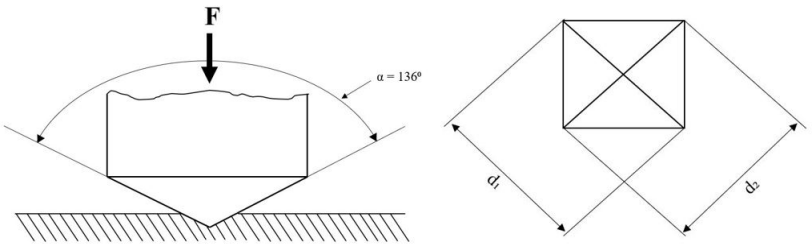

Figure 2.7: Diamond shaped indenter and the corresponding indent made [29].

$$\text{Vickers Hardness} \approx 0.1891 \frac{F}{d^2} \tag{4}$$

where F is the force applied in Newtons, d is the mean of the two diagonals measured in mm and 0.1891 is a calculated factor in relation to the angle α which is 136° [29].

2.13 Optical Microscopy

To investigate the microstructure of a material it is necessary to inspect them in a microscope. Optical microscopes uses light which reflects differently on different parts of the sample being inspected, producing an image in the eyepiece or on a computer screen if it is digitized. A varying degree of magnification can be achieved by mounting different lenses.

Optical microscopy is an important tool in metallurgy as it allows for characterizing materials. By the use of microscopes one can for example determine connections between microstructure and physical properties of a material, or determine if heat treatments and various treatments have been conducted correctly.

2.14 Scanning Electron Microscopy

Scanning Electron Microscopes (SEM) is a microscope that uses electrons to image an area. Electrons are emitted from an electron gun which hits and interacts with a sample. The interaction between the electron and the sample produces different kinds of signals such as secondary electrons, backscatter electrons and characteristic x-rays. These electrons are picked up by a detector and projected on a computer screen. Figure 2.8 below illustrates how the secondary electrons, backscatter electrons and charactheristic x-rays are produced.

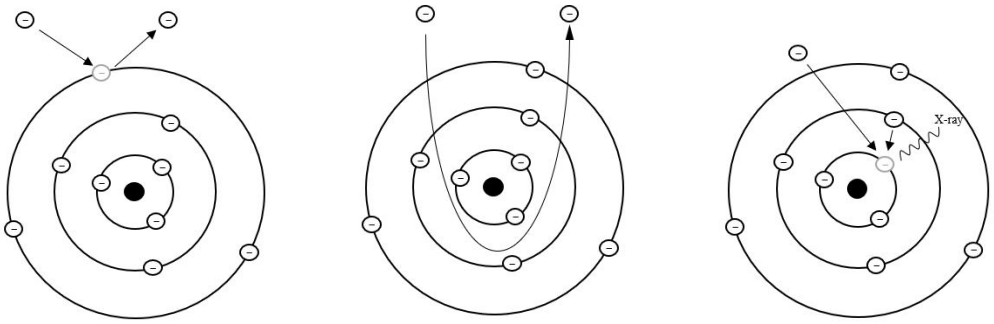

(a) (b) (c)

Figure 2.8: Schematic representation of (a) secondary electrons, (b) backscatter electrons, and (c) characteristic x-rays [30].

The secondary electrons (SE2) are useful for showing topography and morphology of a sample, as it can can have a great depth of field. This is very useful when inspecting fractured surfaces after tensile tests. The backscatter electrons (BSE) are most useful for showing contrast between different phases in a material [31].

SEM imaging allows for a greater depth of focus than optical microscopes, and also have the ability to magnify up to as much as 30,000 times in some cases [31].

2.14.1 EDS

Energy-Dispersive Spectroscopy (EDS) is an analytical method of producing information about the chemical composition of a material including their distribution and concentration. This technique takes use of the characteristic x-rays [32] emitted from the sample.

The characteristic x-rays are produced by the electron beam that hits an electron in the inner shell of an atom in the sample knocking it out. An electron from the outer shell with high energy fills the vacancy of the inner shell with lower energy, and this difference in energy is released in the form of characteristic x-rays. As different elements holds an unique amount of energy, it can be used to quantitatively and qualitatively identify elements and measure the fraction [32]. The data is plotted on a spectrum where the x-axis corresponds to the energy and the y-axis corresponds to the counts of x-rays. This produces a plot where distinct peaks correlate with specific elements. An example of an EDS spectrum produced by the author can be seen below in Figure 2.9 [33].

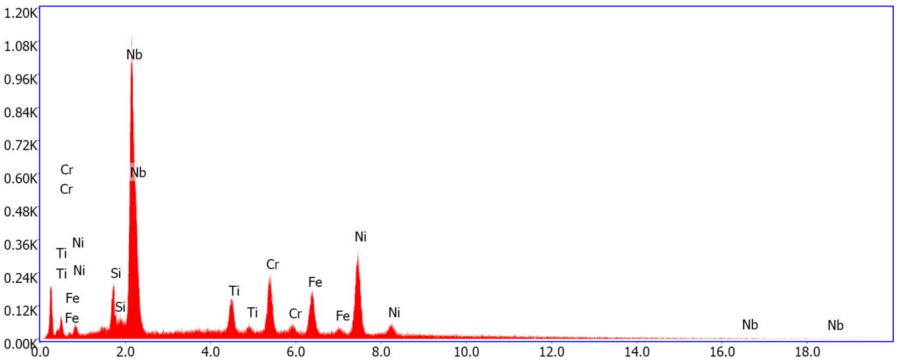

Figure 2.9: Example of an EDS spectrum.

2.14.2 EBSD

EBSD can quantitatively provide crystallographic information about a number of materials such as metals and minerals. It can be used to determine several aspects of a material including phase identification, grain size, grain orientation and texture (degree of crystallographic preferred orientation) and more [34].

EBSD works by pointing the electron gun at a sample that is tilted around 70° with the horizontal axis and inserting an EBSD detector with a phosphor screen up to it. Electrons hit the sample where some of them scatter back due to eliastic collisions (backscatter electrons). As these electrons leave the sample, they interact with the lattice planes in the sample where some diffracts satisfying Bragg's Law presented in Equation 5 below [35].

$$n\lambda = 2dsin\theta \tag{5}$$

Where n is an integer, λ is the wavelength of the electrons, d is the spacing of the diffracted plane and θ is the angle of incidence on the diffracting plane.

These diffracted electrons create a group of paired large angle cones that match with each diffracting plane forming the characteristic Kikuchi bands (diffraction patterns)(seen below in Figure 2.10) on the phosphor screen [35]. The diffraction patterns is then interpreted and indexed with software containing a database of crystallographic patterns.

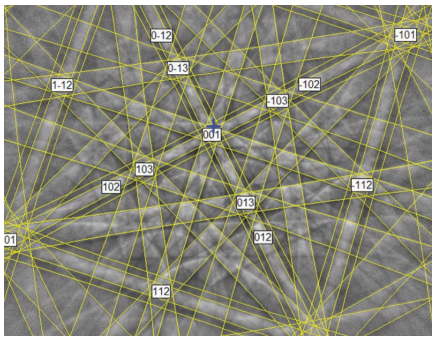

Figure 2.10: Example of a diffraction pattern [36].

3 Experimental

3.1 Prehistory of the Material

The 7/8" studbolts that was provided for this thesis by Scandinavian Fittings and Flanges (SFF) was already a finished product that could have gone into service. This meant that they had undergone fabrication processes such as cold working and precipitation hardening which had induced a great deal of stresses into the material.

The material was produced by VIM+VAR (vacuum induction melting + vacuum arc remelting) melting method by the fabricator, solution annealed at 1030°C for 1.5h followed by water quench. It was then age hardened at 780°C for 6.3h followed by air cooling. The threads was then formed by cold rolling.

To minimize the effects of the history of the material, it was decided to solution heat treat (SHT) the studbolts in order to normalize it and to start with a more or less homogeneous material. The stress relieving and SHT procedure will be discussed later in Chapter 3.4.

3.2 Sample Orientation and Abbreviations

In order for the reader to easier understand the experimental procedures conducted in this theses, some figures and abbreviations have been made. The figures provide a visual representation of the orientation of the samples and the important directions and faces mentioned throughout the thesis.

Figure 3.1 below show the studbolt with its corresponding global xyz coordinate system. Arrows indicate important faces namely the inner and outer face that will be mentioned in the next chapters.

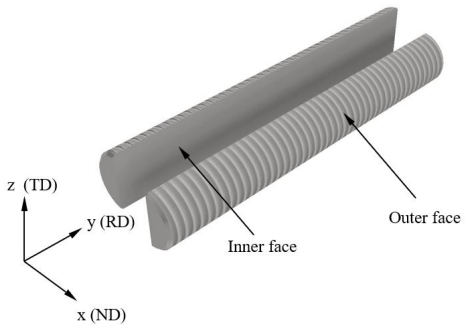

Figure 3.1: Visual representation of important faces and global coordinate system.

Figure 3.2 below shows a sample with another local coordinate system which will be useful when discussing the microstructure later in Chapter 4 and 5. The hatched faces in the figure is the primarily investigated face. This face is located at the RD-ND plane where RD is the Rolling Direction and ND is the Normal direction. The third axis TD on the left figure refers to the Transverse Direction.

Note the correspondence between the global and local coordinate system, where the normal direction correspond with x (ND‖x), Rolling direction corresponds with y (RD‖y) and transverse direction corresponds with z (TD‖z).

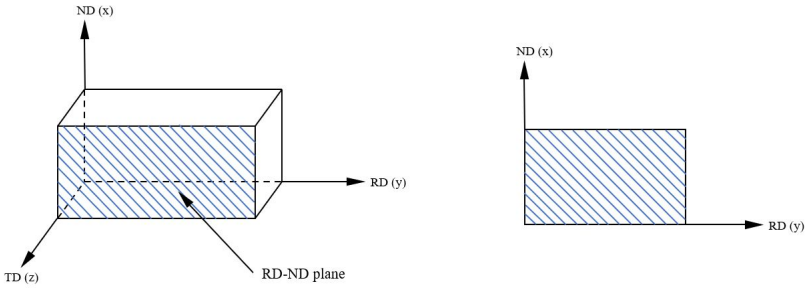

Figure 3.2: 3D and 2D representation of the RD-ND face.

Some abbreviances for the samples have also been created to easier refer to specific samples . In this thesis the abbreviation PH (Precipitation hardened) refers to the precipitaion hardening, while D refers to deformation (deformed). For example the sample named 50D refers to 50% cold rolling reduction with no precipitiation hardening, while 50DPH refers to 50% cold rolling reduction with precipitation hardening. Table 3.1 below shows sample names and the treatments it has received.

Table 3.1: Sample names and their corresponding treatment

Sample name	Cold rolling reduction (%)	SHT	Precipitation hardening
0D	0	Yes	No
0DPH	0	Yes	Yes
20D	20	Yes	No
20DPH	20	Yes	Yes
50D	50	Yes	No
50DPH	50	Yes	Yes

As it can be seen in the table above, six material states have been prepared and tested in this thesis. Namely two different heat treatments (precipitation hardening and no precipitation hardening) for each of the three degrees of deformation.

3.3 Sample Preparation

Figure 3.3 below shows a visual presentation of the processes that has been done to the material to produce tensile samples of the studbolts. Samples for microscopy, both optical and SEM was saved at two different stages of the process, namely before and after precipitation hardening.

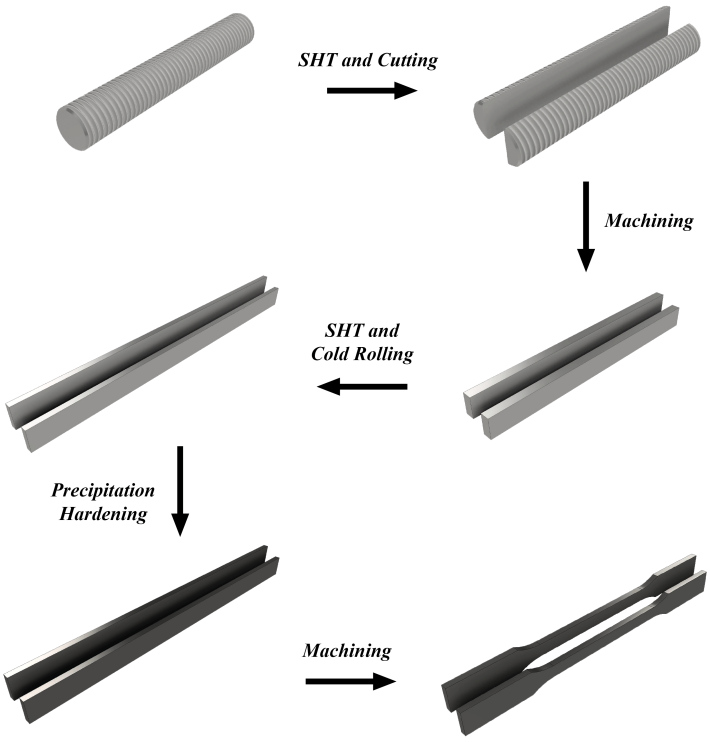

Figure 3.3: Schematic of the sample preparation process.

As explained earlier in Chapter 3.1 the first step in the process was to stress-relieve the material by solution heat treatment (Chapter 3.4). Following that, the studbolts were split in half in the y-direction using a Struers Discotom-10 with the the suitable cutting wheel Struers 66A25.

The halves of the bolts was then placed in a vice on a Somatec mill with the outer face facing up with the intention of milling the outer face parallel to the inner face. The workpiece was then rotated around the y-axis in the vice and milled to essentially a rectangular shape as it can be seen in Figure 3.3.

Although low spindle speed, low feed rate and milling inserts designed to be used for Inconel on the facemill was used, the material still experienced some warping/bending. This left the now rectangular work piece slightly uneven in thickness. Measurements of the testpieces was taken at three different locations to establish the geometry of the testpieces prior to cold rolling. Figure 3.4 shows where the measurements was taken with the dimensions of the testpieces specified in Table 3.2 below.

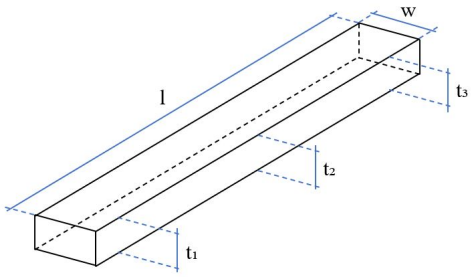

Figure 3.4: Test piece geometry and measurement location.

Table 3.2: Dimensions of the test pieces after milling, prior to cold rolling

Sample name	t_1	t_2	t_3	Avg thickness	l	w
1	5.32	4.70	5.21	5.08	134	14.29
2	5.30	5.08	5.27	5.22	135	9.33
3	5.27	5.05	5.29	5.20	135	9.50
4	5.75	5.76	5.80	5.77	145	12.77
5	5.60	5.77	5.62	5.66	145	12.81
6	5.30	4.93	5.50	5.24	145	14.22
7	5.47	5.92	5.36	5.25	145	14.25

The subsequent heat treatments and cold rolling process is discussed in the next chapters.

3.4 Heat Treatments

Two different types of heat treatments were conducted in this thesis, namely a solution heat treatment to homogenize the microstructure and increase vacancy concentration, and a two-step precipitation hardening heat treatment to induce strengthening precipitates and phases in the material.

For the solution heat treatment a Nabertherm furnace used were set to 1100°C and left to preheat. All the samples were then placed on a tray outside the furnace to be able to quickly place them inside the furnace without loosing too much heat. After one hour the samples were quenched in water.

The two-step precipitation hardening treatment was conducted in the same furnace. The furnace was programmed to preheat to 720°C and stay there for 8 hours. After

the 8 hours, the furnace was set to cool down to 650° and stay at that temperature for another 8 hours. For this heat treatment all samples were also placed on a tray outside the furnace. Once it had reached specified temperature and stabilized, the tray was quickly placed inside. Once the first 8 hours was over, the samples was left inside to furnace cool. The cooling rate was measured to be approximately -186°C/h (shown in Appendix C). Once held at 650°C for another 8 hours, the samples were removed from the furnace and left to air cool to room temperature.

Figure 3.5 below shows graphically the heat treatments conducted in this thesis. The graph is not in scale, and should be used as a visual guide of the heat treatments only.

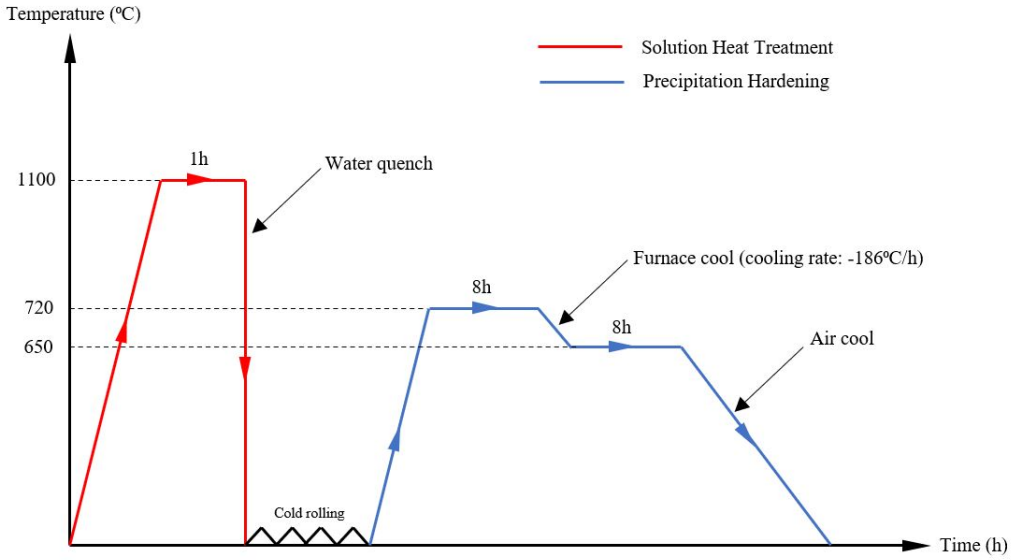

Figure 3.5: Schematics of SHT and precipitation hardening process used in this thesis.

3.5 Cold Working

In this thesis it was decided to investigate the effects cold rolling had on the material. By that, three degrees of deformation was chosen. Namely 0% (undeformed), 20% and 50% reduction of thickness.

The cold rolling were conducted on a Schmitz cold rolling mill located in the UiS workshop. The process was started quickly after SHT to minimize the effects of age hardening on the material, if any. The testpieces were also sanded prior to cold rolling to remove the black oxide layer that had formed during SHT.

Several passes in the cold rolling mill had to be done in order to achieve the desired degree of deformation. Since the testpieces were slightly uneven in thickness, an average thickness of the testpiece was calculated using measurements from t1, t2 and t3. This number was also used to calculate the desired final thickness determining the exact degree of deformation.

For each pass, the machine was adjusted 0.2mm narrower than the last pass. Measurements between each pass were done with a digital caliper at three different locations (t1, t2, t3) specified earlier in Chapter 3.3. Due to the mechanics of the mill and its state it was difficult to precisely reduce the thickness each pass. The precision also relied on the ability to measure precisely.

Final thickness and degree of deformation can be seen in Table 3.3 below, while the full log of passes and measurements can be found in Appendix B.

Table 3.3: Degree of deformation achieved on the basis of average thickness. Three testpieces reduced by 20% named 20def, and three testpieces reduced by 50% named 50def

Sample name	Starting thickness	Final thickness	Degree of deformation
20def1	5.22 mm	4.17 mm	20.11%
20def2	5.20 mm	4.15 mm	20.19%
20def3	5.77 mm	4.62 mm	19.93%
50def1	5.66 mm	2.81 mm	50.35%
50def2	5.24 mm	2.59 mm	50.57%
50def3	5.25 mm	2.59 mm	50.67%

3.6 Microscopy Preparation

A total of six material states was to be investigated in this thesis. Two samples for each degree of deformation, with and without precipitation hardening. These samples had been cut of the testpieces at various times of the preparation process. The cuts were made with a Struers Discotom-10 with an appropriate cutting wheel and plenty of cooling liquid to ensure no excessive heat generation.

The samples was then embedded in Struers Polyfast, which is a bakelite resin with carbon filler using a Struers CitoPress-30 hot mounting machine. This was done so the samples could be mounted in a specimen holder during grinding and polishing ensuring a completely flat surface. The Polyfast resin is also conductive which makes it suitable for SEM examination.

Wet grinding and diamond polishing was then done to prepare the samples for microscopic investigations. This was done on a Struers TegraPol-35 automatic

polisher with a connected Struers TegraDoser-5 unit ensuring correct dosage of polishing compound. The sample holder with all the samples was also removed between each step and cleaned in a Struers Lavamin ultrasonic cleaner. Table 3.4 below show the grinding and polishing steps.

Table 3.4: Grinding and polishing sequence

Disc	Grit	Suspension	Time
SiC	P120	Water	3m
SiC	P320	Water	3m
SiC	P500	Water	3m
SiC	P1000	Water	3m
SiC	P1200	Water	3m
SiC	P2400	Water	3m
Allegro	9 μm	Allegro/Largo	5m
Mol	3 μm	Mol	5m
Nap	1 μm	Nap-B	5m
Chem OP-S	0.25 μm	OP-S	6m

3.7 Tensile Test

The amount of material on hand only allowed for a total of seven tensile test specimens. Three samples that was 20% deformed, three sampled that was 50% deformed, and one undeformed sample.

Due to the size of the material stock, a standardized geometry of the tensile test specimens could not be achieved. Also since the test pieces had slightly different thicknesses prior to rolling, meant that the tensile specimens would have varying thickness within the same degree of deformation as ISO standard 6892-1:2019 [27] specified that for rolled samples, the surface should not be machined.

A rectangular geometry of the specimens had to be used in this thesis. The reduced parallel area was machined on a Mazak CNC within the specifications of the drawing shown below in Figure 3.6.

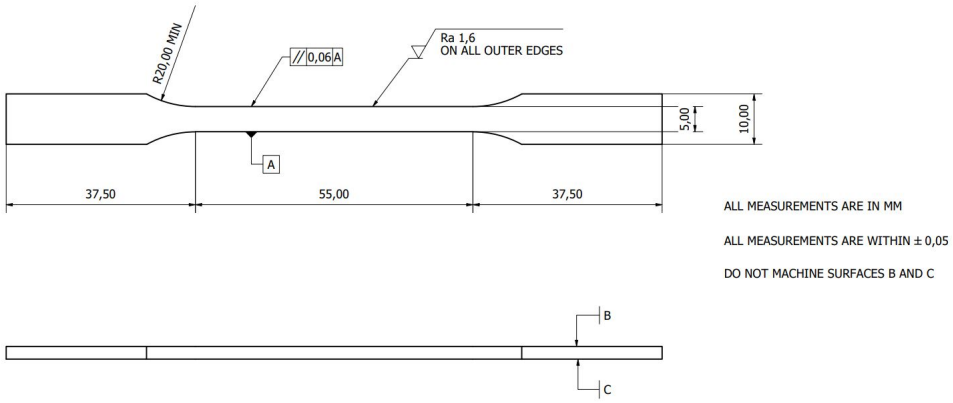

Figure 3.6: Tensile test specimen geometry.

The tensile tests were conducted on a Instron 5985 universial testing machine in accordance with test method A1 in ISO standard NS-EN ISO 6892-1:2019 [27] with a strain rate of 0.00025 $s^{-}1$ at room temperature.

An external clip-on extensiometer was used to measure the elongation up to the yield strength. The test was then paused, the extensiometer removed, and the test resumed. This should not affect the results of the tensile tests, although it leaves a small notch in the stress-strain curves which can be seen in Chapter 4.2.

3.8 Hardness Test

All the six material states listed in Table 3.1 in Chapter 3.2 was tested for hardness. Although the hardness in itself is interesting, the hardness test was also done to confirm that the cold rolling had been correctly executed. It was feared that the constant reduction of thickness during cold rolling had been to small, which could result in uneven deformation through the cross-section and ultimately a decreased hardness in the core of the material.

The hardness test was conducted on the RD-ND plane referenced in Figure 3.2. This was to see the effects of the cold rolling on the entire cross section of the sample. The samples were small in size, so to be able to collect enough data the load was set to 5kg (HV5), since this left relatively small imprints. Preliminary test imprints was done in the corner of each sample to determine the average length of the two diagonals. This was needed to ensure that the imprints were spaced correctly as ISO standard ISO 6507-01 [29] stated that imprints should be done 2.5d (avg. diameter) from the edge and spaced with 3d between each other.

The hardness tests was done on a Innovatest automatic hardness tester with the Vickers test method. This allowed a large number of imprints to be done in a controlled and accurate manner. The six samples were polished in accordance with Table 3.4 in Chapter 3.6 only skipping the last step (OP-S) to ensure a flat and scratch free surface and mounted in the vise on the hardness tester. Due to differences in sample size, there was some variation in number of imprints between each sample. Below in Table 3.5 and the according Figure 3.7 the number of

imprints and their locations can be seen.

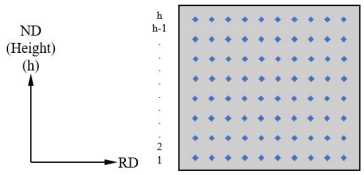

Figure 3.7: Visual representation of location of hardness imprints.

Table 3.5: Amount of HV imprints for the specific samples

Sample name	Total imprints	Imprints at each height
0D	79	11
0DPH	100	10
20D	98	14
20DPH	100	10
50D	80	16
50DPH	85	17

Studying the effects of cold rolling throughout the thickness of the material was desired, but since the size of the samples varied, the number of imprints at each "height" in the Normal Direction also varied. Although only 10-17 imprints depending on the sample was achieved at each height in the normal direction, it would still be enough to show the hardness trends throughout the thickness.

The specific locations of the different heights in the samples is not particularly important as long as the imprints at one height was done at the same height along the Rolling Direction. The different heights was merely a way of determining difference in hardness throughout the thickness of the material.

3.9 Optical Microscopy

To see the general microstructure of the material an metallurgical microscope was used. Namely an Olympus GX53. Samples for each material state, six in total, was prepared by following the procedure described earlier in chapter 3.6 and studied in the microscope.

3.10 Scanning Electron Microscopy

High magnification imaging, as well as EDS analysis and EBSD was done on a Zeiss Supra 35VP Scanning electron microscope. To be able to see the effects of cold rolling, the samples was mounted in Polyfast epoxy as described in chapter 3.6 showing the RD-ND plane. The samples was ground and polished according to Table 3.4 in Chapter 3.6, finishing with OP-S. No etching was required for SEM-imaging.

The ordinary SEM images was taken using the backscatter electrons, producing a good depth of field. EDS analysis was also done to determine the chemical composition of the matrix, as well as precipitates found in the microstructure. An EBSD scan of the samples was also done to more clearly see the grain structure as the ordinary backscatter images had difficulty producing good images on the samples with a high degree of deformation. The EBSD analysis also made it possible to see the grains rearranging in the rolling direction and the average grain size of the different samples.

Data for the EBSD scans were gathered using a NORDIF camera with accompanying EDAX OIM Data Collection software for indexing, while the production of maps and figures was conducted with EDAX OIM Analysis software.

4 Results

In this chapter results from the mechanical testing will be presented. This includes the following:

- Hardness
- Yield strength
- Ultimate tensile strength
- Elongation

Along with mechanical tests, microstructural analysis have also been conducted with the aid of optical light microscopy and scanning electron microscopy and includes the following:

- General microstructure
- Chemical composition by EDS
- Grain arrangement and texture by EBSD

4.1 Hardness

All hardness tests have been conducted in the RD-ND plane as specified in Chapter 3.8. The results are processed and presented as plots and tables in this chapter, discussed further in Chapter 5 while the complete data are given in Appendix G. Figure 4.1 shows graphically what is referred to as the height of the samples. The

heights are evenly spaced over the sample surface with spacing calculated based on the diagonals. As the size of each sample varied, the number of heights also varied.

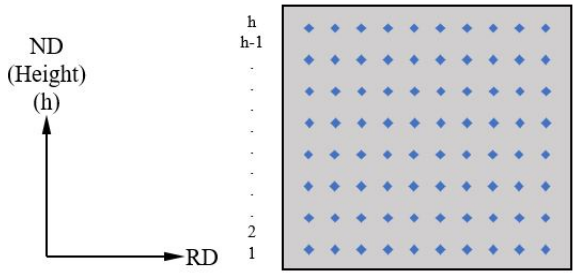

Figure 4.1: Visual aid for location of HV imprints.

4.1.1 Undeformed Samples

Table 4.1 shows the total average hardness and standard deviation for sample 0D and 0DPH. Figure 4.2 graphically show the varying hardness throughout the thickness of the material. The x-axis represent the different heights of the sample, while the y-axis shows HV. The complete table of hardness values are found in Appendix D.

Table 4.1: Average hardness results for undeformed samples

Sample name	Average	SD
0D	165.46	4.58
0DPH	430.07	11.33

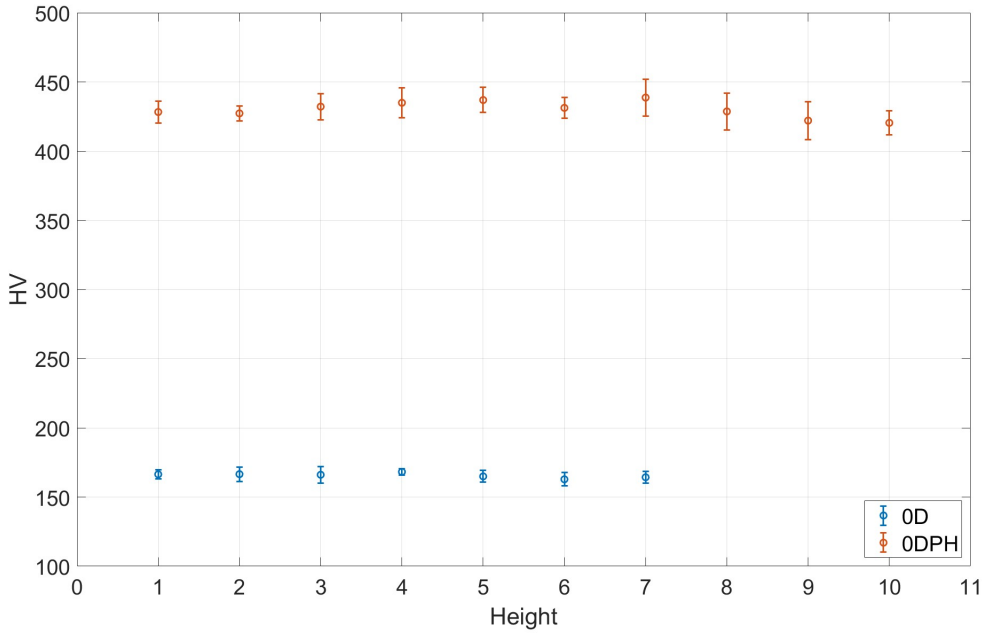

Figure 4.2: Plot of hardness based on height for the undeformed samples. The x-axis represents the different heights, y-axis represents HV.

As it can be seen from Table 4.1, the precipitation hardening treatment has had a major impact on the hardness of the sample. The average hardness for sample 0D is 165.46HV with a standard deviation of 4.58, while sample ODPH yielded an average hardness of 430.07HV with a standard deviation of 11.33. This corresponds to a difference in hardness of 264.61HV which is in turn a 61.52% increase only due to the precipitation hardening process.

Sample 0D shows quite a homogeneous hardness showing only small differences in average hardness at each height. The highest and lowest average hardness values, 168.20 and 162.81, differs only with 2.47HV and 2.65HV respectively from the global average hardness value of 165.46. This corresponds to a difference of 1.5%

and 1.6% difference in hardness from the total average.

Sample 0DPH shows a larger difference in hardness throughout the thickness of the sample where the highest and lowest average values are 438.71HV and 420.42HV respectively. Table 4.1 shows a total average hardness of 430.07HV with a standard deviation of 11.33 which leads to a difference of 8.64HV and 9.65HV from the highest and lowest values based on height. This corresponds to a difference of 2% and 2.2% for the highest and lowest values compared to the total average.

4.1.2 20% deformed

Similarly as the undeformed samples, the precipitation hardening process has had a major impact on the materials hardness in the 20% deformed state. Shown in Table 4.2 below, the average hardness of sample 20D is 290.64HV with a standard deviation of 14.87, while the precipitation hardened sample 20DPH is increased to an average hardness of 472.10HV with a standard deviation of 12.25. This results in a 181.46HV increase in average hardness by precipitation hardening which corresponds to 62.43%.

The standard deviation might seem high, although it only corresponds to a 5.13% and 2.59% deviation from the average in hardness for sample 20D and 20DPH respectively.

Table 4.2: Average hardness results for 20% deformed samples

Sample name	Average	SD
20D	290.64	14.87
20DPH	472.10	12.25

Figure 4.3 below graphically show the average hardness for each height in the samples. The complete set of hardness data are found in Appendix D.

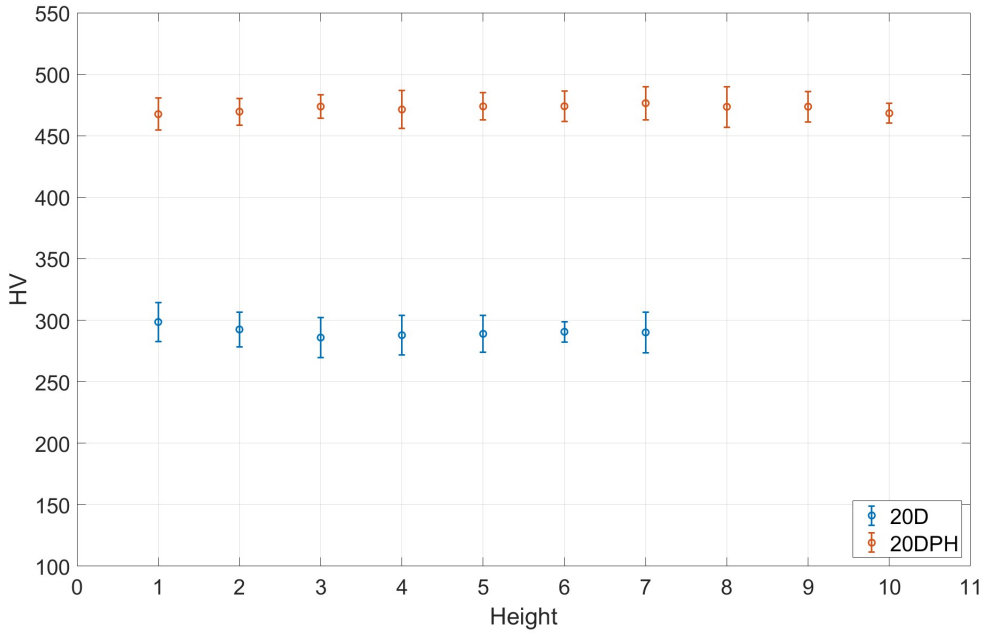

Figure 4.3: Plot of hardness based on height for the 20% deformed samples. The x-axis represents the different heights, y-axis represents HV.

For sample 20D the highest and lowest values are 298.56HV with a standard deviation of 15.94 and 285.90HV with a standard deviation of 16.47 respectively. This corresponds to a difference of 2.73% and 1.63% for the highest and lowest average hardness to the total average hardness. This tells us that the hardness is

more or less uniform throughout the thickness of the sample.

For sample 20DPH the highest average value was found to be 476.46Hv with standard deviation equal to 13.51, while the lowest average hardness was 467.55Hv with a standard deviation of 13.06. This resulted in a difference with the total average of 0.92% for the highest average value specific to height and 0.97% with the lowest average value specific to height. This shows that the 20% deformed samples varied little in hardness at different heights compared to the overall hardness of the sample.

4.1.3 50% deformed

Although precipitation hardening also has had a major impact on the hardness of the 50% deformed samples, it has not increased to a similar extent as the two other material states. As shown in Table4.3, sample 50D achieved an average hardness of 416.57HV with a standard deviation equal to 15.06, while precipitation hardening alone increased the average hardness of sample 50DPH to 528.19Hv with a standard deviation of 13.38. This equals an increase of 111.16HV which corresponds to a 26.8% increase.

Table 4.3: Average hardness results for 50% deformed samples

Sample name	Average	SD
50D	416.57	15.06
50DPH	528.19	13.38

Figure 4.4 graphically show the average hardness at each height in the samples. The complete set of hardness data corresponding to height can be found in Appendix D.

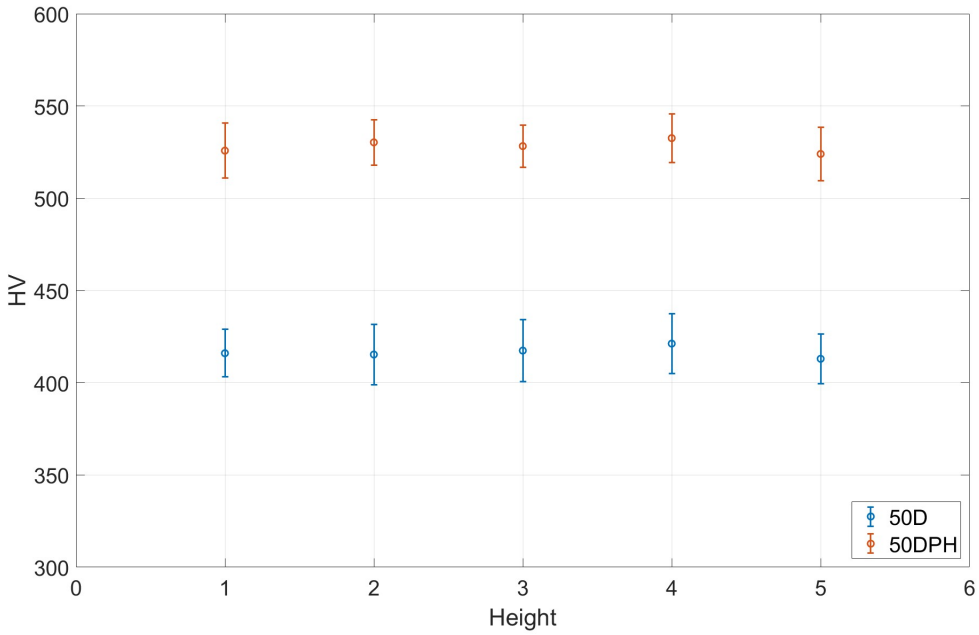

Figure 4.4: Plot of hardness based on height for the 50% deformed samples. The x-axis represents the different heights, y-axis represents HV.

The highest and lowest values for sample 50D was found to be 421.20Hv with a standard deviation of 16.15 and 412.97HV with a standard deviation equal to 13.48 respectively. Comparing the highest average hardness specific to height with the sample average, it corresponds to a difference of 1.11%. Comparing the lowest average value specific to height the difference is 0.87%.

For sample 50DPH the highest and lowest average value specific to height was found to be 532.58HV with a standard deviation of 13.22 and 524.01HV with a

standard deviation equal to 14.41 respectively. This resulted in a difference with the sample average of 0.83% and 0.80% for the highest and lowest height specific average values respectively. This again showed that the hardness specific to height varied very little in comparison with the total sample average resulting in a quite uniform hardness throughout the thickness.

4.1.4 Comparison

Comparing samples that have undergone the same treatment allows for comparing the effects deformation in the form of cold rolling and precipitation hardening separately from each other. Table 4.4 below shows all average hardness results with their corresponding standard deviation. Figures 4.5 and 4.6 represents the same results in a graphical manner.

Table 4.4: Comparison of average hardness and standard deviation for all samples

	0D	0DPH	20D	20DPH	50D	50DPH
Avg HV	165	430	291	472	417	528
SD	4.58	11.33	14.87	12.25	15.06	13.38

Samples 0D, 20D and 50D have not received precipitation hardening (PH). As can be seen from Table 4.4 the hardness increased with increasing degree of deformation. Sample 0D which is undeformed achieved an hardness of 165HV which is the lowest of all samples. Sample 20D is 20% deformed and reached a value of 291HV. This is a 74.6% increase in hardness from sample 0D. Sample 50D is 50% deformed and reched a value of 417HV. This is a 43.3% increase from

sample 20D. The total difference in hardness attributed to deformation alone can be found when comparing sample 0D and 50D. By deforming the samples 50%, the hardness increased by 252HV which corresponds to a 152.7% increase.

Samples 0DPH, 20DPH and 50DPH have all received a precipitation hardening treatment after cold rolling. The hardness for 0DPH, 20DPH and 50DPH reached values of 430HV, 472HV and 528HV respectively which can also be seen in Table 4.4. Comparing sample 0D with 0DPH will show the increase in hardness due to precipitation hardening. The difference in hardness was an increase of 160.6%. The increase between 20D and 20DPH was 62.2%, and the increase between 50D and 50DPH was 26.6%.

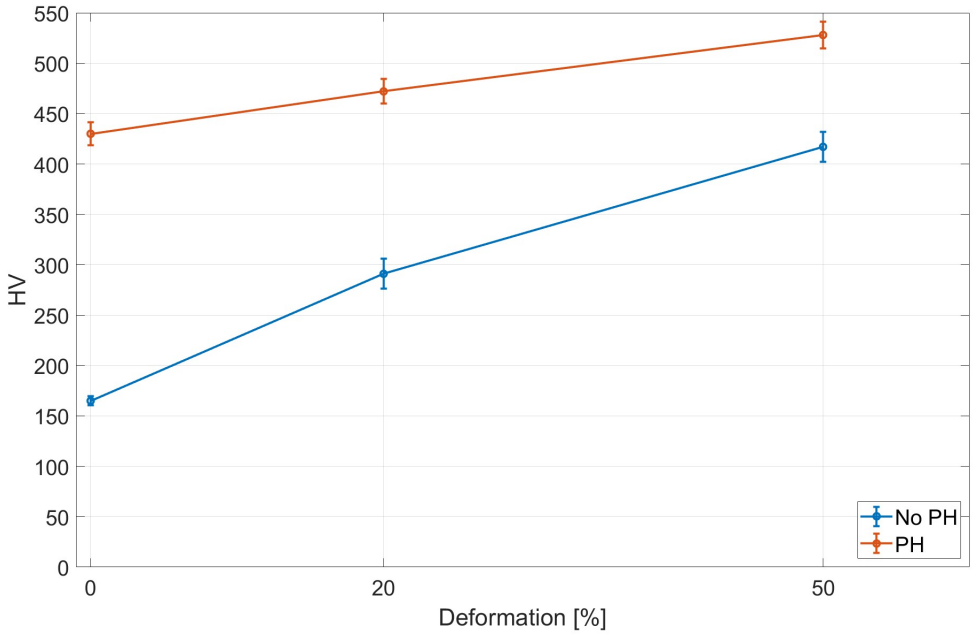

Figure 4.5: Graphical representation of HV results. The x-axis represents degree of deformation, the y-axis shows HV.

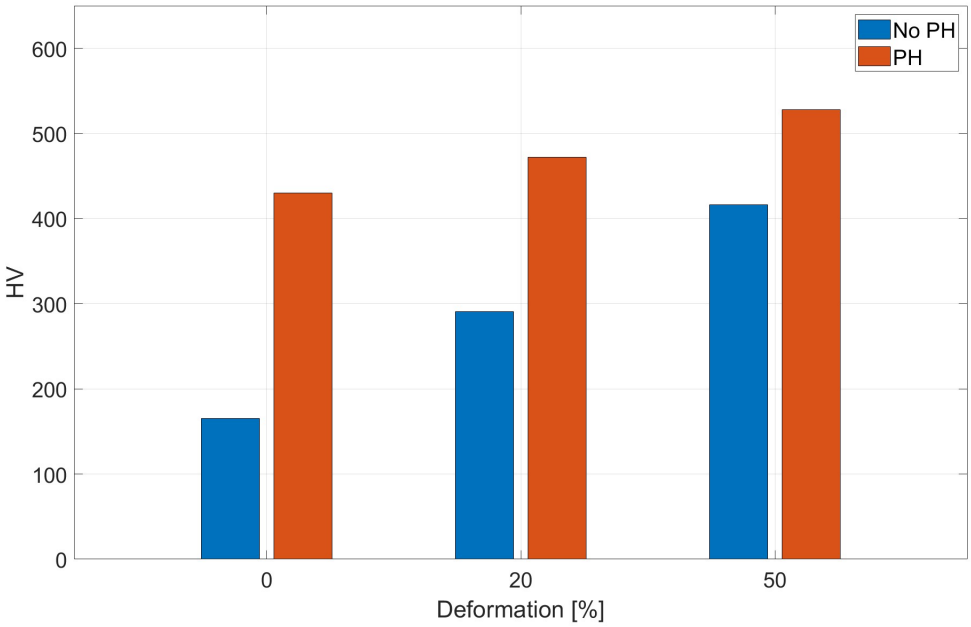

Figure 4.6: Additional visual presentation of hardness by bar plot. The x-axis represents degree of deformation, the y-axis shows HV.

4.2 Tensile Tests

In this chapter results from the seven tensile tests will be presented and compared to each other both in graphical manner in the form of graphs, and with tables. The samples have all been equally heat treated, thus only three different material states are present, namely undeformed, 20% deformed and 50% deformed. Yield strengths and ultimate tensile strength will be listed in the tables along with the specific samples elongation.

Figure 4.7 below shows a plot of all samples that was tested. Three samples of the 50DPH state, three samples of the 20DPH state, and one sample in the 0DPH state.

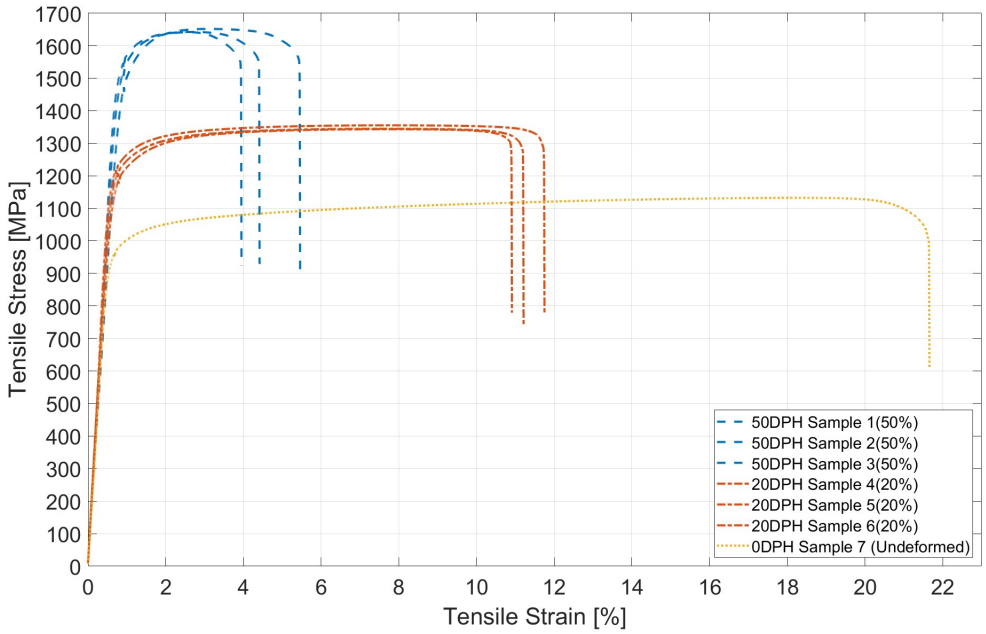

Figure 4.7: Plot of all tensile tests conducted. The x-axis represents % elongation, the y-axis shows tensile stress in MPa.

The tables below present the results from the tensile tests. Table 4.5 shows the results for the undeformed sample 0DPH. Table 4.6 shows results for the 20% deformed samples 20DPH and Table 4.7 shows the results for the 50% deformed samples 50DPH.

- $R_p0.2$: Yield Strength at 0.2% offset
- R_m: Ultimate Tensile Strength
- E: Youngs' Modulus (Modulus of Elasticity)

Table 4.5: Tesile results for undeformed sample (0DPH)

Sample name	$R_p0.2$ [MPa]	R_m [MPa]	Elongation [%]	E [GPa]
0DPH-1	960	1132	21.12	215

Table 4.6: Tesile results for 20% deformed sample (20DPH)

Sample name	$R_p0.2$ [MPa]	R_m [MPa]	Elongation [%]	E [GPa]
20DPH-1	1213 MPa	1355 MPa	11.13%	236
20DPH-2	1187 MPa	1343 MPa	10.19%	202
20DPH-3	1206 MPa	1344 MPa	10.54%	212
20DPH Mean	1202 MPa	1348 MPa	10.62%	217

Table 4.7: Tesile results for 50% deformed sample (50DPH)

Sample name	$R_p0.2$ [MPa]	R_m [MPa]	Elongation [%]	E [GPa]
50DPH-1	1469 MPa	1651 MPa	4.61%	202
50DPH-2	1523 MPa	1641 MPa	3.15%	213
50DPH-3	1543 MPa	1642 MPa	3.68%	236
50DPH Mean	1512 MPa	1654 MPa	3.81%	217

As expected, the sample with the highest degree of deformation showed the highest values for both yield and tensile strength, namely mean values of 1512MPa and 1654MPa respectively. Although achieving only a mean elongation of 3.81%, as was also expected.

Figure 4.8 below shows mean yield and ultimate tensile strength for the different material states in a graphical manner when viewed with the y sccale on the left hand side. The yield strength increased with increasing degree of deformation and ranges from 960MPa for sample 0DPH, to 1202MPa for sample 20DPH, to 1512MPa for sample 50DPH. The Ultimate Tensile Strength also increased with

increasing degree of deformation. This ranged from 1132MPa for sample 0DPH, to 1348MPa for sample 20DPH, to 1654MPa for sample 50DPH.

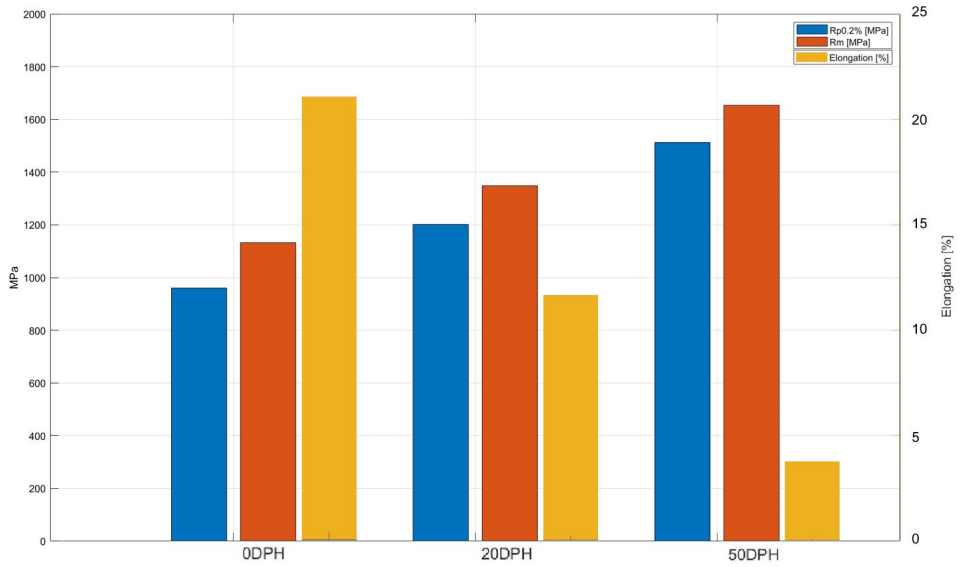

Figure 4.8: Bar plot showing yield strength (blue), ultimate tensile strength (red) and elongation (yellow). Elongation is plotted against the secondary axis on the right side of the plot.

The yellow bars in 4.8 are plotted against the y scale on the right hand side, and show the mean elongation of the samples. The elongation ranged from 21.12% for 0DPH, to 10.62% for 20DPH to 3.81% for 50DPH.

4.3 Optical Microscopy

In this chapter optical microscope images will be presented. All samples were examined using an Olympus GX53 inverted optical light microscope with Stream Essentials software for imaging. All samples were examined in the RD-ND plane as shown in Figure 4.9. The presented images are those determined to be of greatest quality.

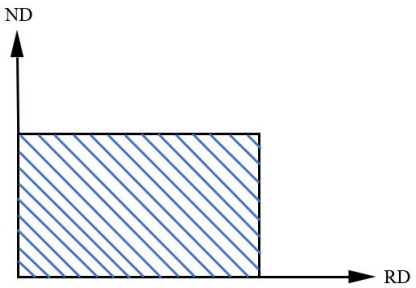

Figure 4.9: Orientation of examined surface.

Figure 4.10 below shows images of sample 0D on the left and 0DPH on the right.

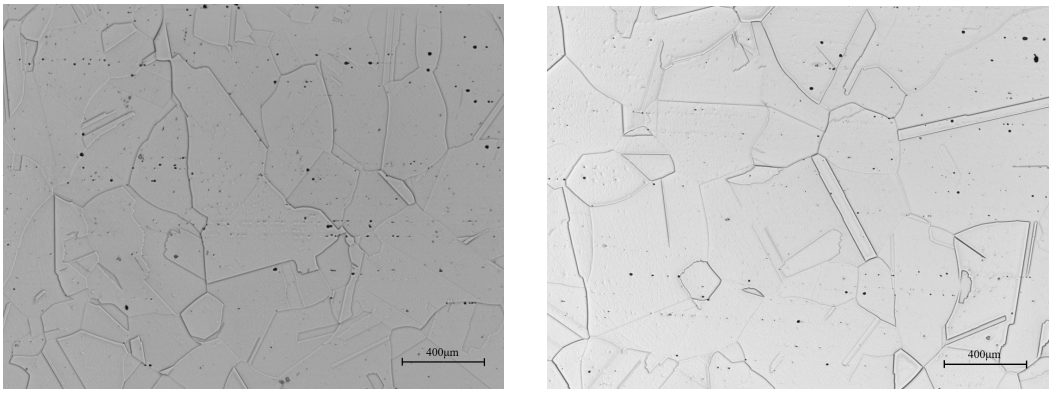

(a) (b)

Figure 4.10: Optical microscope images of sample (a) 0D, and (b) 0DPH. The micron bars shows a length of $400\mu m$.

Sample 0D and 0DPH in Figure 4.10 both show a well defined grain structure with large straight edged grains. The grains appear to be more or less equiaxed. Dark particles were found distributed throughout the whole surface of the samples, which will be discussed further in Chapter 4.4. A large amount of twins were found in the microstructure.

No distinct difference between 0D and 0DPH was found by optical microscopy. The horizontal lines of dark and bright particles are believed to have formed during the manufacturing process of the alloy.

Below, Figure 4.11 shows images of sample 20D on the left and 20DPH on the right.

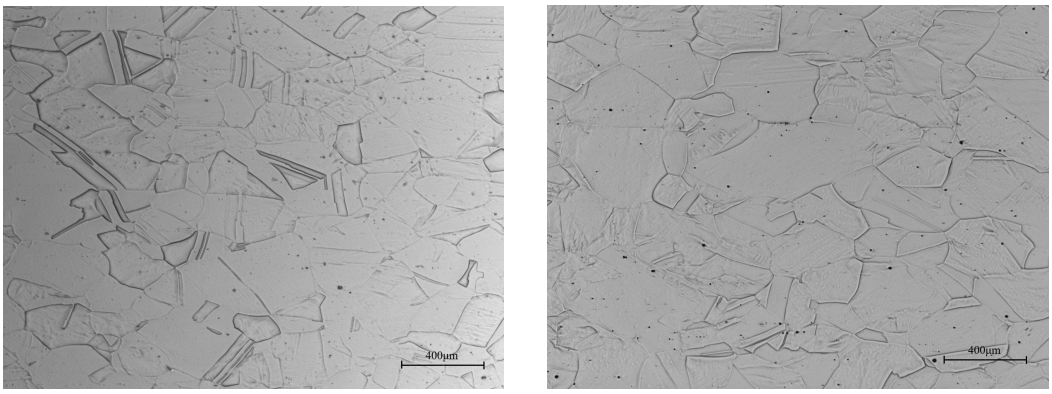

(a) (b)

Figure 4.11: Optical microscope images of sample (a) 20D, and (b) 20DPH. The micron bars shows a length of $400\mu m$.

Sample 20D and 20DPH shown in Figure 4.11 also show a well defined grain structure with a number of twins. Also here the grains appear more or less equiaxed in shape. Even though both samples are deformed 20% it is not clearly visible,

although the grain boundaries do not appear as straight as in the undeformed samples and smaller. No formations of shear bands were found in these samples. Similar dark particles scattered throughout the microstructure as in the undeformed samples were found.

No distinct visible difference between sample 20D and 20DPH was found by optical microscopy examination.

Figure 4.12 below shows images of sample 50D on the left and 50DPH on the right.

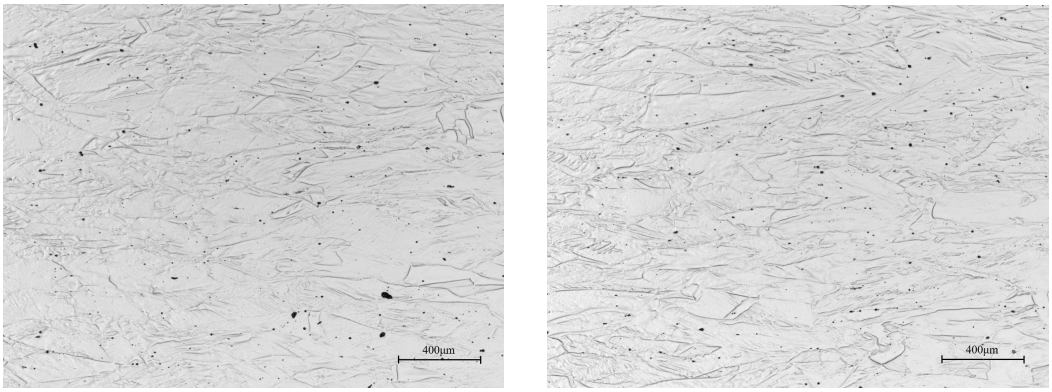

(a) (b)

Figure 4.12: Optical microscope images of sample (a) 50D, and (b) 50DPH. The micron bars shows a length of $400\mu m$.

Both sample 50D and 50DPH i Figure 4.12 shows a highly deformed microstructure with elongated grains in the rolling direction. Dark particles can be seen distributed throughout the samples, which will be discussed further in Chapter 4.4. The images also revealed that shear bands had formed during cold rolling at this degree of deformation, unlike what was found in the 20% deformed samples.

As the precipitation hardening treatment happened well below the recrystallization temperature of the alloy, no distinct difference in microstructure between sample 50D and 50DPH were found with optical microscopy.

4.4 Scanning Electron Microscopy

Results gathered from Scanning Electron Microscopy will be presented in this chapter. The examined surface is the RD-ND plane, similar to the examined surface stated in the previous chapter.

The images selected and shown are those determined to have the greatest quality and provides the most interesting characteristics of the microstructure. A varying degree of magnification is used to highlight specific features more closely. All images were acquired using backscatterd electrons with aperture size of 60 μm, 20kV accelerating voltage and a varying working distance.

Figure 4.13 below shows backscatter images of sample 0D with varying degree of magnification.

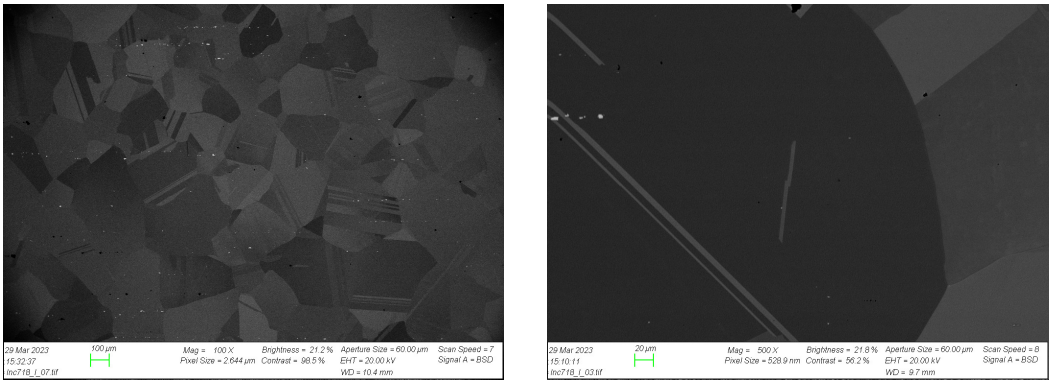

(a) (b)

Figure 4.13: Backscatter images of sample 0D. (a) 100X magnification with 10.4mm working distance, (b) 500X magnification with 9.7mm working distance.

Figure 4.13(a) shows a similar microstructure to that acquired with optical microscopy. Dark and light precipitates are found scattered around the microstructure. Bright particles suggest that the elements it consists of are heavier than those around due to heavier elements reflects more signals to the detector than lighter elements. This will be discussed further in Chapter 4.4.1. The particles seem to have aligned horizontally, and are thought to have formed during the fabrication process of the material.

Figure 4.13(b) shows a high magnification image of grain and twin boundaries with an intergranular twin.

Figure 4.14 below shows backscatter images of sample 0DPH with a varying degree of magnification.

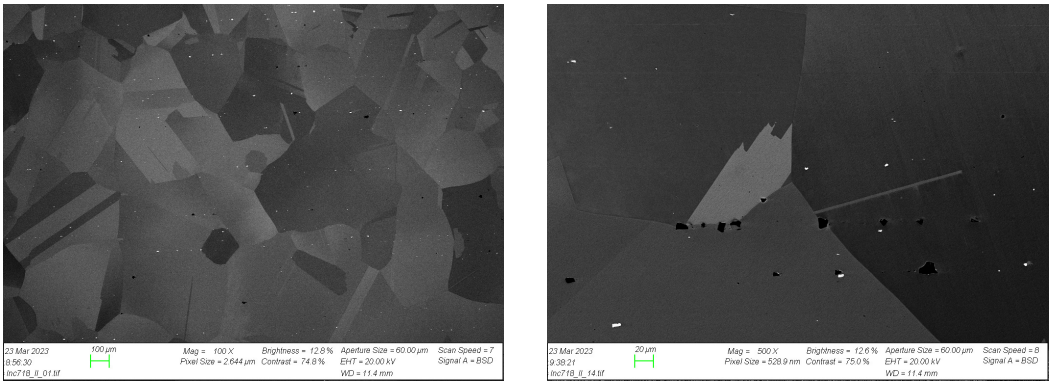

(a) (b)

Figure 4.14: Backscatter images of sample 0DPH. (a) 100X magnification with 11.4mm working distance, (b) 500X magnification with 11.4mm working distance.

Figure 4.14(a) Shows a similar structure as to that of sample 0D with clearly defined grain structure with straight grain boundaries and a number of twins.

Figure 4.14(b) shows dark precipitates have formed both on grain boundaries and intergranularly.

Figure 4.15 below shows backscatter images of sample 20D with a varying degree of magnification.

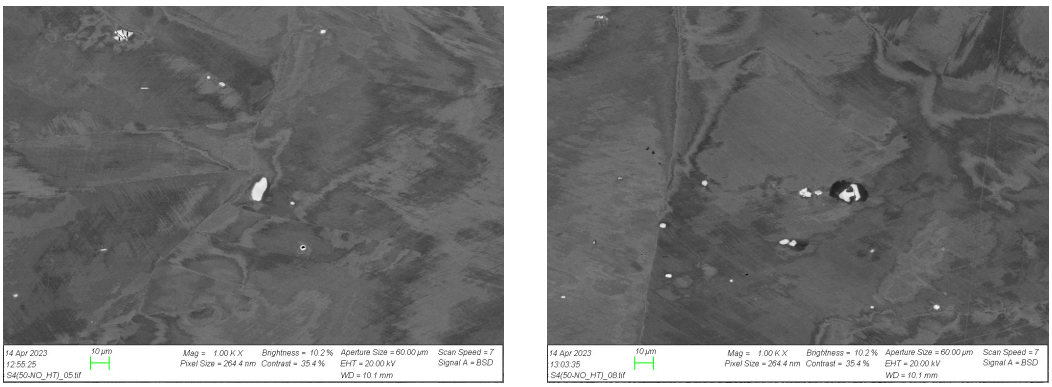

(a) (b)

Figure 4.15: Backscatter images of sample 20D. (a) 1000X magnification with 10.1mm working distance, (b) 1000X magnification with 10.1mm working distance.

The deformed samples proved to be very difficult to acquire good SEM images with both the backscatter electrons and the secondary electrons.

Figure 4.15(a) shows a image of a distorted microstructure due to deformation. This differs from the microstructure images acquired through optical microscopy of the same sample.

Grain boundaries are observed to be more curved than the undeformed samples. The grains also show a non uniform colour which will be discussed further in Chapter 4.5. Both dark and light particles are seen throughout the microstructure. Some of the white particles shows vertical cracks going through them in the direction of the force induced during cold rolling.

Figure 4.16 below shows backscatter images of sample 20DPH with a varying degree of magnification.

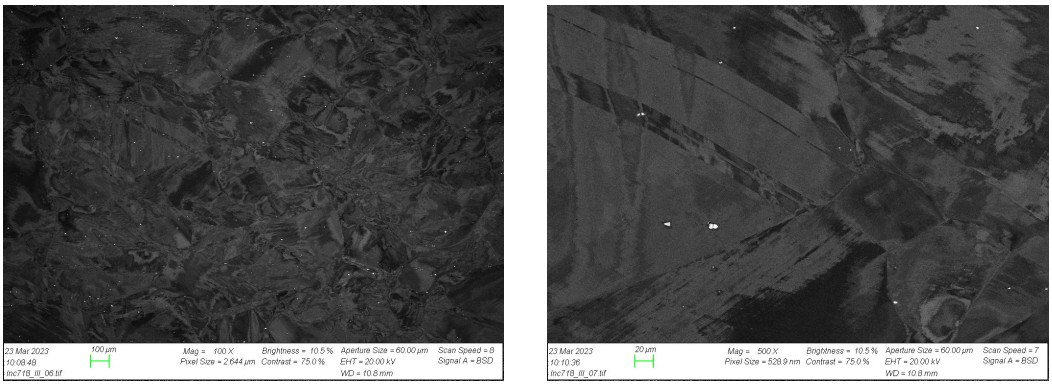

(a) (b)

Figure 4.16: Backscatter images of sample 20DPH. (a) 100X magnification with 10.8mm working distance, (b) 500X magnification with 10.8mm working distance.

Also here in Figure 4.16(a) the SEM images reveal a highly distorted microstructure as opposed to images acquired of the same material state by optical microscopy. The grain structure is unclear with different shades of colour within each grain. Also here, dark and bright particles are scattered throughout the entirety of the sample where some of the bright particles also appear to be cracked in the vertical direction.

Figure 4.17 below shows backscatter images of sample 50D with different magnifications.

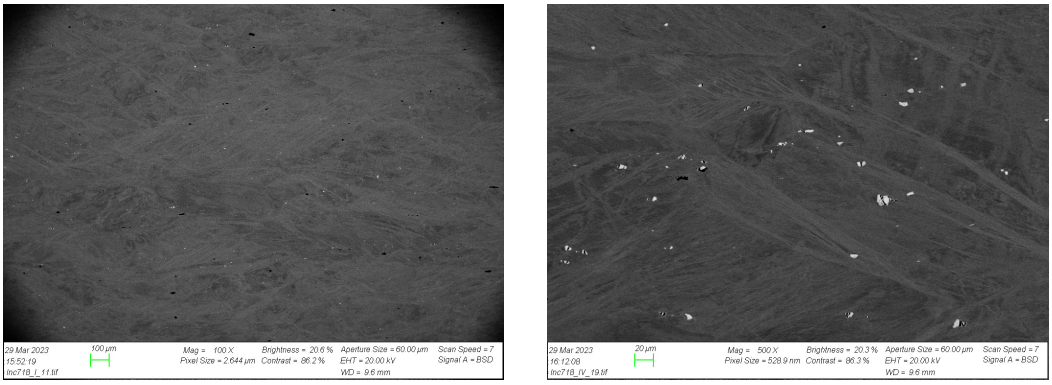

(a) (b)

Figure 4.17: SEM images of sample 50D. (a) 100X magnification with 9.6mm working distance, (b) 500X magnification with 9.6mm working distance..

Sample 50D depicted in Figure 4.17(a-b) also shows a highly deformed microstructure with an unclear grain structure. Some grains can be observed being elongated in the rolling direction and some areas suggests that formation of shear bands have occurred.

Figure 4.17(b) show mainly cracked bright particles distributed randomly throughout the sample due to deformation induced by cold rolling.

Figure 4.18 below shows backscatter images of sample 50DPH with different magnifications.

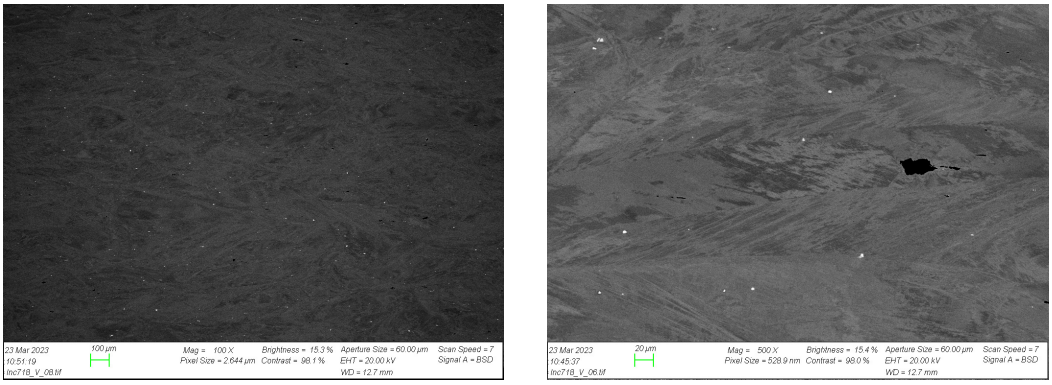

(a) (b)

Figure 4.18: SEM images of sample 50DPH. (a) 100X magnification with 12.7mm working distance, (b) 500X magnification with 12.7mm working distance.

Similarly to sample 50D Figure 4.18(a-b) shows an unclear grain structure, although the grains appear to be elongated in the rolling direction. Also here the microstructure suggest that shear bands have formed. Similarly to all the deformed samples, dark and bright particles appear randomly scattered throughout the entirety of the examined surface.

4.4.1 EDS

In this chapter Energy-dispersive X-ray Spectroscopy results will be presented. This method uses characteristic x-rays to determine chemical composition in a chosen area. The surfaces investigated corresponds to the surface presented in Figure 4.9. Areas examined consisted of interesting features found in the microstructure, such as precipitate particles, as well as the general matrix.

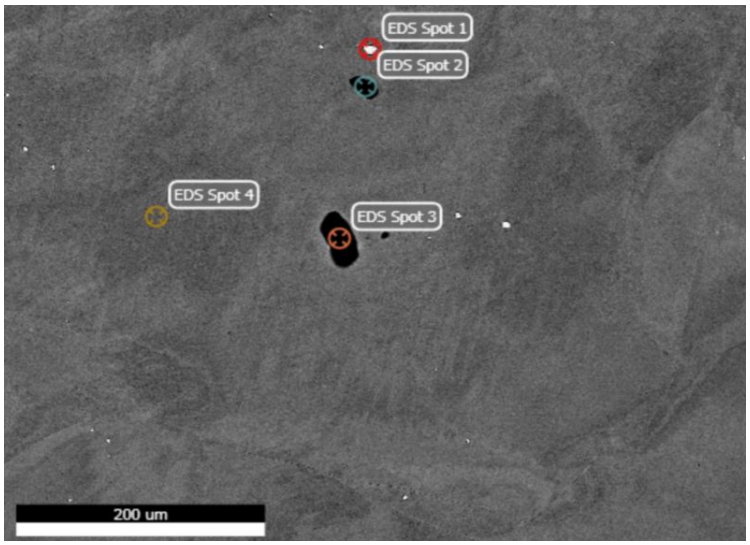

Figure 4.19: EDS spots analyzed in sample 20DPH.

Figure 4.19 shows the surface of sample 20DPH and the different spots chosen for chemical analysis. All other samples were investigated in the same manner and achieved more or less the same results as the sample presented here.

The bright particles (spot 1) found in the microstructure of sample 20DPH, as well as all other samples were found to contain a high amount of Niobium. Heavier elements reflects more signals back to the EDS detector than lighter elements. The dark spots (spot 2 and 3) found in 20DPH and all other samples were found to be rich in Titanium. Spot 4 were analyzed to be the general matrix elements of the material.

The tables below (4.8 - 4.10) presents element, weight percentage, atomic percentage and the error percentage of EDS spot 1, 2 and 4. EDS spot 3 will not be presented as it showed clear faulty results.

Table 4.8: EDS Spot 1 (bright spot).

Element	wt%	at%	Error%
Nb	93.70	88.47	1.29
Ti	6.30	11.53	7.70

Table 4.9: EDS Spot 2 (dark spot)

Element	wt%	at%	Error%
N	24.24	54.86	8.85
Nb	15.55	5.30	1.73
Ti	60.21	39.84	1.81

Table 4.10: EDS Spot 4 (matrix)

Element	wt%	at%	Error%
Nb	2.50	1.55	6.11
Mo	0.82	0.50	16.59
Ti	0.72	0.87	7.70
Cr	17.50	19.44	2.24
Fe	8.65	8.95	4.75
Ni	69.81	68.69	2.10

Comparing Table 4.10 to the known chemical composition of the material presented in chapter 2.2.1, it can be seen that the chemical analysis is not entirely accurate. This is most likely due to analyzing too small of an area. Some amounts of elements are overestimated while other are underestimated, although it still provides an

approximate result.

4.4.2 Fracture Surface

In this chapter, SEM images of the fractured surfaces of the tensile specimens will be presented. This can reveal what type of fracture that occurred and if the samples appear brittle or ductile. The imaging was done by using the secondary electrons which achieves a superior depth of field compared to using backscattered electrons. Aperture size was set to 30 μm with an Accelerating Voltage of 15kV.

As the tensile tests were done on the precipitation hardened samples, only three material states were inspected. Namely sample 0DPH, 20DPH and 50DPH.

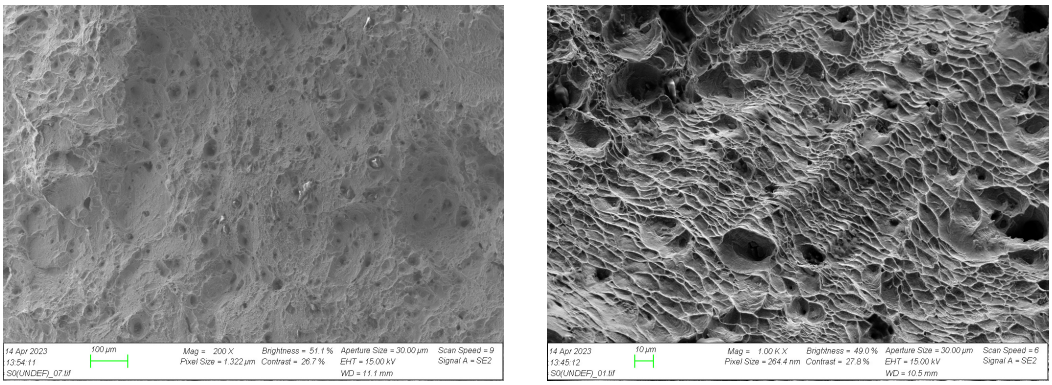

(a) (b)

Figure 4.20: Secondary electron images of the fractured surface of sample 0DPH. (a) 200X magnification with 11.1mm working distance, (b) 1000X magnification with 10.5mm working distance.

Figure 4.20(a-b) above shows secondary electron images of the fractured surface of sample 0DPH with varying degree of magnification. The surface exhibits a

dimpled structure, with deep voids which is a feature of a transgranular ductile fracture mode.

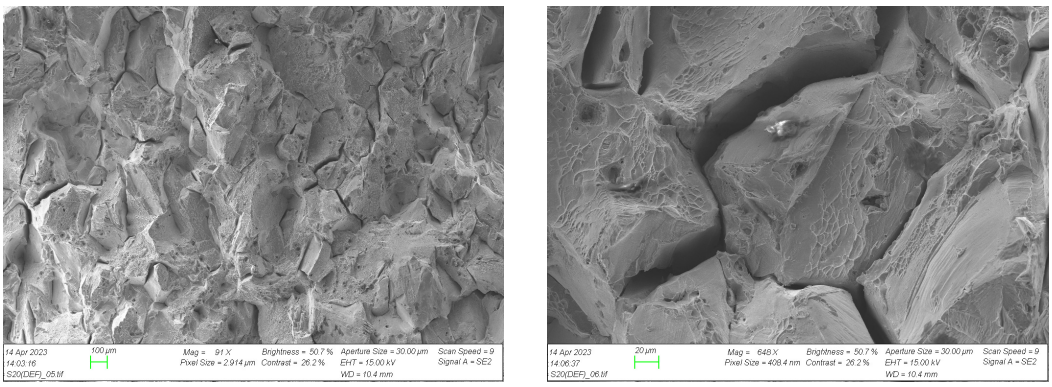

(a) (b)

Figure 4.21: Secondary electron images of the fractured surface of sample 20DPH. (a) 91X magnification with 10.4mm working distance, (b) 648X magnification with 10.4mm working distance.

Figure 4.21 shows SEM images of the fractured surface of sample 20DPH. Long, wide intergranular cracks can be seen in both (a) and (b). This fractured surface is more indicative of a brittle fracture than that of sample 0DPH, which is backed up by the elongation the sample experienced during the tensile test.

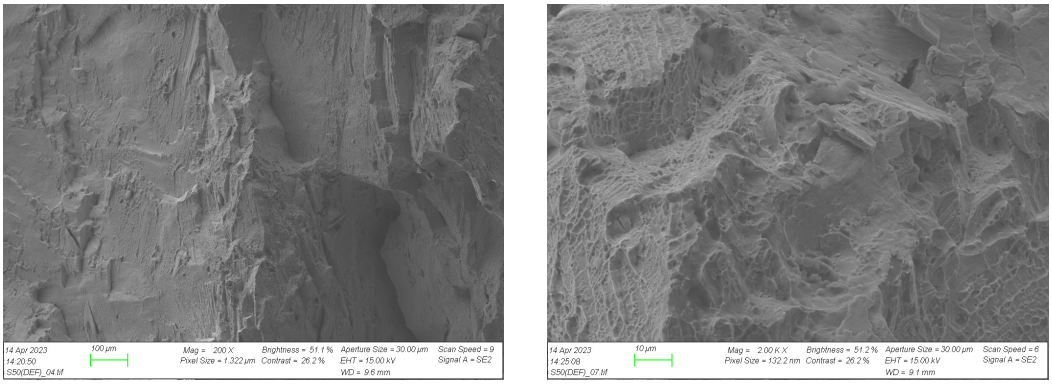

(a) (b)

Figure 4.22: Secondary electron images of the fractured surface of sample 50DPH. (a) 200X magnification with 9.6mm working distance, (b) 2000X magnification with 9.1mm working distance.

Figure 4.22 Shows SEM images of the fractured surface of sample 50DPH. A deep valley located more or less in the center of the sample can be seen in 4.22(a), and transgranular cracks are also visible. Backed up by the tensile test results, this would classify as a brittle fracture.

4.5 EBSD

In this chapter the EBSD results will be presented. All six material states were examined, although the deformed samples proved difficult to achieve high quality images. All samples are examined in the RD-ND plane.

4.5.1 Crystallographic Orientation

Preferred crystallographic directions will be presented in the form of OM (Orientation Maps).

Figure 4.23 below shows the inverse pole figure and direction of the samples that applies to all figures in this chapter.

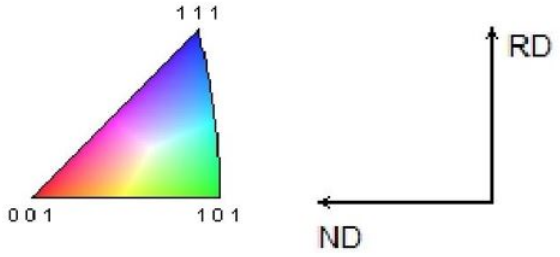

Figure 4.23: Inverse pole figure and directions of sample surface. Applies to all OM.

Table 4.11 specifies the size of the scanned areas and other information about the scanning procedure. The Average Confidence Index says something about the quality of the indexing and is abbreviated CI.

Table 4.11: EBSD scanning information specifying size of area and step size used

Sample	CI	Length X [μm]	Length [μm] Y	Step Size [μm]
0D	0.63	2498	2198	2
0DPH	0.74	2598	2198	2
20D	0.78	2498	2198	2
20DPH	0.49	2498	2198	2
50D	0.50	2498	2198	2
50DPH	0.35	2498	2198	2

Figure 4.24 shows orientation maps of samples 0D on the left and 0DPH on the right.

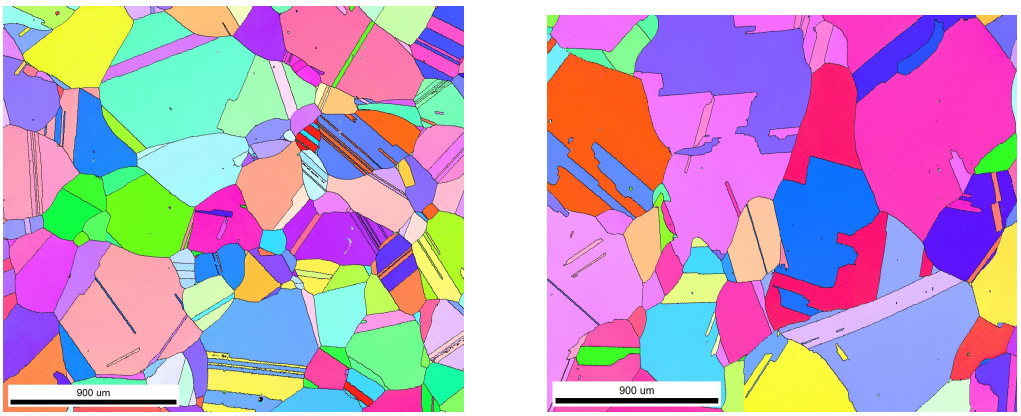

(a) (b)

Figure 4.24: Orientation maps for sample (a) 0D, and (b) 0DPH. The micron bars shows a length of $900\mu m$.

The images in Figure 4.24 shows a microstructure with more or less equiaxed well defined grains with straight grain boundaries. The structure also show a high number of twins. Sample 0DPH which have been precipitation hardened seems to have a larger average grain size than sample 0D which have not been precipitation hardened, although it can not be said with certainty as the scanned area is not very large.

The crystallographic orientation in sample 0D appears to be quite varied between the $\langle 111 \rangle$ $\langle 001 \rangle$ and $\langle 101 \rangle$ directions, while sample 0DPH seems more uniform between the $\langle 111 \rangle$ and $\langle 001 \rangle$ direction with fewer occurrences of the $\langle 101 \rangle$ direction.

Figure 4.25 shows orientation maps of samples 20D on the left and 20DPH on the right. The horizontal lines in (a) is due to something uncontrolled that happened during the scan and should not be taken into consideration when discussing the microstructure.

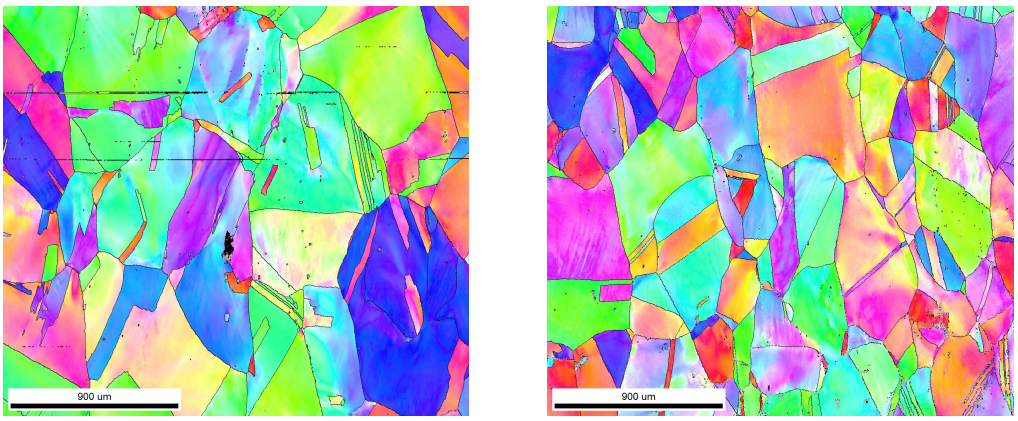

(a) (b)

Figure 4.25: Orientation maps for sample (a) 20D, and (b) 20DPH. The micron bars shows a length of $900\mu m$.

The images in Figure 4.25 also show a well defined grain structure with clearly defined grain boundaries. The grain boundaries are not as straight as in the undeformed samples and a slightly elongated grain structure can be seen. A number of twins can be seen both in sample 20D and 20DPH. The grain size seems to be smaller in sample 20DPH compared to sample 20D, although a definite conclusion can not be made in such a small scanning area.

The crystallographic orientation in both the 20D and 20DPH sample seem to vary between the $\langle 111 \rangle$ $\langle 001 \rangle$ and $\langle 101 \rangle$ directions, although they both have a larger occurrence of the $\langle 101 \rangle$ direction compared to the undeformed samples. The images

also show difference in colour intergranularly which indicate small differences in orientation inside the grains.

Figure 4.26 shows orientation maps of samples 50D on the left and 50DPH on the right.

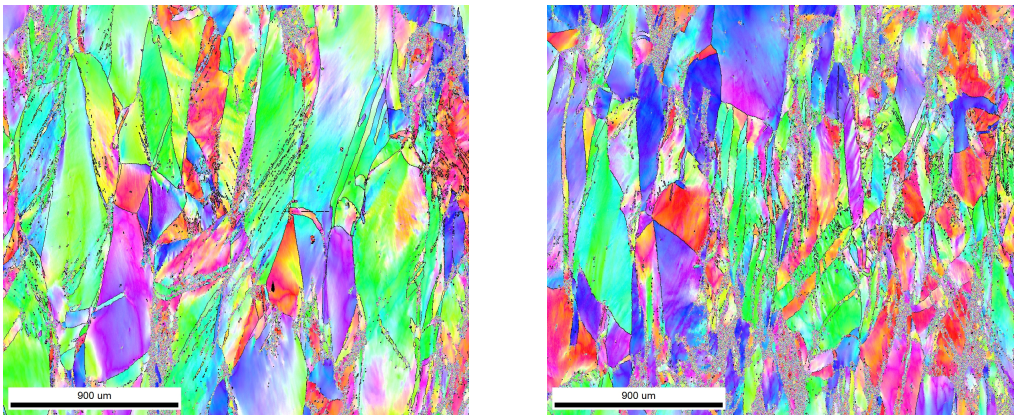

(a) (b)

Figure 4.26: Orientation map for sample (a) 50D, and (b) 50DPH. The micron bars shows a length of $900\mu m$.

Although the quality of the scans are not the best the images in Figure 4.26 both clearly show a highly deformed microstructure which is elongated in the rolling direction. Although some twinning can still be seen, it is not seen to that extent as of the undeformed samples.

The crystallographic orientation varies between $\langle 111 \rangle$ $\langle 001 \rangle$ and $\langle 101 \rangle$ directions, although sample 50D seem to favor the $\langle 101 \rangle$ direction more compared to sample 50DPH. The images also show small differences in orientation intergranularly, as the separate grains are not uniform in colour.

4.5.2 Texture

Texture in a material refers to a preferred orientation of grains in a material. No preferred orientation could be seen by studying the pole figures generated by EBSD in the undeformed and 20% deformed samples, and will not be presented in this chapter. The pole figures for these samples can be found in Appendix F

The 50% deformed sample showed signs of forming a texture, as it can be seen in Figure 4.27.

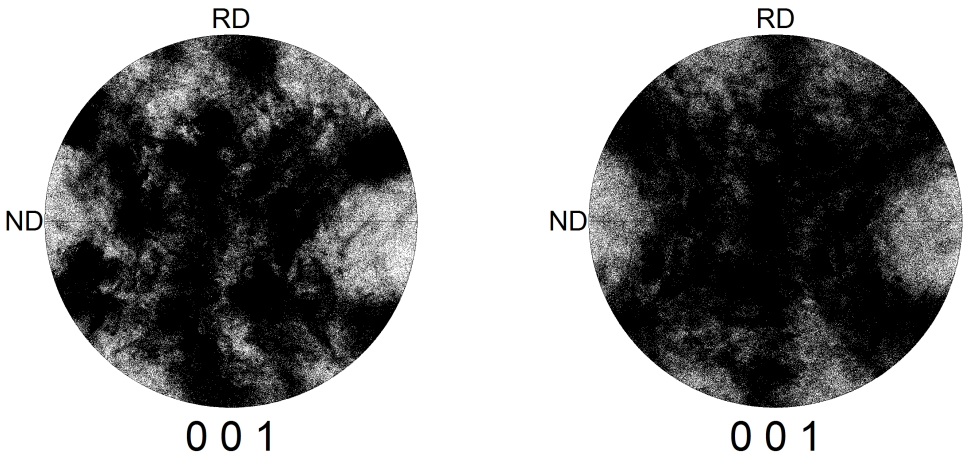

Figure 4.27: Polefigures for 50% deformed samples. (a) shows sample 50D, (b) shows sample 50DPH.

5 Discussion

5.1 Cold Rolling and Hardness Testing

In this thesis, a constant cold rolling reduction of approximately 0.2mm was applied for each pass. Concerned that this constant thickness reduction would lead to uneven deformation throughout the material, investigating the hardness at different specific height locations had to be done.

This resulted in a compromise that had to be done. ISO standard 6507-1:2018 [29] recommended a preferred test force of HV30 for hard materials. However, in this thesis, it was not feasible to use HV30 as the resulting hardness imprints under those loads were large, and the test specimens were small in size. To ensure a sufficient amount of imprints in each sample, the test force was reduced to HV5. This adjustment resulted in an adequate amount of hardness imprints at each height.

Studying the results, it was seen that a relatively uniform hardness across the entirety of each sample was obtained, somewhat disproving the concern of uneven deformation.

The standard deviations obtained for the different hardness results varied in value for each sample. Although the values may appear high, it only differs with a few percent with the average value with the variation ranging from 2.6% to 5.1% in hardness for the most extreme cases.

5.2 Tensile Testing

Due to limited stock of material, only seven tensile test specimens could be produced in total. Each material state required a minimum of three test specimens for validity, so only the precipitation hardened specimens could be tested. Although only one sample in the undeformed state was tested, questioning it's validity, it showed a distinct difference in mechanical properties compared to the deformed samples.

As anticipated, deformation in the form of cold rolling resulted in increased values for both yield strength and ultimate tensile strength. However, it significantly reduced he ductility as shown by the decreased elongation before break.

When comparing the tensile test results, it is clear that both yield and ultimate tensile strength increases with higher levels of deformation. However, the increase in yield strength is more significant than the increase in ultimate tensile strength, while the modulus of elasticity remains nearly unchanged.

For instance, the 20% deformed sample exhibited a 25.2% increase in yield strength while only increasing the ultimate tensile strength with 19.1% when comparing to the undeformed state. A similar result is found when comparing the 20% and the 50% deformed samples, albeit with a slightly smaller difference.

The ductility of the material experienced a substantial reduction with increased cold rolling reduction. By 20% deformation the resulting elongation decreased

to almost half the elongation experienced in the undeformed case decreasing from 21.12 % to 10.62%. Further deformation to 50% reduction decreased the elongation down to 3.81%.

The stress/strain curves also appeared relatively flat which indicates little work hardening occurred during testing and little necking before break.

The decrease of ductility while increased yield and tensile strength can be explained by two main reasons as Zhang et al. showed in [37]. The increase of γ' and γ'' as strengthening precipitates in the matrix causing the strength to increase and the elongation to drop, and an increase of acicular δ precipitates causing lowered ductility. This seems plausible as it is believed that increased degree of deformation increases the volume fraction of δ precipitates in the matrix.

5.3 Cold Rolling and Precipitate Formation

To examine the precipitate phases and their arrangement that formes during the precipitation hardening treatment transmission electron microscope (TEM) examinations are required. Although TEM investigations were not conducted in this thesis, and the formation of precipitates was not observed, it is evident from the results of the mechanical testing that strengthening precipitate phases formed during the heat treatment.

Studying the results of the hardness testing, particularly in the undeformed state (0D and 0DPH), a significant increase in hardness of 160% was observed. As the only difference in treatment between these two samples was the precipitation hardening treatment, it is clear that the main strengthening phase γ'' had formed along with other phases such as δ. The extent to which precipitate phases had formed in terms of volume fraction is unknown.

The percentage increase in hardness between the non precipitation hardened and precipitation hardened samples was not as large for the deformed samples as for the undeformed samples. The samples with 20% reduction achieved a 62.2% increase in hardness, while the samples with 50% reduction only achieved a 26.6% increase.

This then suggest that precipitation hardening has a smaller influence on the strength of the material as cold rolling reduction increases, and that deformation alters the nature of precipitation formation.

As finely dispersed γ'' precipitates is the main strengthening factor of Inconel 718, the δ phase is considered to mainly contribute to impact toughness and creep resistance at elevated temperatures. It is thusly wise to control the volume fraction of δ phase present in the material as δ precipitates at the expense of γ''. The precipitation of δ normally occurs at temperatures between 750-1020 degrees. Below 900 degrees which is the case for this thesis γ'' precedes the precipitation of δ. In that case δ can nucleate at stacking-faults within the already existent γ'' phase and grow into the matrix reaching full transformation from $\gamma'' \rightarrow \delta$ after prolonged aging times. Above 900 degrees precipitation of δ phase can occur directly.

With that being said, Ding et al. in [12] showed that γ'' and δ precipitation kinetics was influenced by plastic deformation and that high-density δ precipitates formed when annealing at only 700 degrees for 5 hours. This can then lower the service temperature of Inconel 718 as delta can directly nucleate and form at lower temperatures when it has been deformed. This temperature- and time-range is similar to that of this thesis and support the claims that increased deformation promotes δ precipitation, ultimately altering the effect of precipitation hardening with increased cold rolling reduction.

Singh et al. [14] showed that δ precipitation is affected by cold rolling reduction where δ can nucleate at slip bands formed during cold rolling decreasing the amount of γ'' phase due to insufficient Nb present. It was also showed that δ precipitation was more prevalent in the higher deformation states than the lower. Rongbin et al. [15] also proved a similar theory and also found that cold rolling changes the morphology of the δ precipitates.

This further explains the trend of decreased effectiveness of precipitation hardening with increased cold rolling reduction as can be seen in the hardness results presented in this thesis.

5.4 Hardness

As expected the hardness increased with increasing degree of deformation and by precipitation, which is mainly due to hindrance of dislocation motion.

As it can be seen by studying the hardness results, the precipitation hardening heat treatment is less effective as degree of deformation increases. This could be explained by the reasons discussed in 5.3, but also due to recovery.

While no evidence of recrystallization was observed, it is likely that recovery, which is a process that can occur with no visible changes in microstructure had taken place [38]. Recovery is influenced by the accumulated internal energy induced by deformation, and higher degrees of deformation contain more internal energy than lower. Thus, it is plausible that recovery occurs more rapidly and easily in highly deformed states. This could also explain the reduced effect of precipitation hardening heat treatment, with respect to hardness, on materials with a high degree of deformation, as recovery restores the physical properties of the cold rolled material.

Another observation that is interesting is that when comparing the undeformed precipitation hardened sample (0DPH) with the 50% deformed non precipitation hardened sample (50D), the hardness only differed with 13HV. This means that although possessing a vastly different microstructure, the hardness achieved was almost the same.

5.5 SEM

Dealing with deformed samples in the electron microscope proved very difficult. Many hours and sessions was spent in the lab trying to obtain usable images.

The EBSD analysis was especially difficult as the highly deformed samples made it difficult to create clear Kikuchi patterns for the software to index. The software used also did not work properly as the post-processing software crashed several times during indexing.

The blasting of an underground tunnel below the lab, which shaked the ground might also have disturbed the scans. In one of the EBSD maps straight horizontal lines can be seen which is believed to be due to a shift of the sample after a blast.

5.6 Texture

The precipitation hardened 50% deformed sample showed signs of forming a material texture, meaning a preferred grain orientation which may have an effect on the material properties of the material. As the dark areas of the polefigures represents a higher volume of a specific orientation, it can be seen that a pattern has formed. The pattern indicates that the grains have aligned well in the rolling direction, while also indicating a higher volume of grains have aligned in the transverse direction and the direction at an angle between the rolling and normal direction.

The undeformed and 20% deformed samples showed a random grain orientation. Although no texture can be observed, the polefigures, along with the OM figures, suggest formation of subgrains in the structure. This is indicated by darker areas of the polefigures, meaning a higher amount of grains with that specific direction is present, and also by the intergranular variety in colour in the OM figures. This is likely caused by the deformation, although it can also have occurred by the precipitation hardening heat treatment.

During deformation the unit cells will rotate to a preferred orientation. This likely will orient the unit cells such that the least dense atomic direction will align with the rolling direction. In the case for fcc structures it is the [111] direction.

It is difficult to assess the effects of texture in this thesis as no clear texture was observed. It may have become more clear had the scanned areas been larger. The material was also not inspected and tested in the transverse orientation which might have yielded different results.

5.7 Potential Errors and Limitations

In an experimental thesis like this it is essential to acknowledge potential errors that may have occurred, which can affect the accuracy and validity of the results.

One of the primary sources of error in experimental studies is measuring errors. Most measurements taken in this thesis has been done manually with a digital

caliper. Although the internal error of the caliper is negligible, human error when taking and reading measurements is still applicable and can affect the accuracy of the results.

As the cold rolling mill was old and had a great deal of play in the mechanisms, it was very difficult to precisely deform the material with a constant step size and achieve an exact final degree of deformation.

The hardness imprints was done with an automatic hardness tester, although for some of the imprints it was necessary to manually adjust the diagonal measurements. How accurately the automatic tester have measured the imprints can affect the results.

Other errors may include excessive heating during machining, inaccurate thermostat in the furnace, placement in the furnace and crooked fastening of the tensile test specimens in the tensile test machine amongst others.

SEM images and scans might also show an incomplete image of the microstructure as only small areas have been focused during imaging and scanning.

6 Conclusion

Shown by results from Vickers hardness testing and tensile testing it can be seen that the formation of strengthening secondary precipitate phases in conventionally produced nickel-based superalloy Inconel 718 is affected by varying degree of cold rolling reduction.

Due to limitations of material stock the tensile tests only allowed to show variations in the precipitation hardened material states which showed an increase in yield and tensile strength, while the ductility was reduced. This only allowed to show the difference in tensile properties for a material which is both cold rolled and precipitation hardened.

Vickers hardness tests showed that hardness increased with increasing degree of cold rolling reduction. The hardness was further increased by precipitates formed during precipitation hardening, although to a decreasing extent as degree of deformation rose.

This suggest that the kinetics of precipitate formation and volume fractions of main strengthening phases γ' and metastable γ'' is altered by the effect of increased deformation which may be due to facilitating precipitation of the stable δ phase which does not directly contribute to strength increase. This was not confirmed as no TEM investigation which allows for observation of precipitate phases was conducted.

6.1 Further Work

Further research is recommended to include TEM investigations focused on examining the influence of cold rolling of precipitate formation and precipitate structure.

It is also advised to conduct further tensile testing on samples that have not undergone precipitation hardening. This will allow for analysing the impact of precipitates on yield strength, tensile strength and elongation, and enable a comparison with the hardness results obtained in this thesis, with particular focus on the diminishing strength enhancement observed as deformation increases.

Additionally, more comprehensive EBSD investigations should be conducted by expanding the scanned areas or increasing the number of areas to gather enough data for a complete texture analysis. Further, it is recommended to test for tensile properties in both the transverse and the longitudinal direction of the preferred grain orientation.

References

[1] C.T. Sims. "A History of Superalloy Metallurgy for Superalloy Metallurgists". en. In: *Superalloys 1984 (Fifth International Symposium)*. TMS, 1984, pp. 399–419. DOI: 10.7449/1984/Superalloys_1984_399_419. URL: http://www.tms.org/Superalloys/10.7449/1984/Superalloys_1984_399_419.pdf (visited on 06/02/2023).

[2] Roger C. Reed. *The Superalloys: Fundamentals and Applications*. Cambridge: Cambridge University Press, 2006. ISBN: 978-0-521-07011-9. DOI: 10.1017/CBO9780511541285. URL: https://www.cambridge.org/core/books/superalloys/00CEE7E1026FA82BBC9F335E75D57AB2 (visited on 04/20/2023).

[3] Matthew J Donachie. *Superalloys : a technical guide*. eng. Edition: 2nd ed. ISBN: 1-61503-064-6 Place: Materials Park, OH. 2002.

[4] Wen-jie Zheng et al. "Effects of carbon content on mechanical properties of inconel 718 alloy". In: *Journal of Iron and Steel Research International* 22.1 (Jan. 2015), pp. 78–83. ISSN: 2210-3988. DOI: 10.1016/S1006-706X(15)60013-9. URL: https://doi.org/10.1016/S1006-706X(15)60013-9.

[5] A. K. Jena and M. C. Chaturvedi. "The role of alloying elements in the design of nickel-base superalloys". en. In: *Journal of Materials Science* 19.10 (Oct. 1984), pp. 3121–3139. ISSN: 0022-2461, 1573-4803. DOI: 10.1007/BF00549796. URL: http://link.springer.com/10.1007/BF00549796 (visited on 04/20/2023).

[6] J A Horton et al. “Microstructural Characterization of Superalloy 718 with Boron and Phosphorus Additions”. en. In: ().

[7] C.G McKamey et al. “Creep Properties of Phosphorus+Boron-Modified Alloy 718”. en. In: *Scripta Materialia* 38.3 (Jan. 1998), pp. 485–491. ISSN: 13596462. DOI: 10.1016/S1359-6462(97)00476-4. URL: https://linkinghub.elsevier.com/retrieve/pii/S1359646297004764 (visited on 04/20/2023).

[8] William D Callister. *Materials science and engineering*. eng. Edition: 9th ed., SI Version. ISBN: 9781118319222 Place: Hoboken, N.J. 2015.

[9] John C. Lippold et al. *Welding Metallurgy and Weldability of Nickel-Base Alloys*. Hoboken, UNITED STATES: John Wiley & Sons, Incorporated, 2009. ISBN: 978-0-470-50021-7. URL: http://ebookcentral.proquest.com/lib/uisbib/detail.action?docID=468615 (visited on 06/08/2023).

[10] R. E Smallman. *Metals and materials : science, processes, applications*. eng. ISBN: 075061093X Place: Oxford. 1995.

[11] Arthur C. Reardon. *Metallurgy for the Non-Metallurgist*. Materials Park, UNITED STATES: A S M International, 2011. ISBN: 978-1-61503-845-9. URL: http://ebookcentral.proquest.com/lib/uisbib/detail.action?docID=3002457.

[12] Jie Ding et al. “Characterization of precipitation in gradient Inconel 718 superalloy”. en. In: *Materials Science and Engineering: A* 804 (Feb. 2021), p. 140718. ISSN: 09215093. DOI: 10.1016/j.msea.2020.140718. URL: https://linkinghub.elsevier.com/retrieve/pii/S0921509320317810 (visited on 05/31/2023).

[13] A. Verma et al. “Evolution of Delta Phase Microstructure in Alloy 718”. en. In: *7th International Symposium on Superalloy 718 and Derivatives (2010)*. John Wiley & Sons, Inc., 2010, pp. 737–750. DOI: 10.7449/2010/Superalloys_2010_737_750. URL: http://www.tms.org/Superalloys/10.7449/2010/Superalloys_2010_737_750.pdf (visited on 06/05/2023).

[14] R.P. Singh et al. “Recrystallization Behavior of Cold Rolled Alloy 718”. en. In: *Superalloys 718, 625 and Various Derivatives (1991)*. TMS, 1991, pp. 205–215. ISBN: 978-0-87339-173-3. DOI: 10.7449/1991/Superalloys_1991_205_215. URL: http://www.tms.org/Superalloys/10.7449/1991/Superalloys_1991_205_215.pdf (visited on 05/30/2023).

[15] Li Rongbin et al. “Effects of Cold Rolling on Precipitates in Inconel 718 Alloy”. en. In: *Journal of Materials Engineering and Performance* 11.5 (Oct. 2002), pp. 504–508. ISSN: 00000000, 10599495. DOI: 10.1361/105994902770343737. URL: http://link.springer.com/10.1361/105994902770343737 (visited on 05/30/2023).

[16] G. Waterloo et al. “Effect of predeformation and preaging at room temperature in Al–Zn–Mg–(Cu,Zr) alloys”. en. In: *Materials Science and Engineering: A* 303.1-2 (May 2001), pp. 226–233. ISSN: 09215093. DOI: 10.1016/S0921-5093(00)01883-9. URL: https://linkinghub.elsevier.com/retrieve/pii/S0921509300018839 (visited on 06/05/2023).

[17] Derek Hull. *Introduction to dislocations*. und. Edition: 3rd ed. ISBN: 0080287212 Place: Oxford Series: International series on materials science and technology Volume: 37. 1984.

[18] Wei Yang and W. B. Lee. "Deformation Mechanisms II: Miscellaneous". In: *Mesoplasticity and its Applications*. Berlin, Heidelberg: Springer Berlin Heidelberg, 1993, pp. 155–190. ISBN: 978-3-642-50040-4. DOI: 10.1007/978-3-642-50040-4_5. URL: https://doi.org/10.1007/978-3-642-50040-4_5.

[19] *Engineering Concepts: Formation of Annealing Twins | Industrial Heating*. en. URL: https://www.industrialheating.com/articles/86154-engineering-concepts-formation-of-annealing-twins (visited on 06/06/2023).

[20] R. Alaghmandfard et al. "Dynamic mechanical properties and failure characteristics of electron beam melted Ti-6Al-4V under high strain rate impact loadings". In: *Materials Science and Engineering: A* 793 (2020), p. 139794. ISSN: 0921-5093. DOI: https://doi.org/10.1016/j.msea.2020.139794. URL: https://www.sciencedirect.com/science/article/pii/S0921509320308686.

[21] Bin Tang et al. "The Formation and Evolution of Shear Bands in Plane Strain Compressed Nickel-Base Superalloy". en. In: *Metals* 8.2 (Feb. 2018), p. 141. ISSN: 2075-4701. DOI: 10.3390/met8020141. URL: http://www.mdpi.com/2075-4701/8/2/141 (visited on 05/20/2023).

[22] Anthony Rollett et al. *Recrystallization and Related Annealing Phenomena*. London, UNITED KINGDOM: Elsevier Science & Technology, 2004. ISBN: 978-0-08-054041-2. URL: http://ebookcentral.proquest.com/lib/uisbib/detail.action?docID=299028 (visited on 06/05/2023).

[23] William F. Spurr and William E. Quist. “The Effects of Crystallographic Texture on the Mechanical and Fracture Properties of Ti-3Al-2.5V Hydraulic Tubing”. In: *SAE Transactions* 82 (1973). Publisher: SAE International, pp. 2227–2236. ISSN: 0096736X, 25771531. URL: http://www.jstor.org/stable/44717617 (visited on 06/09/2023).

[24] Wakshum M. Tucho and Vidar Hansen. “Studies of Post-Fabrication Heat Treatment of L-PBF-Inconel 718: Effects of Hold Time on Microstructure, Annealing Twins, and Hardness”. en. In: *Metals* 11.2 (Feb. 2021), p. 266. ISSN: 2075-4701. DOI: 10.3390/met11020266. URL: https://www.mdpi.com/2075-4701/11/2/266 (visited on 04/20/2023).

[25] Haël Mughrabi. *Materials science and technology : A comprehensive treatment : 6 : Plastic deformation and fracture of materials*. eng. ISBN: 3527268197 Place: Weinheim Volume: 6. 1993.

[26] *EngArc - L - Tensile Test*. URL: http://www.engineeringarchives.com/les_mom_tensiletest.html (visited on 04/20/2023).

[27] *Metallic materials Tensile testing Part 1: Method of test at room temperature (ISO 6892-1:2019)*. Mar. 2020. URL: https://www.standard.no/no/Nettbutikk/produktkatalogen/Produktpresentasjon/?ProductID=1122592.

[28] *Stress-Strain Curve | How to Read the Graph?* en-GB. Section: Engineering Materials. June 2020. URL: http://https\%253A\%252F\%252Ffractory.com\%252Fstress-strain-curve\%252F (visited on 04/21/2023).

[29] *Metallic materials Vickers hardness test Part 1: Test method (ISO 6507-1:2018)*. June 2018. URL: https://www.standard.no/no/

Nettbutikk / produktkatalogen / Produktpresentasjon / ?ProductID = 978537.

[30] Brandon. *What is Scanning Electron Microscopy? (How it Works, Applications, and Limitations)*. en-US. URL: https : / / msestudent . com / what - is - scanning - electron - microscopy - how - it - works - applications-and-limitations/ (visited on 05/19/2023).

[31] *Scanning Electron Microscopy (SEM)*. en. URL: https://serc.carleton.edu/research_education/geochemsheets/techniques/SEM.html (visited on 05/19/2023).

[32] Antonis Nanakoudis. *EDX Analysis with SEM: How Does it Work?* en-US. Nov. 2019. URL: https://www.thermofisher.com/blog/materials/edx-analysis-with-sem-how-does-it-work/ (visited on 05/19/2023).

[33] *Energy-dispersive detector (EDS)*. en. URL: https://serc.carleton.edu/research_education/geochemsheets/eds.html (visited on 05/19/2023).

[34] Zhonglin WANG Weilie L.ZHOU. "Chapter 2 Electron Backscatter Diffraction (EBSD) Technique and Materials Characterization Examples (Tim Maitland and Scott Sitzman)". In: *Advanced Scanning Microscopy for Nanotechnology-Techniques and Applications*. Ed. by Zhonglin WANG Weilie L.ZHOU. 2007, pp. 36 –65. ISBN: 978-7-04-019008-3. URL: https://academic.hep.com.cn/fcc/CN/chapter/chapter380876.shtml.

[35] *An Introduction to EBSD*. en. Section: Materials Article. Feb. 2015. URL: https://www.azom.com/article.aspx?ArticleID=11770 (visited on 05/20/2023).

[36] Struers. *Preparation of ferrous metals for Electron Backscatter Diffraction (EBSD) analysis*. Feb. 2019. URL: https://publications.struers.com/brochures/english/application-notes/ebsd/?_ga=2.218389019.307757237.1684580728-1713319673.1674124846&page=1 (visited on 05/20/2023).

[37] Dongyun Zhang et al. "Effect of standard heat treatment on the microstructure and mechanical properties of selective laser melting manufactured Inconel 718 superalloy". en. In: *Materials Science and Engineering: A* 644 (Sept. 2015), pp. 32–40. ISSN: 09215093. DOI: 10.1016/j.msea.2015.06.021. URL: https://linkinghub.elsevier.com/retrieve/pii/S0921509315300745 (visited on 06/06/2023).

[38] George E Dieter. *Mechanical metallurgy*. eng. Edition: SI metric ed. ISBN: 007084187X Place: London Series: McGraw-Hill series in materials science and engineering. 1988.

Appendix A - Material Documentation

Material documentation provided by SFF:

SR No.		DESCRIPTION	Q'ty	Material	Heat No	Lot No	Heat Treatment(°C×Hr)	
							Quenching	Tempering
0006	1	STUD BOLT	4 EA	ASTM A1014-N07718	D83050	PD201907020713-1		

	SR No.			C X 100	Mn X 100	Si X 100	P X 1000	S X 1000	Ni X 10	Cr X 10	Mo X 100	Cu X 100	Al X 100	Ti X 100	Nb X 100	B X 1000
STD	0006	1	1	0 -8	0 -35	0 -35	0 -15	0 -15	500 -550	170 -210	280 -330	0 -30	20 -80	65 -115	475 -550	0 -6
ACT	0006	1	1	1.4	7.0	6.0	8.0	0.5	543.0	178.6	299.0	5.0	51.0	96.0	502.0	2.5

Figure A.1: Chemical composition of material used in thesis.

Appendix B - Cold Rolling Procedure

20def1 (20% average reduction at 4.18mm)					
Measurements	T1	T2 (mid)	T3 (with arrow)	Average	Diff
1	5,30	5,08	5,27	5,22	
					-1,15 %
2	5,23	5,05	5,20	5,16	
					-1,16 %
3	5,13	5,05	5,11	5,10	
					-2,35 %
4	4,99	4,95	4,99	4,98	
					-2,81 %
5	4,85	4,84	4,84	4,84	
					-5,99 %
6	4,52	4,57	4,57	4,55	
					-5,49 %
7	4,30	4,30	4,31	4,30	
					-3,02 %
8	4,18	4,16	4,18	4,17	
	-21,13 %	-18,11 %	-20,68 %	-20,11 %	-3,14 %

Figure B.1: Cold rolling procedure for sample 20def1.

20def2 (20% average reduction at 4.16mm)					
Measurements	T1	T2 (mid)	T3 (with arrow)	Average	Diff
1	5,27	5,05	5,29	5,20	
					-0,19 %
2	5,27	5,05	5,25	5,19	
					-1,35 %
3	5,17	5,02	5,16	5,12	
					-1,95 %
4	5,04	5,00	5,02	5,02	
					-2,19 %
5	4,91	4,88	4,95	4,91	
					-5,09 %
6	4,63	4,66	4,69	4,66	
					-3,00 %
7	4,53	4,52	4,50	4,52	
					-4,20 %
8	4,34	4,33	4,31	4,33	
					-2,08 %
9	4,25	4,20	4,27	4,24	
					-2,12 %
10	4,16	4,14	4,15	4,15	
	-21,06 %	-18,02 %	-21,55 %	-20,19 %	-2,46 %

Figure B.2: Cold rolling procedure for sample 20def2.

20def3 (20% average reduction at 4.62mm)					
Measurements	T1	T2 (mid)	T3 (with arrow)	Average	Diff
1	5,75	5,76	5,80	5,77	
					-0,69 %
2	5,70	5,72	5,77	5,73	
					-1,75 %
3	5,60	5,63	5,66	5,63	
					-3,55 %
4	5,42	5,44	5,43	5,43	
					-3,31 %
5	5,23	5,26	5,26	5,25	
					-3,81 %
6	5,06	5,05	5,04	5,05	
					-4,55 %
7	4,83	4,83	4,80	4,82	
					-1,87 %
8	4,73	4,73	4,74	4,73	
					-1,69 %
9	4,63	4,66	4,66	4,65	
					-0,65 %
10	4,60	4,63	4,64	4,62	
	-20,00 %	-19,62 %	-20,00 %	-19,93 %	-2,43 %

Figure B.3: Cold rolling procedure for sample 20def3.

50def1 (50% average reduction at 2.83mm)					
Measurements	T1	T2 (mid)	T3 (with arrow)	Average	Diff
1	5,60	5,77	5,62	5,66	
					0,00 %
2	5,57	5,76	5,64	5,66	
					-1,77 %
3	5,53	5,60	5,55	5,56	
					-3,06 %
4	5,35	5,41	5,41	5,39	
					-3,53 %
5	5,17	5,20	5,23	5,20	
					-3,46 %
6	5,01	5,03	5,03	5,02	
					-3,39 %
7	4,88	4,86	4,82	4,85	
					-3,09 %
8	4,63	4,75	4,73	4,70	
					-4,04 %
9	4,49	4,52	4,53	4,51	
					-4,21 %
10	4,29	4,34	4,33	4,32	
					-3,94 %
11	4,17	4,17	4,12	4,15	
					-3,61 %
12	3,96	4,02	4,01	4,00	
					-4,75 %
13	3,84	3,82	3,78	3,81	
					-3,41 %
14	3,65	3,69	3,70	3,68	
					-5,71 %
15	3,49	3,46	3,45	3,47	
					-4,32 %
16	3,31	3,32	3,32	3,32	
					-5,42 %
17	3,15	3,15	3,12	3,14	
					-4,46 %
18	2,97	3,02	3,02	3,00	
					-3,67 %
19	2,89	2,90	2,87	2,89	
					-2,77 %
20	2,80	2,81	2,82	2,81	
	-50,00 %	-51,30 %	-49,82 %	-50,35 %	-3,61 %

Figure B.4: Cold rolling procedure for sample 50def1.

50def2 (50% average reduction at 2.62mm)					
Measurements	T1	T2 (mid)	T3 (with arrow)	Average	Diff
1	5,30	4,93	5,50	5,24	
					-2,86 %
2	5,12	4,95	5,20	5,09	
					-1,18 %
3	5,05	4,97	5,08	5,03	
					-2,98 %
4	4,88	4,84	4,92	4,88	
					-2,46 %
5	4,71	4,74	4,83	4,76	
					-4,83 %
6	4,53	4,51	4,55	4,53	
					-3,31 %
7	4,34	4,38	4,43	4,38	
					-4,11 %
8	4,19	4,20	4,22	4,20	
					-4,05 %
9	4,06	4,02	4,02	4,03	
					-4,47 %
10	3,83	3,84	3,88	3,85	
					-4,16 %
11	3,70	3,68	3,69	3,69	
					-3,79 %
12	3,55	3,53	3,56	3,55	
					-3,94 %
13	3,43	3,40	3,40	3,41	
					-4,99 %
14	3,23	3,24	3,26	3,24	
					-4,63 %
15	3,05	3,09	3,12	3,09	
					-6,47 %
16	2,86	2,89	2,93	2,89	
					-5,88 %
17	2,70	2,73	2,74	2,72	
					-2,57 %
18	2,62	2,65	2,68	2,65	
					-2,26 %
19	2,57	2,59	2,61	2,59	
	-51,51 %	-47,46 %	-52,55 %	-50,57 %	-3,83 %

Figure B.5: Cold rolling procedure for sample 50def2.

50def3 (50% average reduction at 2.62mm)					
Measurements	T1	T2 (mid)	T3 (with arrow)	Average	Diff
1	5,47	4,92	5,36	5,25	
					-1,52 %
2	5,36	4,92	5,24	5,17	
					-1,55 %
3	5,20	4,92	5,15	5,09	
					-2,16 %
4	5,02	4,90	5,01	4,98	
					-3,41 %
5	4,85	4,76	4,81	4,81	
					-3,74 %
6	4,64	4,61	4,65	4,63	
					-3,67 %
7	4,50	4,43	4,44	4,46	
					-4,04 %
8	4,32	4,28	4,25	4,28	
					-5,14 %
9	4,06	4,04	4,09	4,06	
					-3,69 %
10	3,95	3,91	3,87	3,91	
					-4,86 %
11	3,73	3,67	3,75	3,72	
					-3,76 %
12	3,59	3,57	3,59	3,58	
					-4,19 %
13	3,45	3,43	3,41	3,43	
					-4,96 %
14	3,27	3,25	3,25	3,26	
					-6,75 %
15	3,07	3,04	3,00	3,04	
					-5,26 %
16	2,88	2,88	2,88	2,88	
					-5,90 %
17	2,68	2,72	2,73	2,71	
					-3,32 %
18	2,57	2,63	2,66	2,62	
					-1,15 %
19	2,57	2,60	2,60	2,59	
	-53,02 %	-47,15 %	-51,49 %	-50,67 %	-3,84 %

Figure B.6: Cold rolling procedure for sample 50def3.

Appendix C - Furnace Cooling Rate

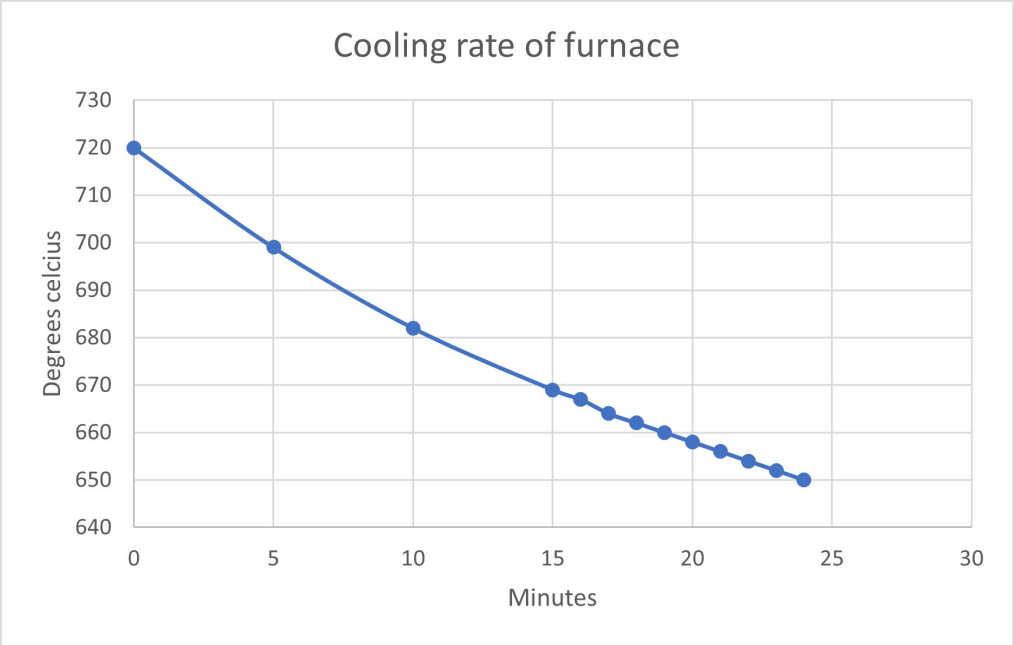

Figure C.1: Cooling rate of furnace during precipitation hardening.

Appendix D - Hardness Results According to Height

Table D.1: Results corresponding to height in sample 0D and 0DPH

Sample name	Height	Nr. of imprints	Avg HV	SD
0D	1	11	166.40	3.23
	2	11	166.51	5.17
	3	11	166.08	6.03
	4	11	168.20	2.27
	5	11	163.93	4.27
	6	11	162.81	4.80
	7	11	164.27	4.10
0DPH	1	10	428.8	7.86
	2	10	427.28	5.32
	3	10	432.14	9.54
	4	10	434.95	10.70
	5	10	436.92	9.12
	6	10	431.24	7.62
	7	10	438.71	13.30
	8	10	428.68	13.25
	9	10	422.07	13.78
	10	10	420.42	8.78

Table D.2: Results corresponding to height 20D and 20DPH

Sample name	Height	Nr. of imprints	Avg HV	SD
20D	1	14	298.56	15.94
	2	14	292.49	14.16
	3	14	285.90	16.47
	4	14	287.85	15.98
	5	14	288.96	14.98
	6	14	290.62	8.20
	7	14	290.10	16.48
20DPH	1	10	467.55	13.06
	2	10	469.60	10.87
	3	10	473.73	9.52
	4	10	471.34	15.36
	5	10	473.86	11.10
	6	10	472.98	12.44
	7	10	476.46	13.51
	8	10	473.53	16.51
	9	10	473.64	12.41
	10	10	468.30	8.19

Table D.3: Results corresponding to height for sample 50D and 50DPH

Sample name	Height	Nr. of imprints	Avg HV	SD
50D	1	16	415.98	12.89
	2	16	415.29	16.28
	3	16	417.41	16.77
	4	16	421.20	16.15
	5	16	412.97	13.48
50DPH	1	17	525.80	14.96
	2	17	530.29	12.36
	3	17	528.26	11.44
	4	17	532.58	13.22
	5	17	524.01	14.41

Appendix E - Tensile Test Graphs

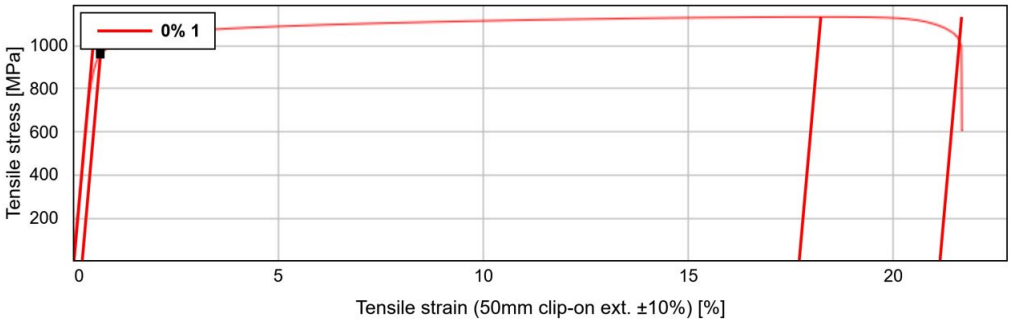

Figure E.1: 0DPH tensile test graph.

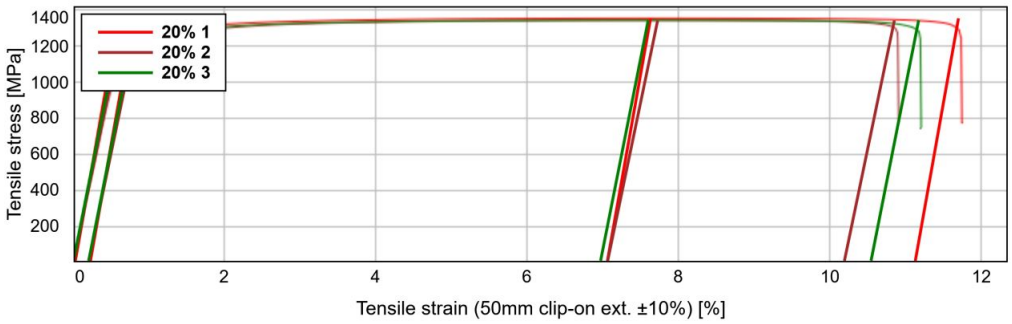

Figure E.2: 20DPH tensile test graphs.

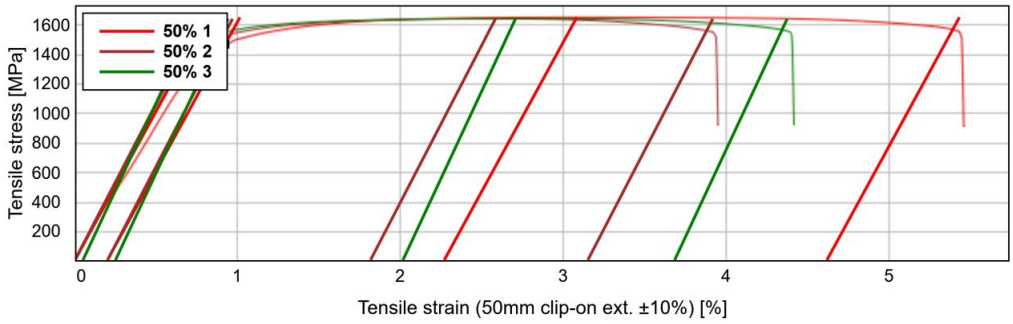

Figure E.3: 50DPH tensile test graphs.

Appendix F - Pole Figures

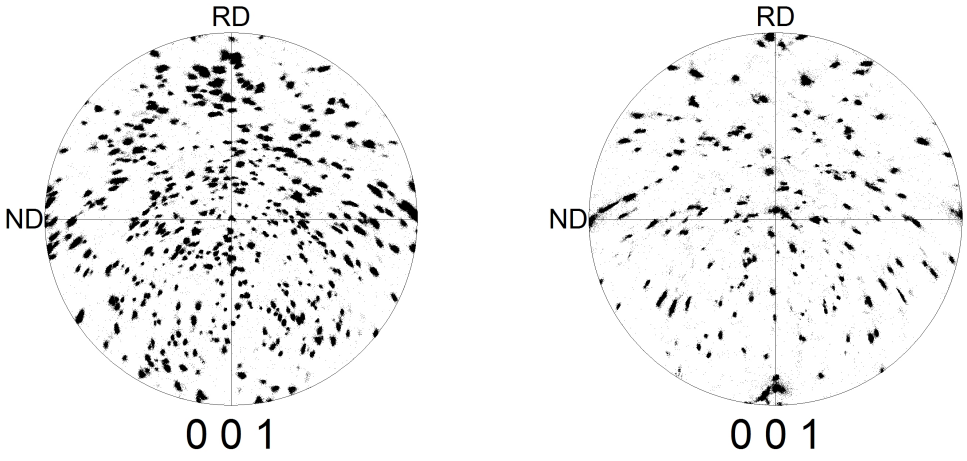

Figure F.1: Polefigures for undeformed samples. (a) Sample 0D, (b) Sample 0DPH.

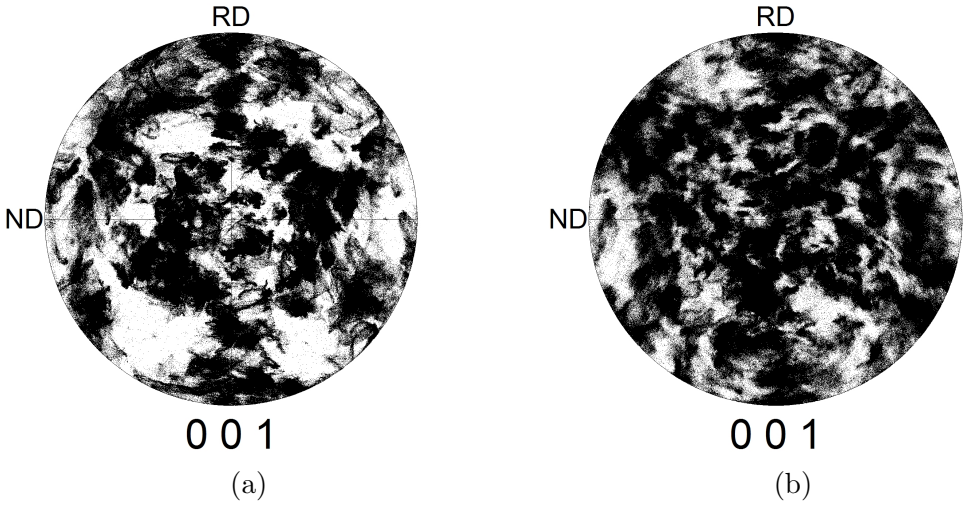

Figure F.2: Polefigures for 20% deformed samples. (a) Sample 20D, (b) 20DPH.

Appendix G - Hardness Data

The following pages contain reports printed from the automatic hardness tester. Listed below is all hardness imprints, their hardness values, and their location. Note that the scales of the colour plots differs for each sample.

Sample: 0D

INNOVATEST®
Advanced Hardness Testing Solutions

Universitetet i Stavanger

www.uis.no

General Information

Date	April 13, 2023
Operator	Johan
Hardness tester type	FALCON 5001

Program Description

Name	I

Enter Comments

Sample: 0D

Hardness Test Information

Method	VICKERS
Hardness scale	HV5
Dwell time	10 sec.

Color Map

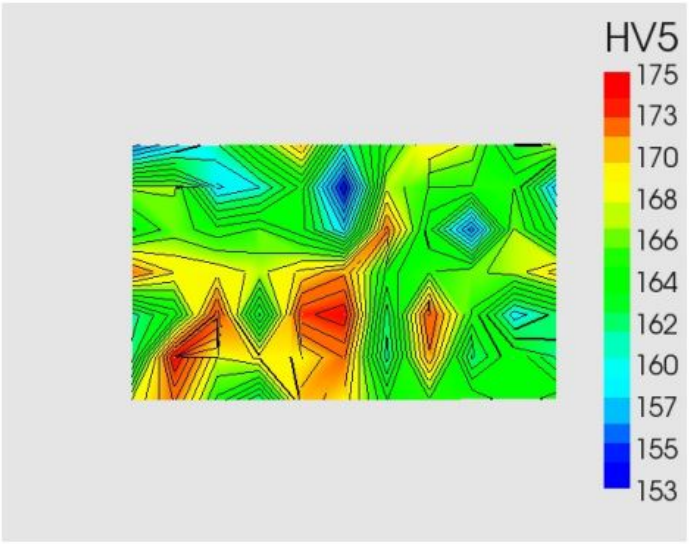

Measurement Tables

Pattern: 1

Measurement Index	Result
1 (1/1)	160 HV5
2 (1/1)	158 HV5
3 (1/1)	161 HV5
4 (1/1)	166 HV5
5 (1/1)	170 HV5
6 (1/1)	160 HV5
7 (1/1)	165 HV5
8 (1/1)	169 HV5
9 (1/1)	167 HV5
10 (1/1)	162 HV5
11 (1/1)	168 HV5
12 (1/1)	167 HV5
13 (1/1)	167 HV5
14 (1/1)	158 HV5
15 (1/1)	160 HV5
16 (1/1)	164 HV5
17 (1/1)	153 HV5
18 (1/1)	168 HV5
19 (1/1)	166 HV5
20 (1/1)	166 HV5
21 (1/1)	166 HV5
22 (1/1)	158 HV5
23 (1/1)	164 HV5
24 (1/1)	166 HV5
25 (1/1)	165 HV5
26 (1/1)	166 HV5
27 (1/1)	164 HV5
28 (1/1)	159 HV5
29 (1/1)	172 HV5
30 (1/1)	164 HV5
31 (1/1)	156 HV5
32 (1/1)	167 HV5
33 (1/1)	162 HV5
34 (1/1)	171 HV5
35 (1/1)	169 HV5
36 (1/1)	169 HV5

37 (1/1)	168 HV5
38 (1/1)	169 HV5
39 (1/1)	171 HV5
40 (1/1)	164 HV5
41 (1/1)	165 HV5
42 (1/1)	167 HV5
43 (1/1)	167 HV5
44 (1/1)	170 HV5
45 (1/1)	160 HV5
46 (1/1)	164 HV5
47 (1/1)	173 HV5
48 (1/1)	162 HV5
49 (1/1)	173 HV5
50 (1/1)	174 HV5
51 (1/1)	161 HV5
52 (1/1)	173 HV5
53 (1/1)	165 HV5
54 (1/1)	159 HV5
55 (1/1)	161 HV5
56 (1/1)	161 HV5
57 (1/1)	175 HV5
58 (1/1)	168 HV5
59 (1/1)	169 HV5
60 (1/1)	169 HV5
61 (1/1)	172 HV5
62 (1/1)	160 HV5
63 (1/1)	171 HV5
64 (1/1)	161 HV5
65 (1/1)	164 HV5
66 (1/1)	161 HV5
67 (1/1)	168 HV5
68 (1/1)	172 HV5
69 (1/1)	165 HV5
70 (1/1)	161 HV5
71 (1/1)	171 HV5
72 (1/1)	170 HV5
73 (1/1)	164 HV5
74 (1/1)	165 HV5
75 (1/1)	165 HV5
76 (1/1)	163 HV5

77 (1/1)	165 HV5
78 (1/1)	168 HV5
79 (1/1)	156 HV5

Statistics

Pattern	Mean	Min	Max	SD	Range	USL	LSL	Cp	Cpk
1	165	153	175	5	22	0.00	0.00	0	-12

Snapshot

Snapshot 1

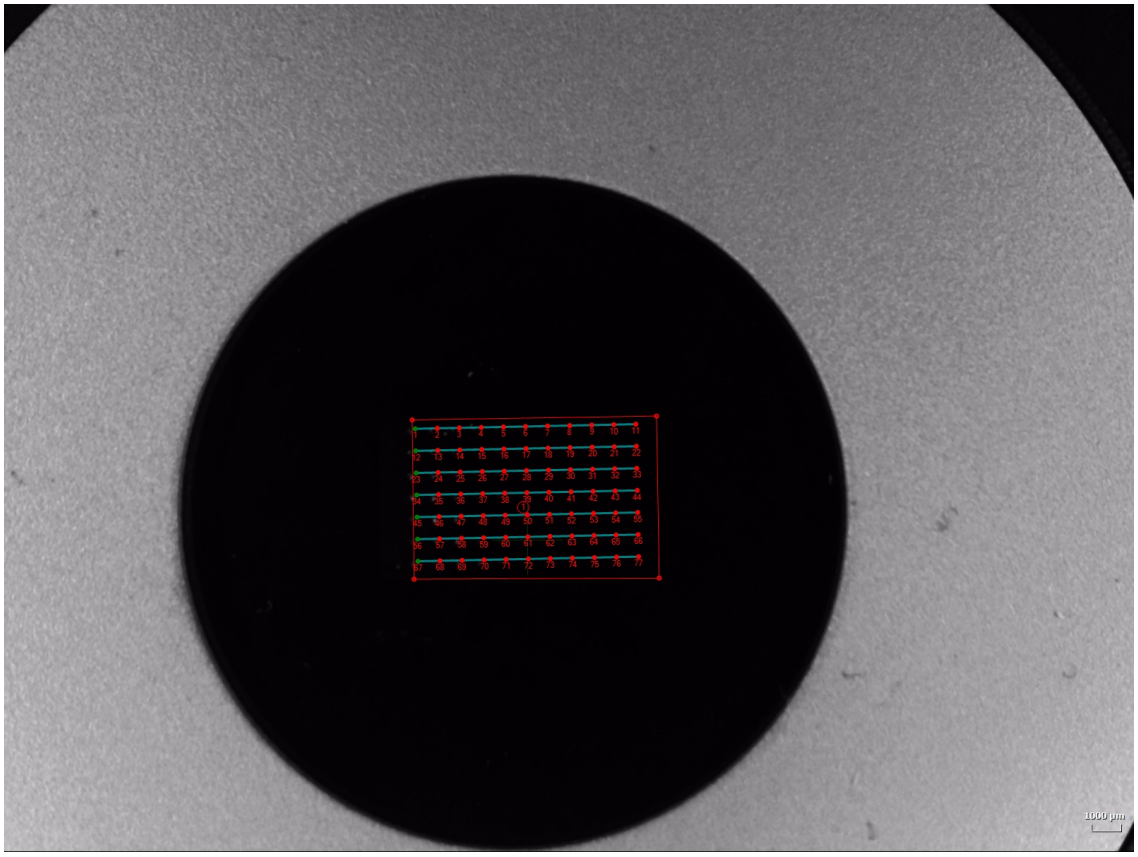

"Enter comments"

Sample: 0DPH

INNOVATEST®
Advanced Hardness Testing Solutions

Universitetet i Stavanger

www.uis.no

General Information

Date	April 13, 2023
Operator	Johan
Hardness tester type	FALCON 5001

Program Description

Name	II

Enter Comments

Sample: 0DPH

Hardness Test Information

Method	VICKERS
Hardness scale	HV5
Dwell time	10 sec.

Color Map

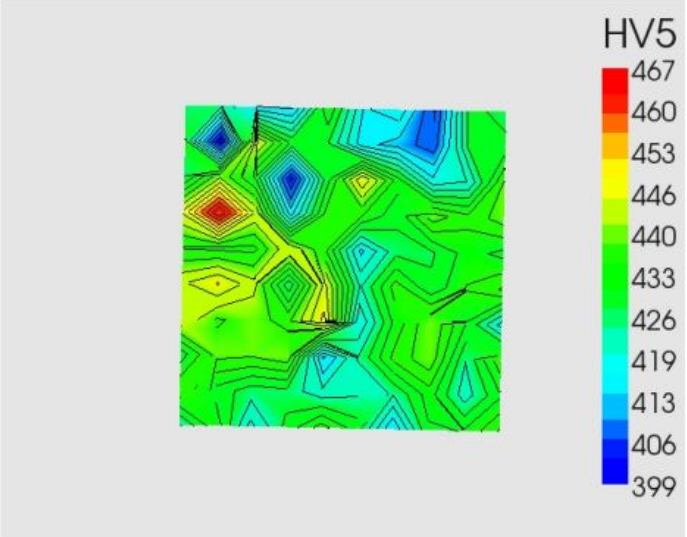

Measurement Tables

Pattern: 1

Measurement Index	Result
1 (1/1)	425 HV5
2 (1/1)	424 HV5
3 (1/1)	413 HV5
4 (1/1)	412 HV5
5 (1/1)	434 HV5
6 (1/1)	416 HV5
7 (1/1)	419 HV5
8 (1/1)	405 HV5
9 (1/1)	429 HV5
10 (1/1)	425 HV5
11 (1/1)	428 HV5
12 (1/1)	399 HV5
13 (1/1)	446 HV5
14 (1/1)	430 HV5
15 (1/1)	428 HV5
16 (1/1)	414 HV5
17 (1/1)	412 HV5
18 (1/1)	407 HV5
19 (1/1)	428 HV5
20 (1/1)	429 HV5
21 (1/1)	427 HV5
22 (1/1)	441 HV5
23 (1/1)	430 HV5
24 (1/1)	402 HV5
25 (1/1)	429 HV5
26 (1/1)	448 HV5
27 (1/1)	433 HV5
28 (1/1)	418 HV5
29 (1/1)	421 HV5
30 (1/1)	439 HV5
31 (1/1)	446 HV5
32 (1/1)	467 HV5
33 (1/1)	445 HV5
34 (1/1)	415 HV5
35 (1/1)	436 HV5
36 (1/1)	435 HV5

37 (1/1)	428 HV5
38 (1/1)	440 HV5
39 (1/1)	436 HV5
40 (1/1)	440 HV5
41 (1/1)	434 HV5
42 (1/1)	433 HV5
43 (1/1)	433 HV5
44 (1/1)	445 HV5
45 (1/1)	435 HV5
46 (1/1)	416 HV5
47 (1/1)	426 HV5
48 (1/1)	427 HV5
49 (1/1)	433 HV5
50 (1/1)	430 HV5
51 (1/1)	445 HV5
52 (1/1)	449 HV5
53 (1/1)	443 HV5
54 (1/1)	425 HV5
55 (1/1)	446 HV5
56 (1/1)	423 HV5
57 (1/1)	436 HV5
58 (1/1)	428 HV5
59 (1/1)	435 HV5
60 (1/1)	439 HV5
61 (1/1)	445 HV5
62 (1/1)	438 HV5
63 (1/1)	439 HV5
64 (1/1)	437 HV5
65 (1/1)	450 HV5
66 (1/1)	417 HV5
67 (1/1)	432 HV5
68 (1/1)	442 HV5
69 (1/1)	431 HV5
70 (1/1)	418 HV5
71 (1/1)	429 HV5
72 (1/1)	439 HV5
73 (1/1)	439 HV5
74 (1/1)	441 HV5
75 (1/1)	412 HV5
76 (1/1)	424 HV5

77 (1/1)	436 HV5
78 (1/1)	441 HV5
79 (1/1)	424 HV5
80 (1/1)	437 HV5
81 (1/1)	438 HV5
82 (1/1)	430 HV5
83 (1/1)	425 HV5
84 (1/1)	426 HV5
85 (1/1)	421 HV5
86 (1/1)	423 HV5
87 (1/1)	424 HV5
88 (1/1)	433 HV5
89 (1/1)	422 HV5
90 (1/1)	431 HV5
91 (1/1)	423 HV5
92 (1/1)	433 HV5
93 (1/1)	419 HV5
94 (1/1)	428 HV5
95 (1/1)	436 HV5
96 (1/1)	429 HV5
97 (1/1)	413 HV5
98 (1/1)	431 HV5
99 (1/1)	431 HV5
100 (1/1)	439 HV5

Statistics

Pattern	Mean	Min	Max	SD	Range	USL	LSL	Cp	Cpk
1	430	399	467	11	68	0.00	0.00	0	-13

Snapshot

Snapshot 1

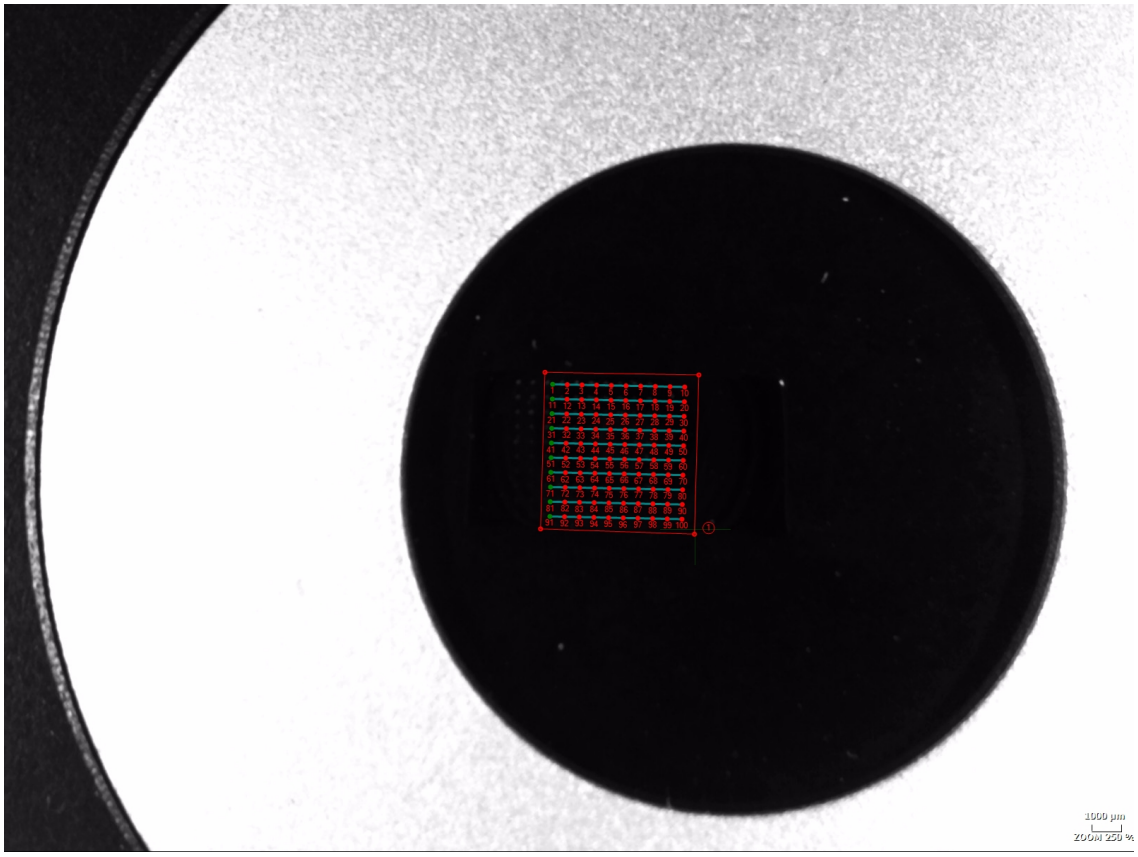

"Enter comments"

Sample: 20D

INNOVATEST®
Advanced Hardness Testing Solutions

Universitetet i Stavanger

www.uis.no

General Information

Date	April 13, 2023
Operator	Johan
Hardness tester type	FALCON 5001

Program Description

Name	VI

Enter Comments

Sample: 20D

Hardness Test Information

Method	VICKERS
Hardness scale	HV5
Dwell time	10 sec.

Color Map

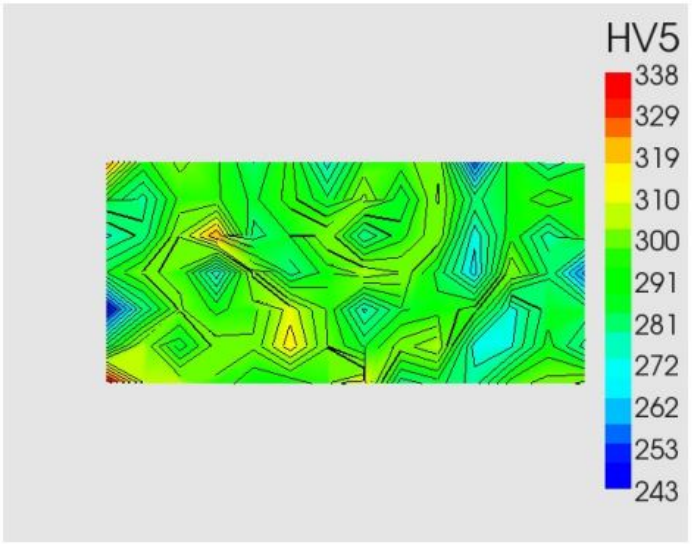

Measurement Tables

Pattern: 1

Measurement Index	Result
1 (1/1)	288 HV5
2 (1/1)	280 HV5
3 (1/1)	293 HV5
4 (1/1)	252 HV5
5 (1/1)	303 HV5
6 (1/1)	295 HV5
7 (1/1)	294 HV5
8 (1/1)	270 HV5
9 (1/1)	295 HV5
10 (1/1)	283 HV5
11 (1/1)	294 HV5
12 (1/1)	300 HV5
13 (1/1)	291 HV5
14 (1/1)	325 HV5
15 (1/1)	291 HV5
16 (1/1)	297 HV5
17 (1/1)	289 HV5
18 (1/1)	281 HV5
19 (1/1)	303 HV5
20 (1/1)	283 HV5
21 (1/1)	305 HV5
22 (1/1)	284 HV5
23 (1/1)	295 HV5
24 (1/1)	287 HV5
25 (1/1)	294 HV5
26 (1/1)	295 HV5
27 (1/1)	276 HV5
28 (1/1)	289 HV5
29 (1/1)	290 HV5
30 (1/1)	275 HV5
31 (1/1)	292 HV5
32 (1/1)	269 HV5
33 (1/1)	302 HV5
34 (1/1)	291 HV5
35 (1/1)	278 HV5
36 (1/1)	303 HV5

37 (1/1)	288 HV5
38 (1/1)	280 HV5
39 (1/1)	322 HV5
40 (1/1)	303 HV5
41 (1/1)	280 HV5
42 (1/1)	272 HV5
43 (1/1)	255 HV5
44 (1/1)	283 HV5
45 (1/1)	303 HV5
46 (1/1)	265 HV5
47 (1/1)	286 HV5
48 (1/1)	303 HV5
49 (1/1)	307 HV5
50 (1/1)	290 HV5
51 (1/1)	280 HV5
52 (1/1)	304 HV5
53 (1/1)	269 HV5
54 (1/1)	297 HV5
55 (1/1)	299 HV5
56 (1/1)	288 HV5
57 (1/1)	287 HV5
58 (1/1)	286 HV5
59 (1/1)	270 HV5
60 (1/1)	295 HV5
61 (1/1)	290 HV5
62 (1/1)	287 HV5
63 (1/1)	271 HV5
64 (1/1)	297 HV5
65 (1/1)	311 HV5
66 (1/1)	296 HV5
67 (1/1)	292 HV5
68 (1/1)	299 HV5
69 (1/1)	278 HV5
70 (1/1)	243 HV5
71 (1/1)	276 HV5
72 (1/1)	290 HV5
73 (1/1)	272 HV5
74 (1/1)	270 HV5
75 (1/1)	308 HV5
76 (1/1)	301 HV5

77 (1/1)	287 HV5
78 (1/1)	298 HV5
79 (1/1)	316 HV5
80 (1/1)	299 HV5
81 (1/1)	300 HV5
82 (1/1)	285 HV5
83 (1/1)	308 HV5
84 (1/1)	284 HV5
85 (1/1)	304 HV5
86 (1/1)	300 HV5
87 (1/1)	296 HV5
88 (1/1)	275 HV5
89 (1/1)	285 HV5
90 (1/1)	280 HV5
91 (1/1)	314 HV5
92 (1/1)	296 HV5
93 (1/1)	289 HV5
94 (1/1)	289 HV5
95 (1/1)	297 HV5
96 (1/1)	307 HV5
97 (1/1)	308 HV5
98 (1/1)	338 HV5

Statistics

Pattern	Mean	Min	Max	SD	Range	USL	LSL	Cp	Cpk
1	291	243	338	15	95	0.00	0.00	0	-7

Snapshot

Snapshot 1

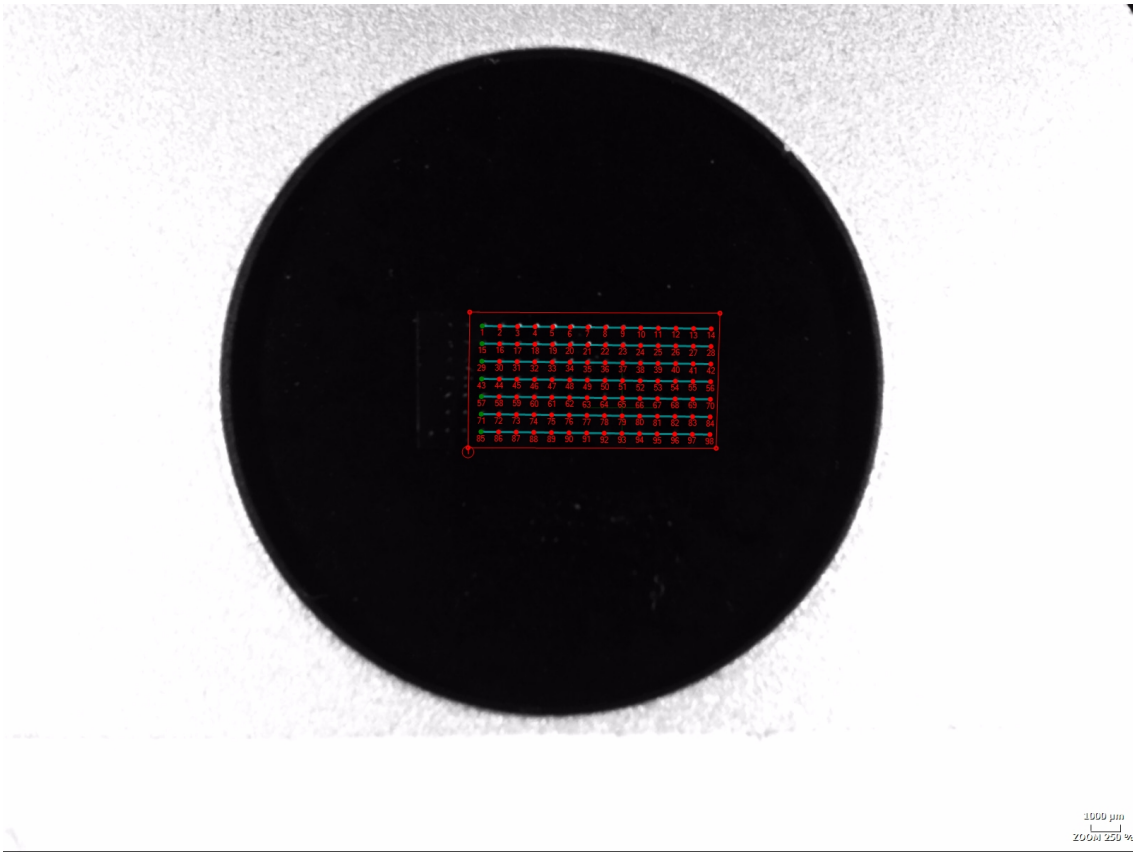

"Enter comments"

Sample: 20DPH

INNOVATEST®
Advanced Hardness Testing Solutions

Universitetet i Stavanger

www.uis.no

General Information

Date	April 13, 2023
Operator	Johan
Hardness tester type	FALCON 5001

Program Description

Name	III

Enter Comments

Sample: 20DPH

Hardness Test Information

Method	VICKERS
Hardness scale	HV5
Dwell time	10 sec.

Color Map

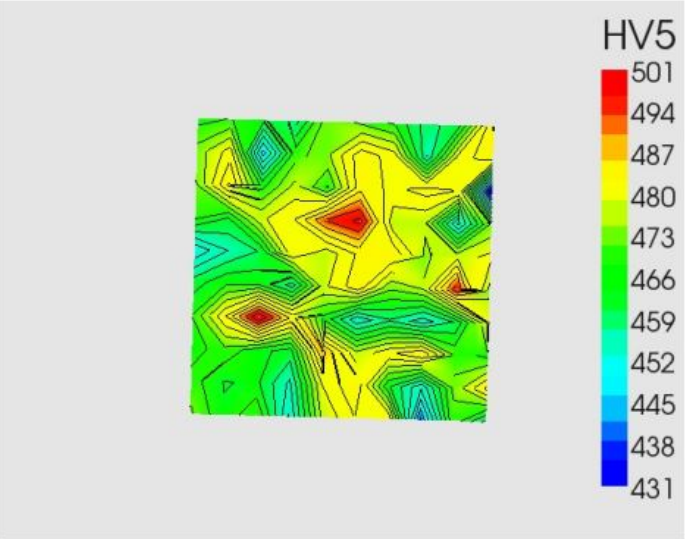

Measurement Tables

Pattern: 1

Measurement Index	Result
1 (1/1)	467 HV5
2 (1/1)	468 HV5
3 (1/1)	465 HV5
4 (1/1)	459 HV5
5 (1/1)	475 HV5
6 (1/1)	471 HV5
7 (1/1)	468 HV5
8 (1/1)	459 HV5
9 (1/1)	464 HV5
10 (1/1)	487 HV5
11 (1/1)	473 HV5
12 (1/1)	481 HV5
13 (1/1)	448 HV5
14 (1/1)	470 HV5
15 (1/1)	475 HV5
16 (1/1)	485 HV5
17 (1/1)	481 HV5
18 (1/1)	457 HV5
19 (1/1)	482 HV5
20 (1/1)	484 HV5
21 (1/1)	472 HV5
22 (1/1)	487 HV5
23 (1/1)	467 HV5
24 (1/1)	477 HV5
25 (1/1)	468 HV5
26 (1/1)	485 HV5
27 (1/1)	482 HV5
28 (1/1)	484 HV5
29 (1/1)	483 HV5
30 (1/1)	431 HV5
31 (1/1)	469 HV5
32 (1/1)	464 HV5
33 (1/1)	478 HV5
34 (1/1)	483 HV5
35 (1/1)	494 HV5
36 (1/1)	499 HV5

37 (1/1)	477 HV5
38 (1/1)	476 HV5
39 (1/1)	452 HV5
40 (1/1)	472 HV5
41 (1/1)	450 HV5
42 (1/1)	457 HV5
43 (1/1)	461 HV5
44 (1/1)	483 HV5
45 (1/1)	477 HV5
46 (1/1)	484 HV5
47 (1/1)	486 HV5
48 (1/1)	475 HV5
49 (1/1)	478 HV5
50 (1/1)	480 HV5
51 (1/1)	463 HV5
52 (1/1)	468 HV5
53 (1/1)	467 HV5
54 (1/1)	459 HV5
55 (1/1)	478 HV5
56 (1/1)	485 HV5
57 (1/1)	472 HV5
58 (1/1)	476 HV5
59 (1/1)	496 HV5
60 (1/1)	474 HV5
61 (1/1)	468 HV5
62 (1/1)	483 HV5
63 (1/1)	501 HV5
64 (1/1)	485 HV5
65 (1/1)	467 HV5
66 (1/1)	454 HV5
67 (1/1)	460 HV5
68 (1/1)	455 HV5
69 (1/1)	461 HV5
70 (1/1)	479 HV5
71 (1/1)	466 HV5
72 (1/1)	471 HV5
73 (1/1)	466 HV5
74 (1/1)	463 HV5
75 (1/1)	491 HV5
76 (1/1)	476 HV5

77 (1/1)	482 HV5
78 (1/1)	486 HV5
79 (1/1)	471 HV5
80 (1/1)	467 HV5
81 (1/1)	470 HV5
82 (1/1)	464 HV5
83 (1/1)	465 HV5
84 (1/1)	456 HV5
85 (1/1)	479 HV5
86 (1/1)	486 HV5
87 (1/1)	465 HV5
88 (1/1)	454 HV5
89 (1/1)	473 HV5
90 (1/1)	484 HV5
91 (1/1)	473 HV5
92 (1/1)	465 HV5
93 (1/1)	472 HV5
94 (1/1)	453 HV5
95 (1/1)	476 HV5
96 (1/1)	483 HV5
97 (1/1)	483 HV5
98 (1/1)	442 HV5
99 (1/1)	471 HV5
100 (1/1)	459 HV5

Statistics

Pattern	Mean	Min	Max	SD	Range	USL	LSL	Cp	Cpk
1	472	431	501	12	70	0.00	0.00	0	-13

Snapshot

Snapshot 1

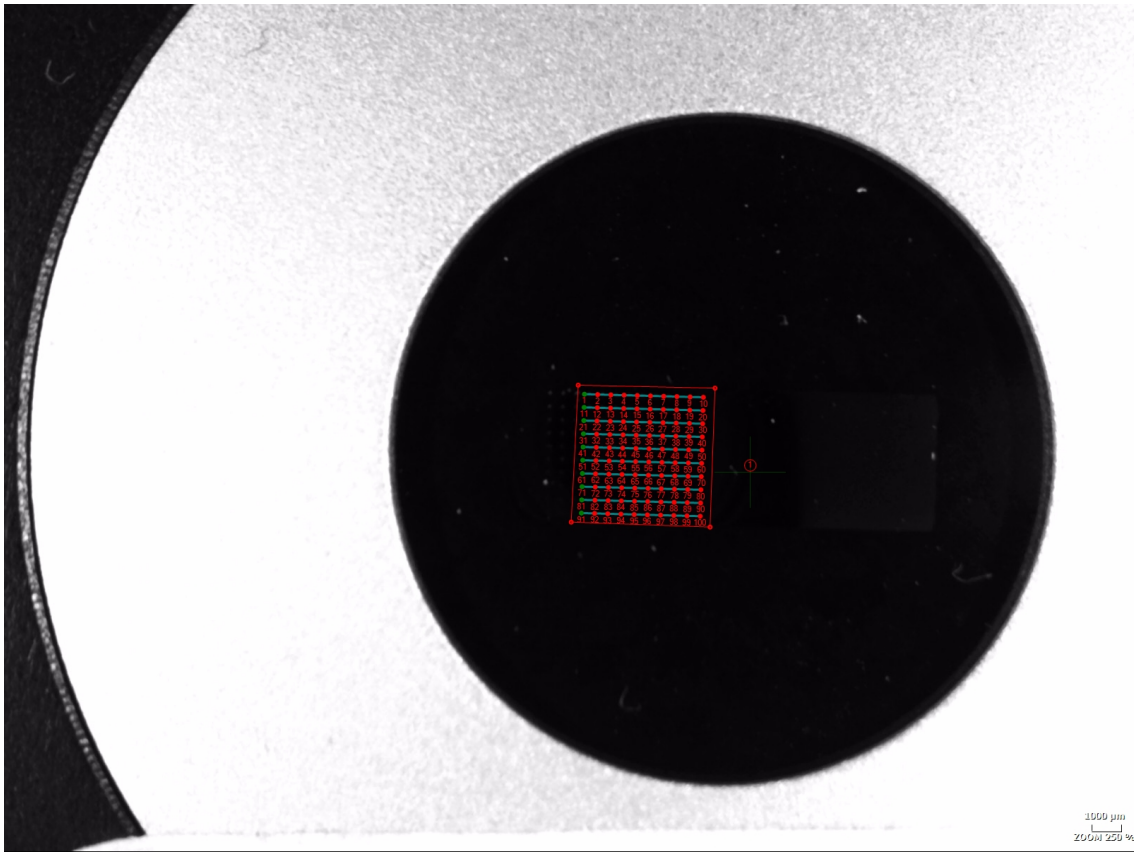

"Enter comments"

Sample: 50D

INNOVATEST®
Advanced Hardness Testing Solutions

Universitetet i Stavanger

www.uis.no

General Information

Date	April 13, 2023
Operator	Johan
Hardness tester type	FALCON 5001

Program Description

Name	IV

Enter Comments

Sample: 50D

Hardness Test Information

Method	VICKERS
Hardness scale	HV5
Dwell time	10 sec.

Color Map

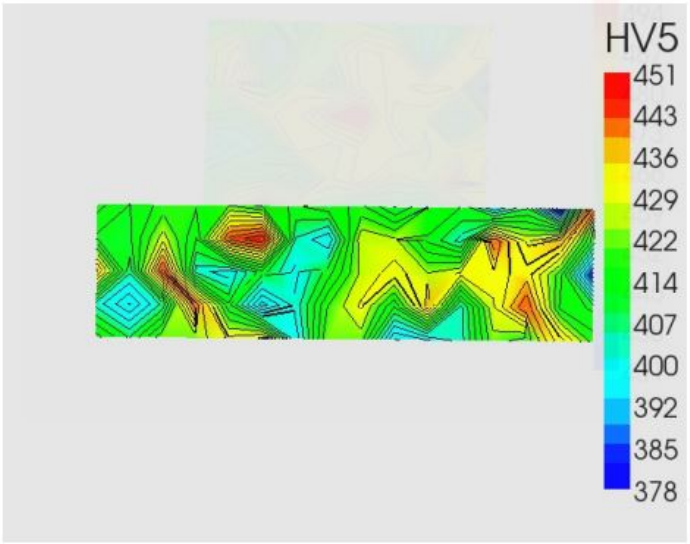

Measurement Tables

Pattern: 1

Measurement Index	Result
1 (1/1)	418 HV5
2 (1/1)	412 HV5
3 (1/1)	418 HV5
4 (1/1)	416 HV5
5 (1/1)	420 HV5
6 (1/1)	415 HV5
7 (1/1)	412 HV5
8 (1/1)	415 HV5
9 (1/1)	417 HV5
10 (1/1)	408 HV5
11 (1/1)	416 HV5
12 (1/1)	412 HV5
13 (1/1)	397 HV5
14 (1/1)	408 HV5
15 (1/1)	378 HV5
16 (1/1)	445 HV5
17 (1/1)	412 HV5
18 (1/1)	412 HV5
19 (1/1)	425 HV5
20 (1/1)	412 HV5
21 (1/1)	444 HV5
22 (1/1)	451 HV5
23 (1/1)	404 HV5
24 (1/1)	397 HV5
25 (1/1)	427 HV5
26 (1/1)	425 HV5
27 (1/1)	412 HV5
28 (1/1)	403 HV5
29 (1/1)	442 HV5
30 (1/1)	427 HV5
31 (1/1)	438 HV5
32 (1/1)	410 HV5
33 (1/1)	437 HV5
34 (1/1)	406 HV5
35 (1/1)	445 HV5
36 (1/1)	403 HV5

37 (1/1)	398 HV5
38 (1/1)	410 HV5
39 (1/1)	400 HV5
40 (1/1)	410 HV5
41 (1/1)	425 HV5
42 (1/1)	430 HV5
43 (1/1)	424 HV5
44 (1/1)	428 HV5
45 (1/1)	430 HV5
46 (1/1)	434 HV5
47 (1/1)	418 HV5
48 (1/1)	383 HV5
49 (1/1)	403 HV5
50 (1/1)	393 HV5
51 (1/1)	406 HV5
52 (1/1)	442 HV5
53 (1/1)	413 HV5
54 (1/1)	391 HV5
55 (1/1)	402 HV5
56 (1/1)	420 HV5
57 (1/1)	428 HV5
58 (1/1)	412 HV5
59 (1/1)	436 HV5
60 (1/1)	403 HV5
61 (1/1)	427 HV5
62 (1/1)	443 HV5
63 (1/1)	416 HV5
64 (1/1)	412 HV5
65 (1/1)	418 HV5
66 (1/1)	408 HV5
67 (1/1)	423 HV5
68 (1/1)	421 HV5
69 (1/1)	428 HV5
70 (1/1)	432 HV5
71 (1/1)	397 HV5
72 (1/1)	423 HV5
73 (1/1)	422 HV5
74 (1/1)	393 HV5
75 (1/1)	396 HV5
76 (1/1)	402 HV5

77 (1/1)	423 HV5
78 (1/1)	417 HV5
79 (1/1)	434 HV5
80 (1/1)	418 HV5

Statistics

Pattern	Mean	Min	Max	SD	Range	USL	LSL	Cp	Cpk
1	417	378	451	15	73	0.00	0.00	0	-9

Snapshot

Snapshot 1

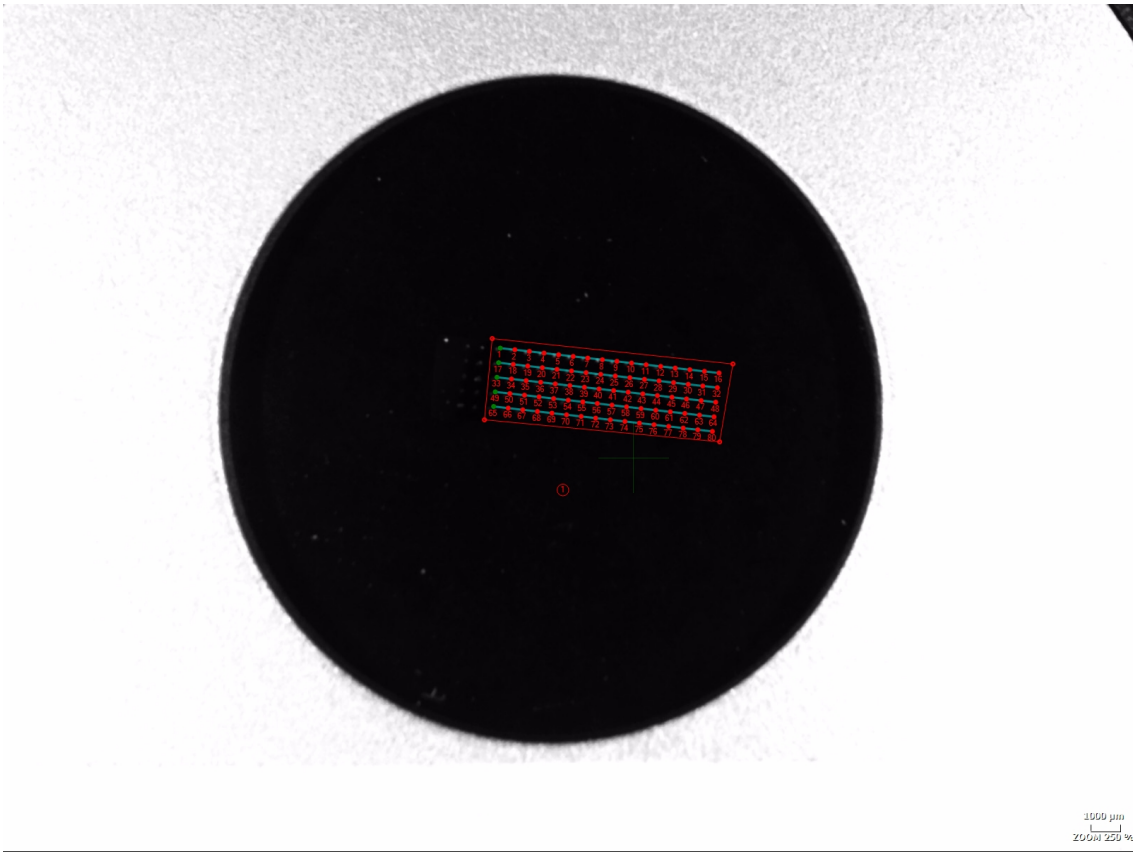

"Enter comments"

Sample: 50DPH

INNOVATEST®
Advanced Hardness Testing Solutions

Universitetet i Stavanger

www.uis.no

General Information

Date	April 13, 2023
Operator	Johan
Hardness tester type	FALCON 5001

Program Description

Name	V

Enter Comments

Sample: 50DPH

Hardness Test Information

Method	VICKERS
Hardness scale	HV5
Dwell time	10 sec.

Color Map

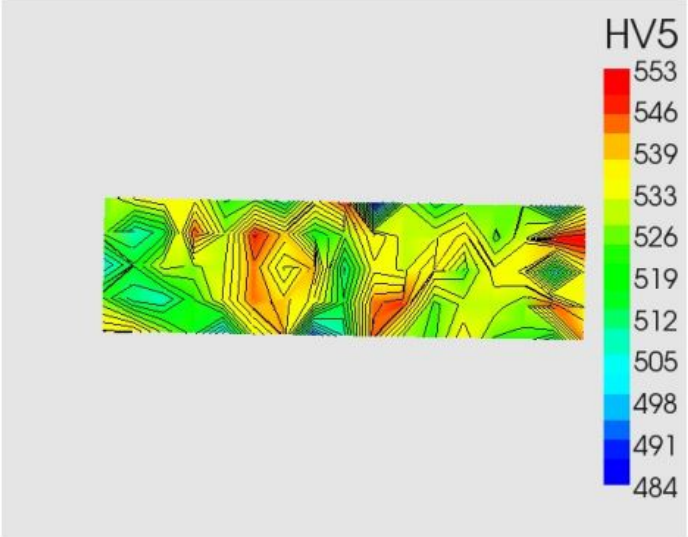

Measurement Tables

Pattern: 1

Measurement Index	Result
1 (1/1)	525 HV5
2 (1/1)	532 HV5
3 (1/1)	535 HV5
4 (1/1)	534 HV5
5 (1/1)	520 HV5
6 (1/1)	524 HV5
7 (1/1)	513 HV5
8 (1/1)	537 HV5
9 (1/1)	549 HV5
10 (1/1)	484 HV5
11 (1/1)	528 HV5
12 (1/1)	519 HV5
13 (1/1)	525 HV5
14 (1/1)	528 HV5
15 (1/1)	524 HV5
16 (1/1)	502 HV5
17 (1/1)	530 HV5
18 (1/1)	526 HV5
19 (1/1)	510 HV5
20 (1/1)	515 HV5
21 (1/1)	548 HV5
22 (1/1)	528 HV5
23 (1/1)	550 HV5
24 (1/1)	541 HV5
25 (1/1)	517 HV5
26 (1/1)	525 HV5
27 (1/1)	539 HV5
28 (1/1)	529 HV5
29 (1/1)	531 HV5
30 (1/1)	537 HV5
31 (1/1)	523 HV5
32 (1/1)	531 HV5
33 (1/1)	552 HV5
34 (1/1)	553 HV5
35 (1/1)	506 HV5
36 (1/1)	517 HV5

37 (1/1)	530 HV5
38 (1/1)	527 HV5
39 (1/1)	531 HV5
40 (1/1)	545 HV5
41 (1/1)	531 HV5
42 (1/1)	544 HV5
43 (1/1)	512 HV5
44 (1/1)	534 HV5
45 (1/1)	531 HV5
46 (1/1)	539 HV5
47 (1/1)	523 HV5
48 (1/1)	533 HV5
49 (1/1)	536 HV5
50 (1/1)	509 HV5
51 (1/1)	535 HV5
52 (1/1)	524 HV5
53 (1/1)	511 HV5
54 (1/1)	510 HV5
55 (1/1)	520 HV5
56 (1/1)	532 HV5
57 (1/1)	546 HV5
58 (1/1)	540 HV5
59 (1/1)	534 HV5
60 (1/1)	517 HV5
61 (1/1)	545 HV5
62 (1/1)	548 HV5
63 (1/1)	523 HV5
64 (1/1)	529 HV5
65 (1/1)	530 HV5
66 (1/1)	525 HV5
67 (1/1)	548 HV5
68 (1/1)	535 HV5
69 (1/1)	539 HV5
70 (1/1)	539 HV5
71 (1/1)	527 HV5
72 (1/1)	519 HV5
73 (1/1)	502 HV5
74 (1/1)	531 HV5
75 (1/1)	543 HV5
76 (1/1)	493 HV5

77 (1/1)	510 HV5
78 (1/1)	547 HV5
79 (1/1)	527 HV5
80 (1/1)	523 HV5
81 (1/1)	534 HV5
82 (1/1)	524 HV5
83 (1/1)	524 HV5
84 (1/1)	514 HV5
85 (1/1)	544 HV5

Statistics

Pattern	Mean	Min	Max	SD	Range	USL	LSL	Cp	Cpk
1	528	484	553	13	69	0.00	0.00	0	-13

Snapshot

Snapshot 1

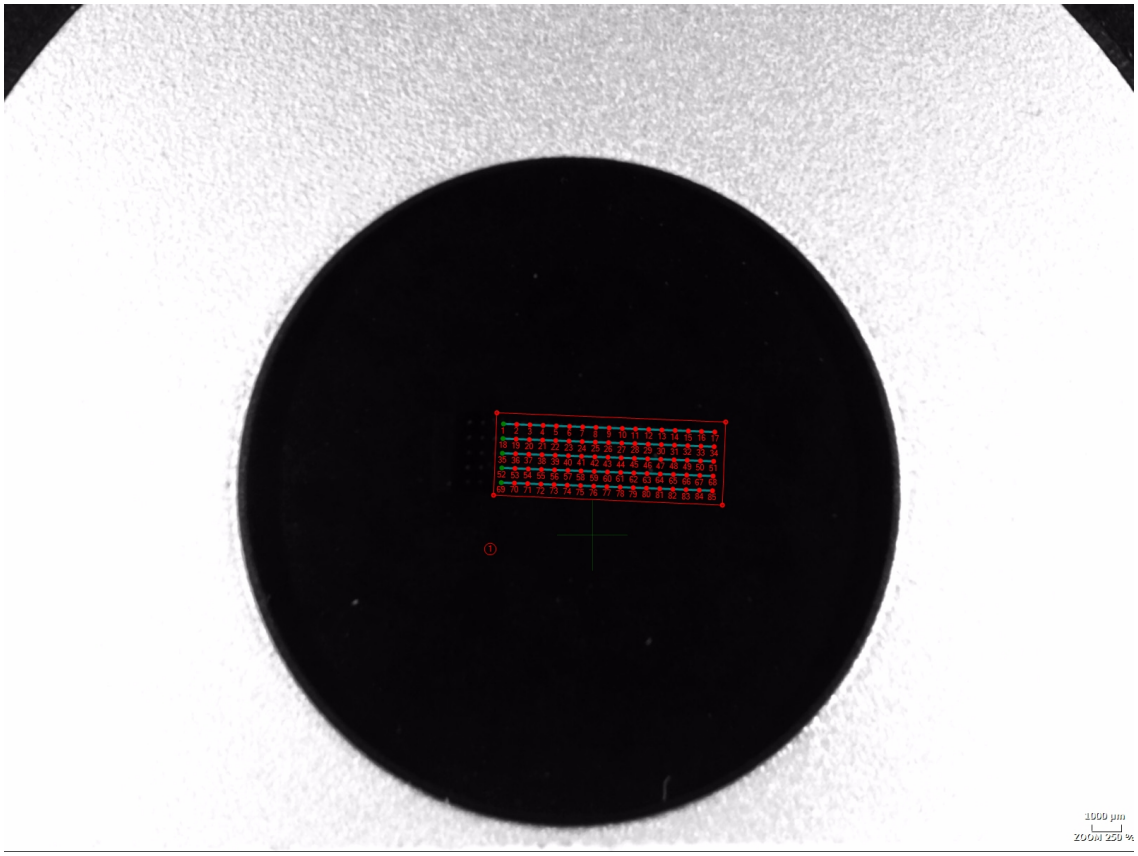

"Enter comments"